CAIO ROBERTO BOTTER

EXPERIMENTAL ANALYSIS OF THE LAMINAR TO TURBULENT TRANSITON PROCESS OF THE BOUNDARY LAYER ON SWEPT WINGS

UNIVERSIDADE FEDERAL DE UBERLÂNDIA
FACULDADE DE ENGENHARIA MECÂNICA
PÓS-GRADUAÇÃO EM ENGENHARIA MECÂNICA
2023

CAIO ROBERTO BOTTER

EXPERIMENTAL ANALYSIS OF THE LAMINAR TO TURBULENT TRANSITON PROCESS OF THE BOUNDARY LAYER ON SWEPT WINGS

Dissertação apresentada ao Programa de Pós-graduação em Engenharia Mecânica da Universidade Federal de Uberlândia, como parte dos requisitos para a obtenção do título de MESTRE EM ENGENHARIA MECÂNICA.

Área de Concentração em Mecânica dos Fluidos e Transferência de Calor

Orientador: Prof. Dr. Francisco José de Souza
Coorientador: Prof. Dr. Odenir de Almeida

UBERLÂNDIA – MG
2023

Ficha Catalográfica Online do Sistema de Bibliotecas da UFU
com dados informados pelo(a) próprio(a) autor(a).

B751
2023

Botter, Caio Roberto, 1995-
EXPERIMENTAL ANALYSIS OF THE LAMINAR TO TURBULENT TRANSITON PROCESS OF THE BOUNDARY LAYER ON SWEPT WINGS [recurso eletrônico] / Caio Roberto Botter. - 2023.

Orientador: Francisco José de Souza.
Coorientador: Odenir de Almeida.
Dissertação (Mestrado) - Universidade Federal de Uberlândia, Pós-graduação em Engenharia Mecânica.
Modo de acesso: Internet.
Disponível em: http://doi.org/10.14393/ufu.di.2023.388
Inclui bibliografia.

1. Engenharia mecânica. I. Souza, Francisco José de , 1973-, (Orient.). II. Almeida, Odenir de,1974-, (Coorient.). III. Universidade Federal de Uberlândia. Pós-graduação em Engenharia Mecânica. IV. Título.

CDU: 621

Bibliotecários responsáveis pela estrutura de acordo com o AACR2:
Gizele Cristine Nunes do Couto - CRB6/2091
Nelson Marcos Ferreira - CRB6/3074

UNIVERSIDADE FEDERAL DE UBERLÂNDIA
Coordenação do Programa de Pós-Graduação em Engenharia Mecânica
Av. João Naves de Ávila, nº 2121, Bloco 1M, Sala 212 - Bairro Santa Mônica, Uberlândia-MG, CEP 38400-902
Telefone: (34) 3239-4282 - www.posmecanicaufu.com.br - secposmec@mecanica.ufu.br

ATA DE DEFESA - PÓS-GRADUAÇÃO

Programa de Pós-Graduação em:	Engenharia Mecânica				
Defesa de:	Dissertação de Mestrado Acadêmico, nº 641, PPGEM				
Data:	09/08/2023	Hora de início:	15:00	Hora de encerramento:	16:50
Matrícula do Discente:	12112EMC001				
Nome do Discente:	Caio Roberto Botter				
Título do Trabalho:	Experimental Analysis of the Laminar to Turbulent Transition Process of the Boundary Layer on Swept Wings				
Área de concentração:	Transferência de Calor e Mecânica dos Fluidos				
Linha de pesquisa:	Transferência de Calor e Mecânica dos Fluidos				
Projeto de Pesquisa de vinculação:	"INVESTIGAÇÃO EXPERIMENTAL DO FENÔMENO DE TRANSIÇÃO LAMINAR-TURBULENTA EM ASA RETA (2D) E ENFLECHADA"				

Reuniu-se por meio de videoconferência a Banca Examinadora, designada pelo Colegiado do Programa de Pós-graduação em Engenharia Mecânica, assim composta: Professores Doutores: Aristeu da Silveira Neto - FEMEC/UFU; Luís Gustavo Trapp - Embraer; Odenir de Almeida (coorientador) - FEMEC/UFU e Francisco José de Souza - FEMEC/UFU, orientador do candidato.

Iniciando os trabalhos o presidente da mesa, Dr. Francisco José de Souza, apresentou a Comissão Examinadora e o candidato, agradeceu a presença do público, e concedeu ao Discente a palavra para a exposição do seu trabalho. A duração da apresentação do Discente e o tempo de arguição e resposta foram conforme as normas do Programa.

A seguir o senhor(a) presidente concedeu a palavra, pela ordem sucessivamente, aos(às) examinadores(as), que passaram a arguir o(a) candidato(a). Ultimada a arguição, que se desenvolveu dentro dos termos regimentais, a Banca, em sessão secreta, atribuiu o resultado final, considerando o(a) candidato(a):

Aprovado.

Esta defesa faz parte dos requisitos necessários à obtenção do título de Mestre.

O competente diploma será expedido após cumprimento dos demais requisitos, conforme as normas do Programa, a legislação pertinente e a regulamentação interna da UFU.

Nada mais havendo a tratar foram encerrados os trabalhos. Foi lavrada a presente ata que após lida e achada conforme foi assinada pela Banca Examinadora.

---

sei! assinatura eletrônica

Documento assinado eletronicamente por **Francisco José de Souza**, **Professor(a) do Magistério Superior**, em 09/08/2023, às 16:55, conforme horário oficial de Brasília, com fundamento no art. 6º, § 1º, do Decreto nº 8.539, de 8 de outubro de 2015.

---

sei! assinatura eletrônica

Documento assinado eletronicamente por **Aristeu da Silveira Neto**, **Professor(a) do Magistério Superior**, em 09/08/2023, às 16:55, conforme horário oficial de Brasília, com fundamento no art. 6º, § 1º, do Decreto nº 8.539, de 8 de outubro de 2015.

Documento assinado eletronicamente por **Luis Gustavo Trapp**, **Usuário Externo**, em 09/08/2023, às 17:24, conforme horário oficial de Brasília, com fundamento no art. 6º, § 1º, do Decreto nº 8.539, de 8 de outubro de 2015.

Documento assinado eletronicamente por **Odenir de Almeida**, **Professor(a) do Magistério Superior**, em 10/08/2023, às 11:17, conforme horário oficial de Brasília, com fundamento no art. 6º, § 1º, do Decreto nº 8.539, de 8 de outubro de 2015.

A autenticidade deste documento pode ser conferida no site https://www.sei.ufu.br/sei/controlador_externo.php?acao=documento_conferir&id_orgao_acesso_externo=0, informando o código verificador **4662911** e o código CRC **5E2A903F**.

Referência: Processo nº 23117.051301/2023-94 SEI nº 4662911

Agradecimentos

A conclusão de uma dissertação de mestrado mostra o término de mais um ciclo. São dois anos dentro de um período da vida, que se inicia logo após a graduação no qual tudo muda de uma hora para a outra e muito repentinamente. Em cada ciclo conhecemos pessoas novas enquanto outras se despedem para seguirem outros caminhos nessa vida ou na próxima. Às vezes somos nós mesmos que nos despedimos. Mas é sempre necessário agradecer àqueles que estiveram do nosso lado. Muitas vezes são eles que nos movem e nos dão forças. Muitas vezes nos ajudam a realizar nossos sonhos e a seguir com nossos caminhos. Dessa forma, início agradecendo a meus pais e a meu irmão por todo o apoio incondicional e totalmente sem medida. São vocês que me dão forças quando não as encontro. Em seguida, assim como em meu trabalho de conclusão de curso, deixo meus agradecimentos ao professor Odenir por estar comigo desde o início da minha graduação guiando meus trabalhos e me dando conselhos para seguir meu caminho. Estendo ao professor Francisco por ter aceitado ser meu orientador neste trabalho, ao professor Catalano não só por seu auxílio nas discussões e tomadas de decisão dessa dissertação, mas também por ter me permitido utilizar as instalações de seu laboratório para efetuar os experimentos. Agradeço ao agora professor doutor João Paulo por cada momento que gastou comigo nas discussões, elaboração de códigos e explicações. Aos quatro professores, além de todo o apoio prestado, agradeço como aluno por todo o amor e dedicação que vocês para com a arte de ensinar e de fomentar a pesquisa brasileira, algo que infelizmente não é compartilhado por todos. Agradeço também aos técnicos Osnam e Reinaldo pelo trabalho incrível realizado na nossa asa e em sua adaptação ao túnel de vento LAE-1 da USP. Agradeço também à FAPEMIG pelo financiamento deste trabalho sob o projeto APQ-01589-21. Por fim, agradeço a minha família e aos meus amigos que fiz na infância, na faculdade e após ela.

BOTTER, C. R. **Experimental Analyses of the Laminar to Turbulent Transition Process of the Boundary Layer on Swept Wings.** 2023. 150 f. Master’s Degree Dissertation, Universidade Federal de Uberlândia, Uberlândia.

Resumo

O uso de termografia infravermelha para detecção da fronte de transição de um modelo de asa com 25 º de ângulo de enflechamento e seção transversal dada por um aerofólio simétrico foi estudado em um túnel de vento soprador de circuito fechado. O modelo foi manufaturado em fibra de vidro, pintado em tinta preta fosca, e foi submetido ao calor de lâmpadas halogênicas para aumentar a emissividade térmica, e assim o contraste entre a asa e o meio, permitindo uma melhor visualização dos estágios turbulento e laminar da camada limite. Em seguida, um código de processamento de imagens em Python foi utilizado para detectar a fronte de transição e indicar sua posição. Várias combinações de números de Reynolds e ângulos de ataque foram testados, variando entre $4{,}50 \cdot 10^5 \leq Re \leq 9{,}15 \cdot 10^5$ e $0\,° \leq \alpha \leq 14\,°$ visando uma melhor avaliação do comportamento da fronte de transição em vários cenários. Isso permitiu a análise do fenômeno da transição contrastando os resultados com a literatura, permitindo assim se inferir sobre os mecanismos que estão agindo no sistema. Apesar de algumas exceções, a maioria dos pontos testados seguiram as expectativas, com maiores números de Reynolds e ângulos de ataque mais altos resultando em uma transição mais avançada. Em seguida, as imagens infravermelhas foram contrastadas com as de um trabalho anterior que ensaiou a detecção da posição da transição em um modelo de asa reta de mesma corda e aerofólio da presente asa enflechada. Esta última comparação teve por objetivo avaliar a significância das instabilidades de vento cruzado no desenvolvimento da camada limite, e assim como elas modificam a posição da fronte de transição. Um fenômeno interessante foi então observado onde para pequenos ângulos de ataque a asa enflechada apresentou uma transição mais próxima ao bordo de ataque enquanto que para ângulos de ataque mais altos a camada limite da asa reta foi a primeira a transicionar, provavelmente implicando que ela está transicionando por outro fenômeno que as ondas T-S. além das aquisição das imagens infravermelhas, para melhor qualificar o escoamento sobre a asa enflechada, a distribuição de pressão e os esforços aerodinâmicos de sustentação e arrasto foram obtidos respetivamente por um transdutor de pressão e uma balança aerodinâmica.

Palavras-Chave: Fronte de Transição de Camada Limite – Asa Enflechada – Instabilidade de Vento Cruzado – Termografia Infravermelha.

BOTTER, C. R. **Experimental Analysis of the Laminar to Turbulent Transition Process of the Boundary Layer on Swept Wings.** 2023. 150 f. Master's Degree Dissertation, Universidade Federal de Uberlândia, Uberlândia.

Abstract

The utilization of infrared thermography for the detection of the boundary layer transition front with a 25º swept wing model of a laminar airfoil cross-section has been studied and tested in a blow-down and closed-circuit wind tunnel. The model, manufactured in fiberglass, has been painted in black matte paint and was submitted to the heat of halogenic lights to increase its thermal emissivity and thus increase the thermal contrast of the body to the mean allowing a better visualization of the turbulent and the laminar stages of the boundary layer. Later, a Python image processing code was used to detect the transition front and result in its position. Combinations of Reynolds numbers and angles of attack have been tested, varying from $4{,}50 \cdot 10^5 \leq Re \leq 9{,}15 \cdot 10^5$ and $0\,° \leq \alpha \leq 14\,°$, to better verify the behavior of the transition front position to various scenarios. This permitted the analyses of the transition phenomena contrasting the results with the literature allowing the inference of the mechanisms that are acting on the system. Besides some special cases, most of the tested points followed the expectations, with higher Reynolds numbers and higher angles of attack providing an early transition position. After, the infrared images have been contrasted with the infrared images of a straight wing model of same chord and airfoil as the present swept wing. The later comparison was to evaluate the significance level of the crossflow instabilities in the development of the boundary layer, and thus how it would modify the transition front position. An interesting phenomenon was then observed were for small angles of attack the swept wing showed a closer to the leading-edge transition front position as expected, while for higher alphas the boundary layer of the straight wing was firstly transitioning, implying that it is in truth transitioning by other mechanisms then the T-S waves. Besides the infrared images acquisition, to better qualify the flow over the swept wing, the pressure distribution over the wing and the aerodynamics efforts of lift and drag have also been characterized respectively by a pressure transducer and an aerodynamics balance.

Keywords: Boundary Layer Transition Front – Swept Wing – Crossflow Instability – Infrared Thermography

List of Figures

Figure 1.1: Concept of aircraft drag forces and drag reduction potential analyses. (ABBAS et al., 2017). 2
Figure 1.2: Common events of the airflow over a wing cross section. Adapted from Gudmundsson (2014) 3
Figure 2.1: Boundary layer development on a flat plate (SCHLICHTING & GERSTEN, 2017). 11
Figure 2.2: Sketch of continuous mode transition in a boundary layer on a flat plate at zero incidence (SCHLICHTING & GERSTEN, 2017). 13
Figure 2.3: Airbus A-380. Source: https://www.aerospace- technology.com/features/feature top-ten-aircraft-with-the-longest-wings-4448115/ 16
Figure 2.4: Effect of a swept wing on critical Mach number. Adapted from (ANDERSON, 2018 (b)). 16
Figure 2.5: Schematic comparison between both T-S waves and CFI path over the wing. Adapted from SERPIERI, 2018. 19
Figure 2.6: 3D Boundary Layer on a Swept Wing and Transition Mechanisms (BECK et al., 2018). 20
Figure 2.7: Görtler instabilities scheme. Seeding of Görtler Vortices Through a Suction and Blowing Strip (SOUZA et al., 2004). 21
Figure 4.1: Laminar Airfoil Modified From NACA3609 32
Figure 4.2: Straight Wing configuration for the pressure taps assemble. 33
Figure 4.3: Swept wing model. 35
Figure 4.4: Gap between the swept wing model and the wind tunnel superior wall. 35
Figure 4.5: Swept wing model basis. 36
Figure 4.6: Swept wing model basis with fixation discs attached. 36
Figure 4.7: Fixation screws used for the wing model attachment to the endplate. 37
Figure 4.8: Manufactured Swept Wing Model. 37
Figure 4.9: Endplate CAD Model. 38
Figure 4.10: Endplate to swept wing model assemble. 39
Figure 4.11: Project variables and axis system. 40
Figure 4.12: LAE-1 Wind Tunnel Schematics 42
Figure 4.13: Allogeneic lights and corner vanes installation into the wind tunnel test section. 44
Figure 4.14: Calibration points for the infrared camera. 45
Figure 4.15: Experimental assemble with infrared camera positioning. 45
Figure 4.16: Scanivalve ZOC33/64 Px X1. 47
Figure 4.17: Three Components Aerodynamics Balance. 48
Figure 5.1: Swept Wing Pressure Field for Re = 450000 and $0^\circ \leq \alpha \leq 5^\circ$ 54
Figure 5.2: Swept Wing Pressure Field for Re = 650000 $0^\circ \leq \alpha \leq 5^\circ$ 55
Figure 5.3: Swept Wing Pressure Field for Re = 720000 $0^\circ \leq \alpha \leq 5^\circ$ 56
Figure 5.4: Swept Wing Pressure Field for Re = 765000 $0^\circ \leq \alpha \leq 5^\circ$ 57
Figure 5.5: Swept Wing Pressure Field for Re = 915000 $0^\circ \leq \alpha \leq 5^\circ$ 58
Figure 5.6: Endplate Lift x Dynamic Pressure 59
Figure 5.7: Endplate Drag x Dynamic Pressure 60
Figure 5.8: Swept Wing $CL\ x\ \alpha$ *for each Reynolds Number* 61
Figure 5.9: Swept Wing Drag Polar for each Reynolds Number 62

Figure 5.10: Image comparison for raw and tread images for the swept wing boundary layer transition detection at 4 ° of angle of attack and Re = 450000. Left: Raw image. Raw: Treat image. 63
Figure 5.11: Infrared Results for Transition Line Detection at Re = 450000. 64
Figure 5.12: Infrared Results for Transition Line Detection at Re = 650000. 65
Figure 5.13: Infrared Results for Transition Line Detection at Re = 720000. 66
Figure 5.14: Infrared Results for Transition Line Detection at Re = 765000. 67
Figure 5.15: Infrared Results for Transition Line Detection at Re = 915000. 67
Figure 5.16: Swept Wing Transition to Turbulence Position in Function of the Angle of Attack 68
Figure 5.17: Swept x Straight wing comparison for Re = 450000 and $0^\circ \leq \alpha \leq 3^\circ$ 73
Figure 5.18: Swept x Straight wing comparison for Re = 450000 $4^\circ \leq \alpha \leq 7^\circ$ 74
Figure 5.19: Swept x Straight wing comparison for Re = 650000 $2^\circ \leq \alpha \leq 5^\circ$ 75
Figure 5.20: Swept x Straight wing comparison for Re = 765000 $2^\circ \leq \alpha \leq 5^\circ$ 76
Figure 5.21: Swept x Straight wing comparison for Re = 915000 $0^\circ \leq \alpha \leq 2^\circ$ 77
Figure 5.22: Swept x Straight wing comparison for Re = 915000 $3^\circ \leq \alpha \leq 5^\circ$ 78
Figure 5.23: Swept x Straight Wing Transition to Turbulence Position in Function of the Angle of Attack 79
Figure 5.24: Pressure Distribution simulated at XFLR5 for the Straight Wing 82
Figure I.0.1: Kelvin-Helmholtz instabilities occurring in nature. (KOWNACKI, 2019) 92
Figure II.0.2: Kelvin-Helmholtz instability evolution. (CUSHMAN-ROISIN and BECKERS 2006). 92
Figure III.0.3: Scheme of the Rayleigh-Bérnard cells fomrmation. (RANJAN, 2019) 94
Figure IV.4: Visualization of Taylor–Couette and spiral Poiseuille flows using a snapshot FLASH spatial tagging sequence. (MOSER et al., 2000). 95
Figure VIII 0.1: Swept Wing Infrared Thermography for Re = 450000 122
Figure VIII.0.2: Swept Wing Infrared Thermography for Re = 650000 123
Figure VIII.0.3: Swept Wing Infrared Thermography for Re =720000 124
Figure VIII.0.4: Swept Wing Infrared Thermography for Re =765000 125
Figure VIII.0.5: Swept Wing Infrared Thermography for Re =915000 125

List of Tables

Table 4.1: Infrared Camera Characteristics......46
Table 4.2: Pressure Field Determination Test Matrix......49
Table 4.3: Aerodynamics Efforts Acquisition Test Matrix......51
Table 4.4: Infrared Visualization Test Matrix......52
Table 5.1: Medium Value for the Transition Front to Turbulence Position......68
Table 5.2: Matrix for Swept x Straight Models Comparison......72
Table 5.3: Transition Front to Turbulence Position for the Swept x Straight Models......79
Table 5.4: Wind Tunnel x XFLR5 Transition Front Position Resutls......81
Table IV.1: Pressure Distribution for $\alpha = 0\,°$......106
Table IV.2: Pressure Distribution for $\alpha = 1\,°$......107
Table IV.3: Pressure Distribution for $\alpha = 2\,°$......109
Table IV.4: Pressure Distribution for $\alpha = 3\,°$......110
Table IV.5: Pressure Distribution for $\alpha = 4\,°$......112
Table IV.6: Pressure Distribution for $\alpha = 5\,°$......113
Table V.1: Swept Wing Results for Aerodynamics Balance at Re = 450000......115
Table V.2: Swept Wing Aerodynamics Balance After Wind Tunnel Correction for Re = 450000......115
Table V.3: Swept Wing Results for Aerodynamics Balance at Re = 650000......116
Table V.4: Swept Wing Aerodynamics Balance After Wind Tunnel Correction for Re = 650000......116
Table V.5: Swept Wing Results for Aerodynamics Balance at Re = 720000......117
Table V.6: Swept Wing Aerodynamics Balance After Wind Tunnel Correction for Re = 720000......117
Table V.7: Swept Wing Results for Aerodynamics Balance at Re = 765000......117
Table V.8: Swept Wing Aerodynamics Balance After Wind Tunnel Correction for Re = 765000......118
Table V.9: Swept Wing Results for Aerodynamics Balance at Re = 915000......118
Table V.10: Swept Wing Aerodynamics Balance After Wind Tunnel Correction for Re = 915000......118
Table VI.1: Laminar Airfoil 3609 Coordinates......119
Table VII.1: Pressure Taps Coordinates......121

List of Symbols

α – angle of attack

BL – Boundary Layer

Cd – Drag Coefficient

CF – Crossflow

CFI – Crossflow Instabilities

CFV – Crossflow Vortices

CL – Lift Coefficient

CP – Pressure Coefficient

IR – Infrared

Re – Reynolds Number

T-S – Tollmien-Schlichting

Summary

1. INTRODUCTION 1
  1.1 From Wind Tunnel to the Boundary Layer Transition on Swept Wings 1
  1.2 Motivation for Studying the Transition Process on Swept Wings 5
2. PHENOMENOLOGY 8
  2.1 The Linear Stability Theory 8
  2.2 The Transition to Turbulence of the Boundary Layer 11
  2.3 The Straight Wing 14
  2.4 The Swept Wing 15
    2.4.1. Tollmien and Schlichting Instability 17
    2.4.2. Cross Flow Instability 18
    2.4.3. Görtler Instability 20
    2.3.4 Attachment Line Instability 21
3. BIBLIOGRAPHIC REVIEW 22
4. METHODOLOGY 31
  4.1 Swept Wing Model Construction Background 31
  4.2 Swept Wing Model and Manufacture 33
  4.3 Project Variables 39
  4.4 Materials and Methods 41
    4.4.1 Wind Tunnel Facility 42
    4.4.2 Infrared Thermography Camera 42
    4.4.3 Pressure Transducer 46
    4.4.4 Aerodynamics Balance and Aerodynamics Efforts Determination 47
  4.5 Experiments Description 48
    4.5.1 Pressure Field Determination 48
    4.5.2 Lift and Drag Acquisition 49
    4.5.3 Transition Front Detection Via Infrared Thermography 51
5. RESULTS AND DISCUSSIONS 53
  5.1 Pressure Field Results 53
    5.1.1 Pressure Field Distribution – Re = 450000. 54
    5.1.2 Pressure Field Distribution – Re = 650000 55
    5.1.3 Pressure Field Distribution – Re = 720000 56
    5.1.4 Pressure Field Distribution – Re = 765000 57

5.1.5 Pressure Field Distribution – Re = 915000 58
5.2 Lift and Drag Measurements 59
5.2.1 End Plate Lift and Drag 59
5.2.2 $CL\ x\ \alpha$ Results 61
5.2.3 Drag Polar Results 62
5.3 Boundary Layer Transition Front Detection 63
5.3.1 Swept Wing Infrared Images - Re = 450000 64
5.3.2 Swept Wing Infrared Images - Re = 650000 65
5.3.3 Swept Wing Infrared Images - Re = 720000 66
5.3.4 Swept Wing Infrared Images - Re = 765000 67
5.3.5 Swept Wing Infrared Images - Re = 915000 67
5.3.6 Transition Front position in terms of wing cord in function of the angle of attack. 68
5.4 Swept Wing Experiments Results Discussion 69
5.5 Swept x Straight Wing IR Image Comparison 72
5.5.1 $Reswept = 450000 \quad x \quad Restraight = \ 486000$ 73
5.5.2 $Reswept = 650000 \quad x \quad Restraight = \ 655000$ 75
5.5.3 $Reswept = 765000 \quad x \quad Restraight = \ 787000$ 76
5.5.4 $Reswept = 915000 \quad x \quad Restraight = 950000$ 77
5.5.5 Transition Front position in terms of wing cord in function of the angle of attack. 79
5.6 Swept x Straight Wing Infrared Results Discussion 80
6. CONCLUSION 84
6.1 Future Works Perspective 85
REFERENCES 87
APPENDIX I 91
APPENDIX II 96
APPENDIX III 104
APPENDIX IV 106
APPENDIX V 115
APPENDIX VI 119
APPENDIX VII 121
APPENDIX VIII 122
ANNEX I 126
ANNEX II 127

ANNEX III... 135

CHAPTER I

1. INTRODUCTION

1.1 From Wind Tunnel to the Boundary Layer Transition on Swept Wings

Many techniques, instruments and devices have been developed and implemented by technological and research centers to predict and study the aerodynamics characteristics of the airflow to body interaction, such as obtaining the aerodynamics efforts of lift, drag and pitching moment via aerodynamics balance, velocity fields determination via hotwire anemometry or particle image velocimetry, pressure field determination via a huge sort of pressure transducers, flow visualization via smoke, tufts, China-clay, flow-visualization painting, and nowadays the state of the art, via infrared thermography (HOESSLIN et al., 2017). The technique to be applied at each study will mostly depend on the object of interest, the know-how of the institution and the resources available. The latter technique, however, is being vastly applied and becoming almost a demand for the state of the art on aerodynamics research of wings: the study of the transition process of the boundary layer from the laminar to the turbulent state. Other visualization methods may be able to detect the transition, but infrared thermography can detect it with high fidelity, and it is considered a non-intrusive method (Crawford et al., 2013).

One of the main reasons for studying the boundary layer transition process is the drag force, since its intensity is higher on the turbulent boundary layer than in the laminar. Knowing the coordinates from where the transition happens allow the utilization of flow control devices to retard or maybe even prevent the transition to turbulence to happen. In other words, the application of these methods shall reduce drag, which for the aeronautical world will then be converted into fuel saving (DAGENHART and SARIC, 1999). Aircraft manufacturers already use some flow control techniques based on non-active control (suction flow areas, roughness superficial design and other aerodynamic devices…). However, active control should provide better results as it can be more easily adapted for each flight stage and acts directly in the source of the problem. Nevertheless, even if the method to be applied is active based or not, the transition front must be well known.

The drag force has many causes, in which the most protuberant ones are the lift induced drag and the viscous drag. As its own name implies, the lift induced drag happens due to the simple existence of the lift force that causes the drag. Wing shape optimization, wing devices and load control can be applied to decrease this factor. Concerning the viscous drag, its main cause is due to the viscous interaction between the flow and the surface of the wing. Figure 1.1 represents the composition of the drag force that acts on a wing.

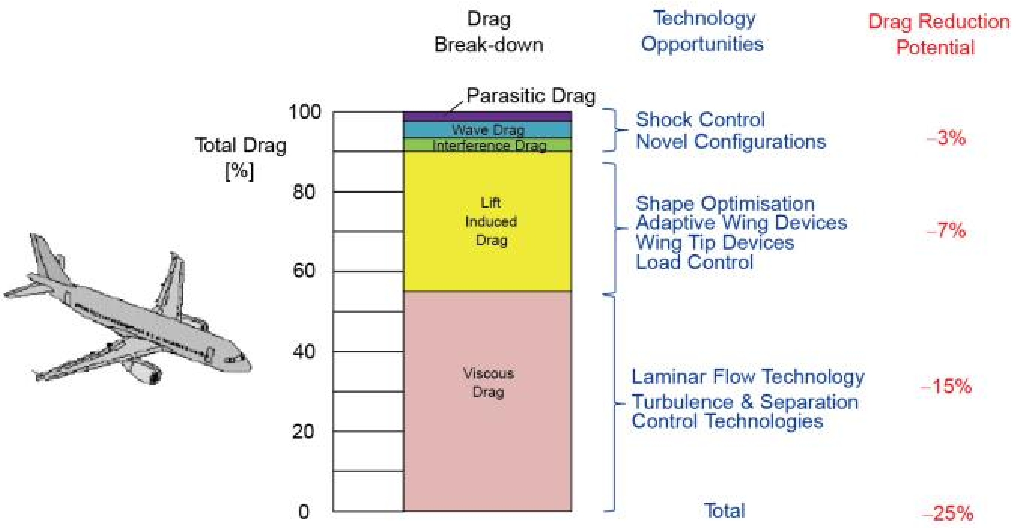

Figure 1.1: Concept of aircraft drag forces and drag reduction potential analyses. (ABBAS et al., 2017).

This viscous interaction causes the appearance of the boundary layer. As the airflow progresses along the wing chord, the layer becomes thicker and the flow velocity inside it will lose energy due to frictional effects between the flow molecules and the wing surface. Consequently, at a specific point, the boundary layer detachment may occur and from that point on the generation of lift ceases. The boundary layer detachment occurs due to the loss of energy of the air molecules that can no longer support the boundary layer pressure gradient that act against the molecule's adhesion to the wall. The thickening of the boundary layer may also happen due the amplification of disturbances within it, originating from the viscous interaction of the air molecules and the body surface. However, under certain conditions, rather than losing energy, the flow will energize itself through viscous interactions, and keep it attached to the body surface, conducting itself to the turbulent state. In contrast to its laminar counterpart, since the turbulent boundary layer has more kinetic energy, the frictional tension is higher, resulting in a more pronounced viscous drag. Although the turbulent layer induces more drag, the air molecules exhibit greater kinetic energy, potentially preventing the detachment (ANDERSON, 1987). Thus, at times inducing the transition may be advantageous to maintain the flow's attachment to the body. Figure 1.2 illustrates the possible stages of the airflow over a wing cross-section.

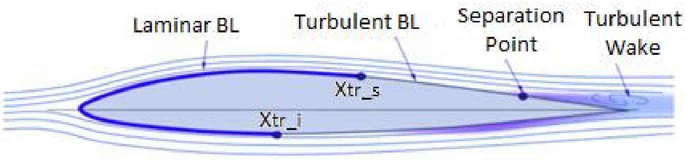

Figure 1.2: Common events of the airflow over a wing cross section. Adapted from Gudmundsson (2014)

In simple terms, for the transition to turbulence to occur, a series of instabilities of a large range of wavelengths must be introduced into the laminar flow certain conditions are met, these instabilities can amplify into larger, more intricate structures, carrying greater energy through a non-linear process, ultimately leading to the turbulent state. The more advanced the wing design, the more complex the flow-body interaction becomes, resulting in a multitude of phenomena simultaneously occurring within the boundary layer. Consequently, for the flow control techniques to be as effective as possible, they should aim to prevent the amplification of instabilities, preventing the formation of more complex structures.

Thereby, initiative in the aeronautical industry involves the adoption of laminar wings, designed to minimize transition occurrence along most of the wing chord. However, this achievement for commercial aircraft necessitates flying at transonic speeds presenting a challenge in developing such wings due to the increased likelihood of transition associated with higher Reynolds numbers. Employing flow control devices, whether active or passive, and optimizing the wing's geometry and airfoil can help to mitigate flow instability and reduce the probability of transition.

To advocate for the utilization of flow control devices, especially in the active category, a comprehensive understanding of airflow over the wing is crucial, so that this understanding enables a precise application of control techniques at strategic locations to achieve optimal results. Some of the transition characteristics that must be acknowledged, such as the transition point to turbulence and the process's initial point. The application of Linear Stability Theory, coupled with semi-empirical methods, is essential for this purpose These methods necessitate experimentation, whether through actual flight tests, wind tunnels with scaled models, or numerical-computational models. However, numerical-computational models still face challenges due to the complexity of interactions between turbulent structures, especially during the development of the boundary layer. If turbulence is computationally simulated via DNS, even simple flow to structure interactions demands a lot of simulation time since every structure interaction is simulated. If LES or RSM methods are used, the need of closing models appear and they need to be very well calibrated for each case (SILVEIRA NETO, 2020), being very specific for each case, and thus not always presenting the most trustworthy results without a good historic of results and material experimentation to be compared to. Therefore, wind tunnel and flight test must be applied for the transition study.

Nevertheless, even with wind tunnel testing offering a more controlled environment than real flight tests, caution is imperative. Turbulence is highly sensitive to even minor perturbations owing to its inherently chaotic nature. Factors such as noise, mechanical or acoustic vibrations, and surface impurities on the model can lead to significantly disparate results. Specifically, if the transition from laminar to turbulence on wings is the subject of study, the airflow in the inlet of the test section must be as laminar as possible, with very little variations on the medium velocity profile. Otherwise, deviations in the medium velocity profile can cause the airflow to reach the leading edge of the model in a turbulent state. Additionally, minimizing the intrusiveness of experimental equipment is essential to reduce its influence on the airflow. Therefore, regardless of the chosen study method, meticulous care must be exercised to ensure the reliability of the results.

An example of ongoing research in this field there is the Airbus "Breakthrough Laminar Aircraft Demonstrator in Europe (BLADE)" project, which focuses on studying wing surface imperfections and tolerances to maintain laminar flow. The project involves extensive measurement points for wing surface waviness, infrared cameras to monitor the wing temperature, an acoustic generator to assess acoustic influence in the transition process, and a reflectometry system to measure wing deformation during flight. On 26 September of 2017 the prototype made its first flight, standing in air for 3 h 48’. The project aims to reduce viscous drag by 50% compared to previous wing models, translating to approximately 5% less carbon dioxide emission (FENDT, M.; DUVELLEROY, 2017).

In the pursuit of knowledge and understanding complex or simple problems, commencing with the simplest case in a controlled environment is often advisable. For investigating the transition point from laminar to turbulent states in the boundary layer, the simplest and controlled scenario involves a straight laminar wing tested in a wind tunnel facility, without applying additional wing configurations or aerodynamic devices. Then, thinking about the evolution in terms of simplicity, the next step should be the application of a sweep angle on this straight wing while maintaining the other characteristics.

Thereby, this work presents a discussion of theory, methods and results from a wind tunnel testing campaign that intends to analyze the transition front to turbulence in the boundary layer of a swept wing. The straight case has already been experimented in Eguea (2022). Following the presentation of experimental methods and results, the swept wing case is compared to the straight wing, aiming to comprehend the influence of the sweep angle on the transition process to turbulence in the wing's boundary layer. Thus, a swept wing model of 1.2 m of wingspan and 0.5 m of chord has been manufactured on fiberglass and tested in a wind tunnel facility at low Reynolds numbers. The experiments involved an aerodynamics balance for force characterization, a pressure transducer for pressure coefficient distribution, and an infrared camera to register the transition front to turbulence.

1.2 Motivation for Studying the Transition Process on Swept Wings

In the aeronautical world, performance is a metric that showcases the capabilities of an aircraft in executing various maneuvers. While safety is paramount and enables the aircraft's approval for production and sale, it's the demonstrated performance that truly captivates possible buyers. Thereby, its goal is to compute the takeoff field length, the time to climb to the cruise altitude, the cruise velocity, and more. Among these, fuel consumption during flight stands out as a vital economic parameter for assessing aircraft profitability. Given that the drag force is an aerodynamic force that opposes the forward motion of the aircraft, researchers have always investigated mechanisms and devices to reduce the total drag acting on the aircraft, and currently, frictional drag is a focal point given its potential for significant reductions and subsequent savings (VIUNESSA and SCHLATTER 2017). As previously pointed out, the transition to turbulence on the boundary layer of wings is a highlight on the viscous drag reduction, as maintaining a laminar attached flow for a longer chordwise length is translated into reduced drag.

Moreover, the transition mechanism to turbulence becomes increasingly intricate as one progresses from the simple straight wing to the modern wings seen in contemporary commercial aircraft. Regardless of the specific wing shape, the presence of high lift devices, and the application of construction angles, this transition cannot be considered a simple process. Though, the aerodynamics mechanisms and their interactions within the boundary layer become more complex as the wing's design becomes more elaborated. To illustrate, in a conventional straight wing, the boundary layer typically transitions due to the evolution of Tollmien-Schlichting (T-S) waves, while for the swept wing, as the wing complexity increases, besides the T-S waves, the crossflow instabilities emerge, potentially playing a significant role in the transition process. For this case, factors such as the wing cross section, the Reynolds Number, the sweep angle, the surface roughness and the angle of attack, the transition to turbulence will be more influenced by one kind of instabilities or the other, reflecting on the transition front position.

For instance, while it's logical to anticipate that an increase in the angle of attack might bring the transition front closer to the leading edge, precise computation of how much the transition front shifts with variations in the angle of attack remains challenging, even with today's advanced numerical-computational models. This analysis can be thought of for other parameters as well. Thus, issue with relying solely on numerical-computational methods is that they are not yet fully equipped to accurately compute all the interactions that can occur during the transition process that have the potential to alter the expected outcomes, which may lead to incorrect results, or they require an extensive amount of time to model all the interactions.

In contrast, material experimentation conducted in a wind tunnel becomes, then, of immense value since it allows for the isolation of numerous effects that are present in the natural environment, like the excessiveness of noise, the production a laminar flow, the isolation of external disturbances, and, with proper precautions, it can reproduce the transition phenomena in a more reliable way since it does not depend on a mathematical equation to model it. Therefore, it becomes evident that a comprehensive understanding and advancement in aerodynamics research necessitate a synergistic approach involving both numerical-computational simulations and meticulous material experimentation in controlled environments like wind tunnels.

Hence, the motivation for the present study is to delve into the transition mechanisms of swept wings and how they impact the position of the transition front within the boundary layer. Thus, this research builds upon the earlier exploration of the boundary layer transition process to turbulence in the straight wing case (EGUEA, 2022), adding the sweep angle to the former straight wing configuration, increasing its complexity. Then, locating the transition front on both straight and swept models, for the Reynolds and angle of attack measured range, will allow future studies to focus on proposals for active flow control devices, and characterize them for each situation if it is better to act on each type of instability for each wing geometry.

Furthermore, material experimentation enables the refinement and calibration of semi-empirical methods, As understanding of a subject deepens, more numeric-computational approaches are developed to describe the problem. Consequently, this work also endeavors to be a source material for the development of numeric methods to describe the various aspects of the transition process to turbulence.

Lastly, as a motivation-consequence, this study aims to open the doors to bring Brazilian researchers, particularly those associated with the Experimental Aerodynamics Research Center - CPAERO of the Federal University of Uberlândia towards the forefront of aerodynamics research. Globally, only a limited number of research centers are focused on studying the transition process to turbulence, with even fewer situated in Brazil. Hence, this research, funded through the FAPEMIG project APQ-01589-21 ("INVESTIGAÇÃO EXPERIMENTAL DO FENÔMENO DE TRANSIÇÃO LAMINAR-TURBULENTA EM ASA RETA (2D) E ENFLECHADA) has the potential to set the stage for forthcoming investments and advancements in intellectual property. These advancements could bridge the gap and align us with the cutting-edge research conducted in aerodynamics institutes abroad.

CHAPTER II

2. PHENOMENOLOGY

2.1 The Linear Stability Theory

The Linear Stability Theory (LST) may be defined as the conglomeration of knowledge that elucidates the stability of flows in terms of the transition to turbulence during the linear phase of the process. It elucidates the types of instabilities that may be manifested in certain flow types and proposes a methodology for analyzing the linear aspect of the transition. Given the multitude of non-linear interactions inherent in turbulent flows and the transition process itself, it is crucial to emphasize that the Linear Stability Theory is applicable primarily to the initial stages of the transition, because In these stages the interactions can be predominantly treated as linear, ultimate objective of LST is to determine the frequency of the disturbances that may firstly be amplified into instabilities and where they may occur (SILVEIRA NETO, 2020).

Concerning the boundary layer, the LST considers the flow velocity as a composition of a mean profile supplemented by its corresponding fluctuations. Decomposing this system, it adopts the Orr-Sommerfeld equation, culminating in a diagram correlating the Reynolds number and the frequency of disturbances emission, unveiling the specific combinations of Reynolds numbers and disturbance frequencies at which amplification or attenuation would occur. The Orr-Sommerfeld is a linear and homogeneous equation, as also are the boundary conditions of the flows in which it may be applied. To solve it, an eigenvalue and eigenvector problem is formulated, amenable to solution through numerical and computational methods. The LST admits that the base velocity profile is parallel to the body surface (thus ensuring that the flow remains constant in the direction of disturbances amplifications) and that only minor disturbances are present, rendering non-linear effects are negligible. Additionally, LST incorporates the Rayleigh and Fjortoft theorems that establishing the prerequisites for turbulence to manifest in various flow types (see APPENDIX I).

It is imperative to emphasize that the Linear Stability Theory, despite anticipating the preliminary stages to turbulence, it does not constitute a theory for the turbulence itself, for it lacks the capacity to describe more advanced stages of turbulence. Moreover, it remains incapable of elucidating the fundamental cause for some process to happen in one way and not in the other. It just indicates what happens. In other words, the LST can be employed to ascertain the wave number of disturbances introduced into the flow, identifying the most amplified one that is most likely to be manifested as an instability. However, it is unable to precisely determine the underlying cause for this occurrence.

Nevertheless, it is a fundamental principle within Linear Stability Theory (LST) that the flow, influenced by pressure gradients, thermal effects, viscosity, and other factors, typically initiates without turbulent characteristics. In the context of canonic flows (flows that can be identified by distinctive specific characteristics), the turbulence process commences with the flow assumed to be laminar, and subsequently, due to various influencing factors, the flow may transition from the laminar state to the turbulent state. Some of the canonic flows includes free shear flow (subdivided into jets, wakes, and mixing layers), parietal flow (represented by the boundary layers), Rayleigh flow, and centrifugal flows (Taylor-Couette cylindrical type and Görtler boundary layer types). Despite their unique defining traits and distinct types of instabilities driving the flow state transition, all these flows can be analyzed under the framework of the Linear Stability Theory (SILVEIRA NETO, 2020).

Another common characteristic shared by all these flows is that for the transition to a turbulent state to initiate, it requires not only the injection of disturbances (exhibiting wave-like behavior), with a wide range of wavelengths, but also it also necessitates the amplification of these disturbances to start the transition process. These disturbances may appear due to mechanisms such as mechanical vibration, thermal energy, and numerous other factors. highly susceptible to transitioning into turbulence, all injected disturbances tend to undergo amplification. Although the precise reasons for this amplification are not fully comprehended, the flow, influenced by its physics, external conditions, and inherent flow characteristics, effectively "selects" a wavelength to be the most amplified one. Consequently, this wavelength is amplified at maximum rate, manifesting itself as an instability. The specific type of canonic flow determines the unique structure and behavior of this instability. Later, owing to the flow's instability, these instabilities may evolve into increasingly complex structures via non-linear amplification mechanisms. Then, these structures gradually intensify exhibiting harmonics and subharmonics of the wavelength that experienced maximum amplification, thus becoming increasingly pronounced until the flow reaches the turbulent state.

Regarding the boundary layer, for a certain period, there was a belief that it could not undergo transition since its velocity field did not exhibit an inflectional base profile, a fundamental requirement for the theorems proposed by Fjortoff and Rayleigh, which were utilized to determine the potential for transition. After the research conducted by Prandtl, and succeeded by his students Tollmien and Schlichting, it was finally demonstrated the occurrence of transition processes within this type of flow. The mechanism for boundary layer transition is described on next items.

Finally, to elucidate more advanced transition stages, alternative methods are emerging and gaining recognition and are beginning to be known as Nonlinear Instability Theory. Moreover, a hybrid approach utilizing a combination of empirical methods and LST can be employed to anticipate various stages of the transition process, including the transition front to turbulence. In the context of boundary layer flow, a calibrated blend of methods, validated through wind tunnel testing, includes the e^n Method. Additionally, the Orr-Sommerfeld equation is applied to bidimensional flows, with the application of the Squire Theorem extends the analysis to the three-dimensional realm (MENDONÇA and MEDEIROS, 2006). At APPENDIX II a concise and accessible overview of the Orr-Sommerfeld equation, the Squire Theorem, and the e^n Method.

With the LST s the foundational framework, next sections will describe the amplification disturbances processes and the transition to turbulence in boundary layers and specify the current understanding on its occurrences on straight and swept wings.

2.2 The Transition to Turbulence of the Boundary Layer

The boundary layer may be defined as the region of the viscous interaction between a fluid and a wall, in a relative movement, and due to this viscous interaction, it is a parietal flow. The velocity profile changes in the orthogonal direction to the body starting from a non-slip condition where the fluid is in direct contact with the body and shares the same velocity as the wall and increases until it reaches the free-stream condition. The distance between the point of non-slip velocity and the point where it deviates by 1% from the free stream velocity defines the boundary layer thickness. As the flow moves in a parallel direction along the body the boundary layer may gradually thicken and depending on the properties of the fluid, the free stream velocity and the wall roughness, the boundary layer may transition from the laminar to the turbulent state or even experience boundary layer detachment. Thus, the mechanisms for these possible events are caused by the viscous interaction mentioned before The mechanisms underlying these events are attributed to the before mentioned viscous interaction that provides, inside the boundary layer region, the exchange of information between the fluid and the body in form of diffusive and advective processes, causing the appearing of thermal and dynamic effects, manifesting as fluid dynamics forces and thermal fluxes (SILVEIRA NETO, 2020). Figure 2.1 illustrates the airflow boundary layer development from the laminar to the turbulent state on a flat plate.

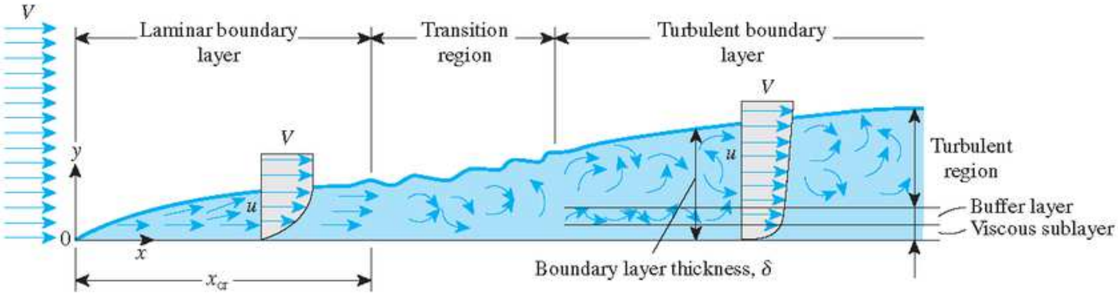

Figure 2.1: Boundary layer development on a flat plate (SCHLICHTING & GERSTEN, 2017).

Figure 2.1 shows the development of the boundary layer on a flat plate where, given a critical distance that corresponds to a critical Reynolds number, the transition process begins. Also, the thickness increasement of the boundary layer is perceptible.

It is important to emphasize that while viscosity may be an attenuation agent for the disturbances in the free shear flows, it plays a significant role in driving the transition processes in parietal flows. As already mentioned, for the transition to occur, disturbances with a large range of wavelengths must be inserted into the flow, and if there is a tendency for instability, the transition can occur. For boundary layers, the viscosity effects may transform the dynamic forces of the mean flow into other effects such as thermal energy exchange, attenuating the disturbances. However, the viscosity effect can also inject dynamic energy from the flow into the disturbances. If the energy rate transferred to the disturbances surpasses other transformation processes (such as noise and thermal effects), the flow is unstable, and the disturbances intensity can escalate and culminating in instabilities The precise mechanisms governing the transfer of energy from the base flow to the disturbances remain not fully understood. One plausible explanation is the involves the creation of vorticity next to the wall due to the non-slip condition and to the vorticity generation in proximity to the critical layer. The critical layer can be defined as the distance between the wall and the point where the disturbance phase velocity is equal to the mean base flow velocity. Thus, these vorticities would be responsible for the energy transfer from the base flow to the disturbances (SILVEIRA NETO, 2020).

Furthermore, an essential factor for predicting the possibility of a transition to turbulence is the Reynolds number, as it establishes a relationship between dynamic forces and viscous effects. A higher Reynolds number corresponds to greater inertial effects, making the flow more susceptible to initiating the transition process, since for higher Reynolds numbers the viscosity effects become less effective in attenuating dynamic forces. Hence, a critical Reynolds number can be defined to indicate that from this value on, the transition processes may begin and it is relative to the horizontal position of the flow on the surface in analyses, as shown in Figure 2.1 by x_{cr} (critical distance in x axis).

Therefore, considering that a parietal flow that presents the condition to amplify the disturbances as previously described, these disturbances amplified are manifested as the instabilities known as Tollmien-Schlichting (T-S) waves, named after the two researchers who first theorized these instabilities. The T-S waves are the first instabilities to be manifested in parietal flows and they correspond to the amplification of the disturbances that are selected to be amplified with the maximum rate. They can be characterized as transversal tubes with low amplitudes that rotate towards the wall, interacting with and being transported by the flow. Sustaining the initial conditions, as the boundary layer develops in space, transversal oscillations emerge over the T-S waves exhibiting a harmonic wavelength correlated with the initial T-S wavelength. Then, complex whirl structures known as hairpins, horseshoes, lambda, and delta are developed. These structures can be defined as counter-rotating whirl filaments which crests lifting towards the interior of the boundary layer due to the pumping of the fluid close to the parietal region to the central region of the flow (still within the boundary layer). This effect is further influenced by the translation and rotational movement of the flow relative to the filament, generating the Magnus effect.

At the valleys the descendent pumping effect promoted by the counter rotating filaments keeps them adhered to the wall. As a result of these crests and valleys movements, and as the spatial boundary layer continues to develop, turbulent spots with strong vorticity concentration may be formed, and as consequence this leads to intense matter flux from the region near the wall to the interior of the boundary layer. Finally, with an increase in the quantity and intensity of turbulent spots, the boundary layer flow is reorganized, culminating in a fully turbulent phase. The mechanisms of these amplifications are non-linear and not yet fully comprehended. Figure 2.2 represents the experimental development of the boundary layer instabilities amplification over a flat plate.

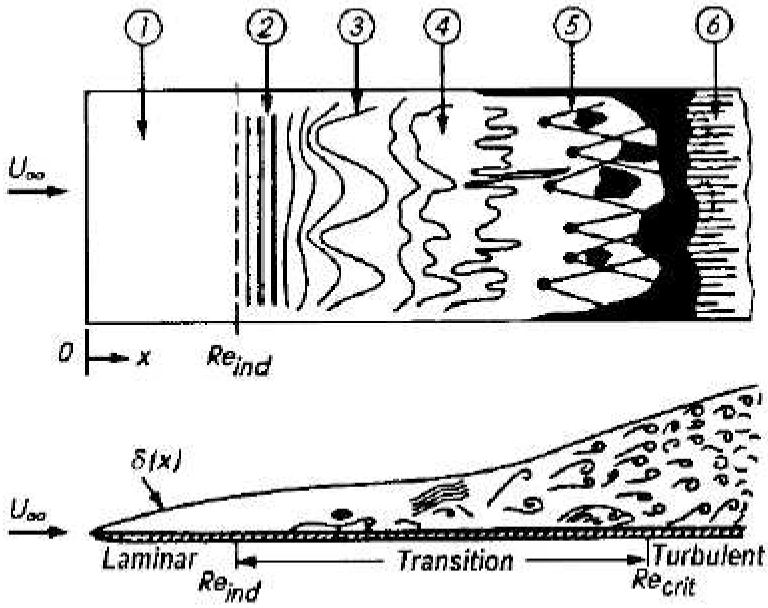

Figure 2.2: Sketch of continuous mode transition in a boundary layer on a flat plate at zero incidence (SCHLICHTING & GERSTEN, 2017).

Indices: (1) stable laminar flow, (2) unstable Tollmien-Schlichting waves, (3) three-dimensional waves and vortex formation (Λ-structures), (4) vortex decay, (5) formation of turbulent spots, (6) fully turbulent flow.

In the following sections, the concepts of straight and swept wings are elucidated to enable the definition of the instabilities that manifest in these wing types.

2.3 The Straight Wing

Historically, the straight wing was the initial wing concept utilized in aircraft design. Despite being a simpler wing type, even in contemporary times, numerous aircraft models are still designed with straight wings, particularly those not intended for high velocities or altitudes. Thereby, studying this type of wing is imperative not only because it constitutes a foundational issue for the swept-wing concept, but also because the straight wing remains a prevalent component in contemporary aircraft.

In most cases, the boundary layers formed on straight wings undergo transition primarily due to Tollmien-Schlichting (T-S) waves. Therefore, when the conditions necessary for transition are met, instabilities progress from the laminar state to the turbulent state through a process like the one outlined in the preceding section: disturbances introduced into the boundary layer may experience amplification, with the flow selecting a wavelength to be predominantly amplified into the Tollmien-Schlichting waves. As the air flows over the airfoil chord, Tollmien-Schlichting waves are conveyed by the flow, and non-linear processes take place between all the wave numbers that compose the flow leading to amplification of the instabilities Consequently, harmonics and subharmonics of the most amplified wavelength begin to emerge. As previously explained, increasingly intricate structures are manifested until turbulent spots become evident. With the breakdown of these turbulent spots, the turbulent regime is ultimately established.

However, even in the case of a straight wing, the wing's geometry is inherently more complex than the flat plate used to illustrate the transition problem in Sec. 2.2. The cross section of a wing is typically curved and an even display asymmetry along the chord. By employing the Linear Stability Theory and solving the Orr-Sommerfeld Equation for such cases may present greater complexity compared to the before mentioned scenario. but it is still possible to use them to find the critical Reynolds number and the Instability Diagram. Nonetheless, it remains feasible to use these methods to ascertain the critical Reynolds number and construct the Instability Diagram. Moreover, employing semi-empirical methods enables numerical computation to determine the transition point to turbulence. However, for the purpose of this study, which focuses exclusively on material experimentation, these techniques were not applied.

2.4 The Swept Wing

The concept of swept wings originated to enable aircraft to attain higher speeds that were previously hindered by airflow over the wing approaching supersonic characteristics. Due to the airfoil's shape, there are typically regions where the airflow accelerates, and locally, these regions may reach higher velocities than the external flow, manifesting supersonic characteristics. While these occurrences are often localized, they can potentially inflict significant damage or complications to the aircraft.

Thus, when a swept angle is applied to a wing, the flow velocity vector that reaches the leading edge which was previously parallel for non-swept wings, is now split into two components. One component is parallel to the wing leading edge and the other is perpendicular to it. The vector sum of both components results in the original velocity vector in terms of direction, sense, and magnitude. However, the orthogonal component to the wing, responsible for stablishing the critical Mach Number, now exhibits a lower magnitude for the swept wing when compared to the straight wing (assuming the aircraft is flying at the same airflow velocity and environmental conditions for both cases). Additionally, "the aerodynamic properties of the local section of the swept wing are now governed mainly by the flow normal to the leading edge" (BORODULIN et al., 2016 (a)). this design feature allows the airplane to attain higher velocities, as it reduces the critical Mach number for the same airfoil profile and airflow velocity. Also, the critical Mach has the characteristic of decreasing with temperature. Thus, not only swept wings allowed the aircraft to reach higher speeds, but they also allowed the airplanes to reach higher altitudes. Apart from these high advantages of the swept wing over the straight one, it is also important to mention that the swept case may have some disadvantages, as it is more complicated to either analyze or construct at structural, loads, aerodynamics, and flight mechanics views, and it presents higher construction and manufacturing costs. Beyond these significant advantages of swept wings over straight ones, it is important to acknowledge that the swept configuration may have certain drawbacks. It is more intricate to analyze, construct, and evaluate from structural, load, aerodynamics, and flight mechanics perspectives, leading to higher construction and manufacturing costs. However, despite these challenges, for most aircraft requiring higher Mach numbers, swept wings have supplanted non-swept ones due to the ability to achieve faster speeds and greater altitudes outweighing these complexities. For the application of the sweep angle to be effective in reducing wave drag at transonic speeds, usually common swept angles found in conventional transport aircraft may vary from 25º to 35º (BELISLE, 2013). Figure 2.3 illustrates the swept wing concept used in modern aircrafts.

Figure 2.3: Airbus A-380 aircraft. Source: https://www.superadrianme.com/travel/fun-facts-airbus-a380/

To illustrate the advantages of employing a swept wing concept, Anderson (2018 (b)) exemplified the augmentation of the Critical Mach Number with a swept wing compared to the straight case. In this example, a sweep angle of 30º was employed. Assuming that the critical Mach number for the straight case was approximately 0.7, the application of the sweep angle resulted in an increase of the critical Mach number to a value approaching 0.808. Figure 2.4 can be utilized to elucidate this example.

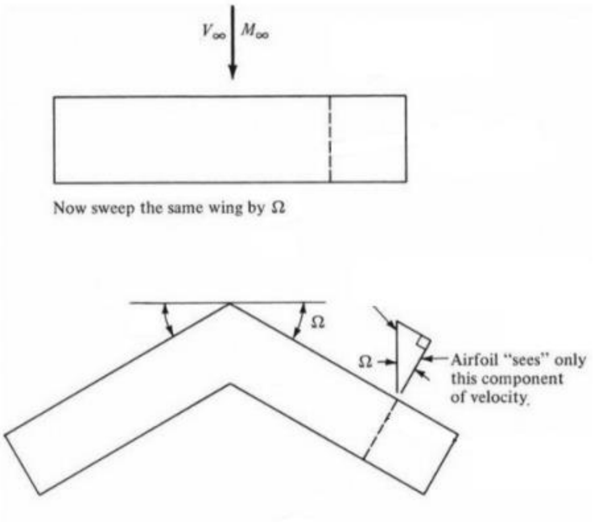

Figure 2.4: Effect of a swept wing on critical Mach number. Adapted from (ANDERSON, 2018 (b)).

Recapitulating, the velocity vector experienced by the wing is now, in the case of a swept wing, divided into two components. One is orthogonal to the leading edge, and the other one is parallel to it. While the perpendicular component initially exhibits characteristics like a straight wing, with the boundary layer corresponding to a similar case as described in the previous section the presence of the parallel component can significantly alter the boundary layer profile of the wing. Before the transition processes at straight wings reach a certain stage, the boundary layer, even with the presence of the T-S instabilities may be considered as a 2-D profile. However, with the sweeping of the wing and the new velocity vector, the cross flow emerges and thus, from the beginning, the boundary layer of swept wings is tri-dimensional, introducing another type of instability: Crossflow Instability (CFI). Additionally, based on the wing's geometry, there are two more instabilities that can affect swept wings: Görtler and Attachment Line instabilities (BELISLE, 2013).

Therefore, with the objective of offering comprehensive analyses of the transition on swept wings, the subsequent sections delve into the theory of the transition mechanisms affecting swept wings. The LST, was previously elucidated since it is the basis of the transition study and describes the first observed transition mechanism on the boundary layer wings, the T-S waves. Later, the concept of the straight and swept wing is shown to give space to the presentation of the transition mechanisms relevant to this study.

2.4.1. Tollmien and Schlichting Instability

The Tollmien-Schlichting (T-S) instabilities, as the most elementary form of boundary layer instabilities, have been described in previous sections. Consequently, given their occurrence in the boundary layers of flat plates and straight wings, they manifest in the boundary layer of swept wings as well. However, due to the presence of other types of instabilities in the swept case, it is crucial to acknowledge that the initiation of transition may not be exclusively driven by the development of T-S waves. The decisive factor lies in the selection of the most amplified instability by the flow. Nonetheless, since the transition process results from the interaction of complex structures, it is possible that other instabilities promote the development of the T-S waves prematurely, in comparison to the scenario where the T-S waves acted alone. The specific outcome hinges on various factors including the Reynolds number, surface roughness, airfoil camber, sweep angle, other wing geometry characteristics, and environmental conditions (DAGENHART and SARIC, 2019).

In summary, the T-S waves are fundamentally structures that are advected by the boundary layer progressing from the leading edge to the trailing edge, the streamwise direction. Their amplification occurs under a positive pressure gradient in the streamwise direction, and they exhibit a high sensitivity to acoustic and vortical disturbances in the free stream. As these structures travel downstream, they grow in amplitude as the advection velocity decreases due to the thickening of the boundary layer. Consequently, vortex structures in proximity can collapse on each other merging, generating larger whirl structures at double wavelength, a phenomenon known as vortex pairing. Then secondary mechanisms cause the flow breakdown, creating complex structures that cannot be referred to as presenting a two-dimension characteristic anymore signifying the attainment of a turbulent state.

2.4.2. Cross Flow Instability

The Crossflow Instability (CFI) manifests in the orthogonal direction to the wing. This velocity component triggers the formation of co-rotating whirl structures that are aligned with the flow direction and known as crossflow vortices (CFV). In regions where the flow is accelerating, these structures may increase in amplitude, traveling on the spanwise and streamwise direction when the streamwise turbulence direction is high, or they remain stationary when the streamwise turbulence direction is low. This behavior is distinct from the T-S waves and their amplified modes, which propagate solely in the streamwise direction. This effect also induces the CFV amplitude to increase when approaching the trailing edge. Moreover, the CFV can act as secondary mechanisms, accelerating or inducing the transition to turbulence in the streamwise direction by altering the mean flow field (SERPIERI, 2018). The crossflow profiles inherently possess at least one inflection point, rendering them unstable to disturbances with a wave vector oriented approximately in the crossflow direction. As detailed in APPENDIX I, inflectional points, besides not being sufficient to the turbulence to initiate, are mandatory for the transition in certain flow types, and now they enable the emergence of inviscid instability modes at the boundary layer, augmenting the instability characteristic of the boundary layer. These modes may exhibit a traveling or stationary nature. Usually, for sweep angles until 35º it is expected a predominance of stationary modes, while for higher angles it is expected a predominance of travelling modes. Figure 2.5, represents a schematic comparison between both T-S waves and CFI in terms of their directional behavior within the wing boundary layer.

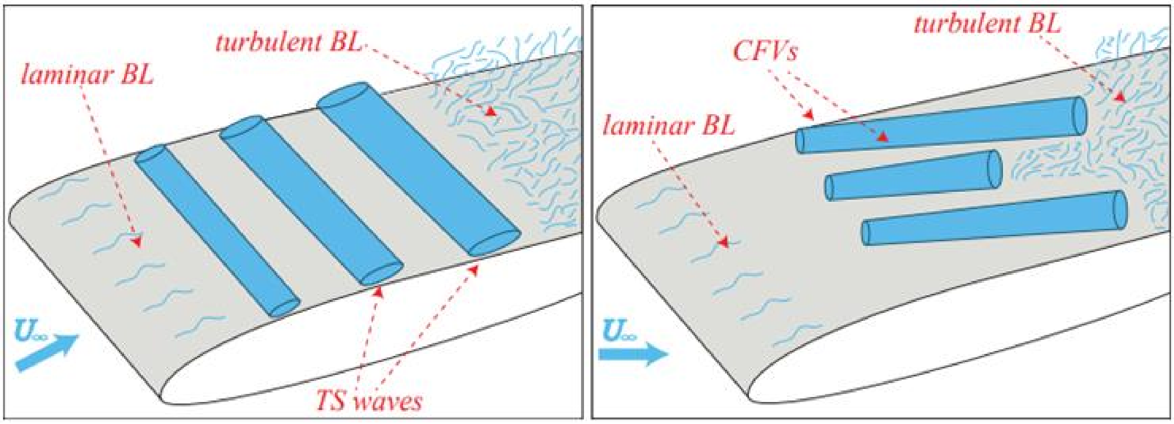

Figure 2.5: Schematic comparison between both T-S waves and CFI path over the wing. Adapted from SERPIERI, 2018.

Therefore, considering a streamline over the wing, the crossflow arises from an imbalance between the force equilibrium in the orthogonal direction to the streamline and the force parallel to the surface. These forces are represented by pressure forces and may cause an imbalance between the centripetal acceleration and the centrifugal ones which attempt to tear the wind particles out of the streamline. This imbalance occurs due to the momentum deficiency within the boundary layer, resulting in air particles moving perpendicularly to the streamlines.

Comparing the contribution of the T-S waves and the CFI to the turbulence transition processes, an early analysis may be made concerning the magnitude of the sweep angle and the pressure gradient. Thus, for favorable negative stream wise pressure gradients exhibiting an inflection point in the velocity profile, and sufficiently large sweep angles the predominance of the stationary or traveling CFI is expected. For low turbulence conditions, the stationary CFI are predominant, while higher turbulent environments are more conducive to a travelling CFI. However, for weak chordwise adverse pressure gradients, the T-S waves influence may be predominant (BORODULIN et al., 2019 (b)). Figure 2.6 represents the wing (consider it to be with a swept angle applied) demonstrating the velocity profiles of both orthogonal and parallel components, along with the directions followed by the T-S waves and the CFI. Additionally, it is possible to verify the inflectional characteristic of the medium velocity profile in the spanwise direction due to the crossflow.

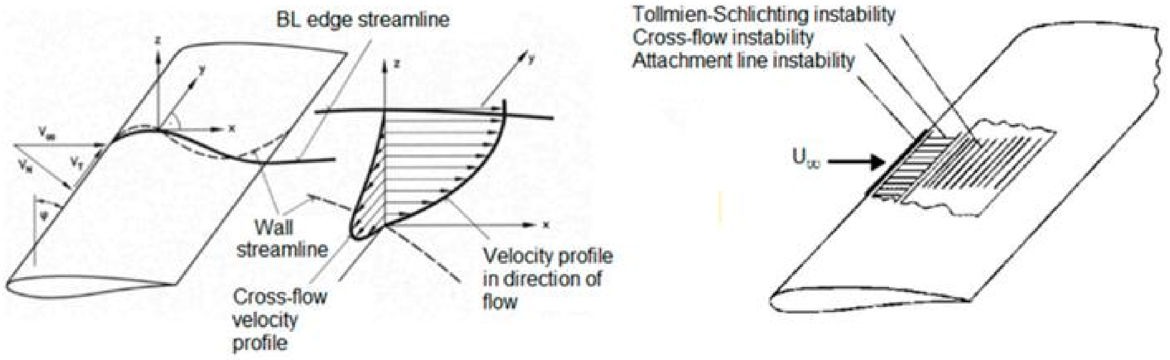

Figure 2.6: 3D Boundary Layer on a Swept Wing and Transition Mechanisms (BECK et al., 2018).

2.4.3. Görtler Instability

This instability arises due to the combined effects of centrifugal and parietal influences. It happens inside the boundary layer in secondary flows specifically when the wall is concave, and the boundary layer thickness is comparable to the wall curvature. In a stable scenario, a centrifugal force field emerges owing to the wall curvature, countered by a pressure gradient directed from the wall towards the center of curvature. The disruption of this equilibrium can lead to the appearance of Görtler instabilities, exhibiting a counter-rotating behavior (SILVEIRA NETO, 2020). A schematic representation of Görtler instabilities is depicted in Figure 2.7. For Görtler instabilities to manifest in wings, a prominent airfoil camber is typically required, or at the very least, some section of the airfoil must exhibit a concave geometry. In conventional wing designs, if these instabilities are manifested, the concave part of the airfoil is usually situated on the lower surface. However, as it will be further elucidated, the wing model tested in this work is symmetrical, lacking the concavity necessary for the development of Görtler instabilities.

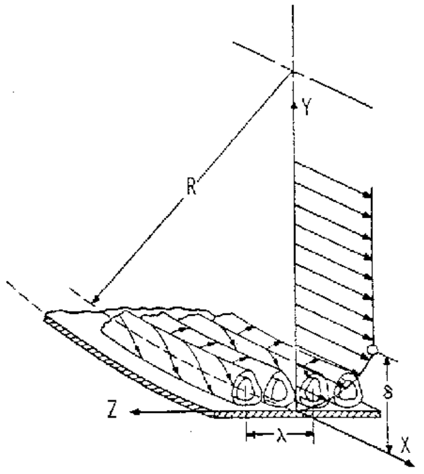

Figure 2.7: Görtler instabilities scheme. Seeding of Görtler Vortices Through a Suction and Blowing Strip (SOUZA et al., 2004).

2.3.4 Attachment Line Instability

This transition mechanism can occur on swept bodies when the curvature of the leading edge is significant, resulting in a ratio of leading-edge thickness to wing chord greater than 1%. It appears due to the splitting of the airflow that reaches the leading edge into the upper and lower surface of the wing and acts in the spanwise direction can lead to the formation of a boundary layer along the attachment line, which may become unstable and contaminate the overall boundary layer right from the beginning. Especially at scaled wing models used for wind tunnel testing, the possibility of this transition mechanism occurring should always be considered. Then to prevent the occurrence of the so-called attachment line transition, when projecting the test model, the wing leading edge thickness ratio relation to the chord length must be at least 1%. In complete aircraft models, the Attachment Line instability may also appear in the junction of the fuselage to the wing, propagating in the span direction and contaminating the boundary layer of the wing (SERPIERI, 2018). Given that the present wing model is a stand-alone wing and the ratio of leading-edge thickness to wing chord exceeds 1%, this type of instability should not develop.

Considering the described instabilities affecting swept wings, the following chapter provides an overview of the latest works of the community regarding the research of the boundary layer transition on wings, giving a highlight to swept wings and how the transition problem is being treated on material experimentation. Also, at APPENDIX III an overview focused on the construction of the models of wings for scaled wind tunnel testing is presented.

CHAPTER III

3. BIBLIOGRAPHIC REVIEW

During the last years many researchers have not only sought to identify the transition front to turbulence on wings, but they have also proposed mechanisms for active or passive boundary layer control. The identification methods encompass numeric-computational approaches, wind-tunnel testing or even flight test campaigns. In this section, some studies published within the last seven years are summarized. They have been chosen based on their year of publication and the material experimentation techniques employed for boundary layer transition detection. The intent is to present the latest advancements in the field of boundary layer detection and/or techniques for visualizing and quantifying the transition phenomenon in some cases. It is important to emphasize that some studies herein presented have studied mechanisms for boundary layer control. Although this is not the primary focus of the current work, they have been included to contextualize the potential of the present study, since the identification of the transition front may be necessary for employing more effective active transition control methods and it is noteworthy that some of the studies aiming to develop control methods also involve the identification of the boundary layer transition front. Other works are also presented due to the utilization of infrared thermography for the detection of the transition front or for registering the boundary layer control mechanism effectiveness.

Borodulin et al. (2016) tested the utilization of Distributed Micro-Sized Roughness elements (DMSR) to control the transition to turbulence on a swept wing model. The main idea is to use these elements to introduce controlled stationary vortices to modify the base flow and thus its stability characteristics. They have tested some configurations of the DMSR in three configurations for the wind tunnel turbulence: with a clean wind tunnel configuration, with noise (to insert perturbations) and with grids to induce a turbulent regime in the flow. For the clean configuration the DMSR has shown to retard the transition point, while for the turbulent generation grids the DMSR did not show to be effective since the turbulence transition point has moved upstream. For the disturbances induced by noise, even without the DMSR the transition point did not move. All the experiments have been recorded by an infrared thermography camera so that the transition process could be noticed. Then, an image post-processing technique has been applied to improve the visualization of the phenomenon. The wind tunnel used is a low-turbulence one of turbulent intensity registered to be under 0.02 %. It has a test section of 4 m x 1 m x 1 m. The wing model is based on a modified NACA 671-215 airfoil with 0,7 m of chord, 1 m of wingspan, 45º of sweep angle and has been placed at -5º of angle of attack to provide an extended region for the flow acceleration and thus to provide a predominance of the crossflow instability. Regarding the infrared thermography, the wing model has been heated by a designed heater to increase the contrast between the wing and the flow. The image captured occurred by the recording of a thermogram sequence at a rate of 100 frames per second during 45 to 60 seconds of which 20 seconds are used to the flow stabilization after the wind tunnel is on. After that, the image post processing has been applied: the image is rotated, the background is extracted, and board detection methodology (Canny Methodology) is used to identify the transition since it is seen at the area of contrast between the high and low cooling rates.

Also studying a flow control method, Serpieri (2017), for his PhD thesis for Delft University of Technology studied the instability phenomenon that occurs during the boundary layer transition to turbulence of swept wings. The active control method proposed was based on conditioning the boundary layer via alternating current dielectric barrier actuators. Therefore, his work focused on the observation of the first and second modes of the crossflow instabilities and their stream wise evolution. For the first modes instabilities he applied an oil film visualization to trace the vortices instabilities, hot-wire anemometry and three-component three-dimensional particle image velocimetry (tomographic PIV) for the boundary layer determination. The manufactured wing has been placed at an angle of attack of 3º, with an infinity velocity of $25{,}6\,m/s$ (equivalent to a Reynolds number of $2{,}17 \cdot 10^6$. Also, he forced, in the leading edge, through roughness elements the critical stationary mode to appear with $\lambda = 9\,mm$. With the oil film visualization, it was possible to estimate the position of the transition point (found to be next to x/c = 0.5). With this value Serpieri could find the best positions to apply the boundary layer determination techniques to observe the velocity profile evolution and the actuation of the crossflow instabilities. The PIV technique could also provide the vortex spatial organization. When comparing the boundary layer results between PIV and hot wire anemometry, he concluded that for heights too close to the wall the PIV resulted in wrong measures while for heights further from the wall the hot-wire and PIV presented similar results. Finally, applying the LST numerically computed over the measured pressure field, he could compare the experimentally measured boundary layer to the computed one. Regarding the flow control, the proposed idea was to force some selected crossflow instability mode via plasma actuators to introduce unsteady fluctuations in the boundary layer and thus to amplify them at frequencies that are lower than the ones selected to be amplified by the flow. Therefore, the primary modes should be less amplified, and the transition process retarded. The wind tunnel installation is a closed circuit one with 1.25 m x 1,80 m x 2.6 m of test section. The swept wing tested had 1,25 m of wingspan, 1,27 of chord and the airfoil corresponded to a modified NACA66018.

Giving one step ahead in terms of material experimentation, Kurz (2017) for his master's degree thesis studied the application of plasma dielectric actuators to control the boundary layer transition via in-flight test and wind tunnel testing. Therefore, for the flight testing a wing glove has been developed and attached to the wing of a single engine aircraft (model GROB G109b) with the possibility to also be placed inside a test section for wind tunnel experiments. It has been developed after a laminar wing with cross section of the modified airfoil BU84-158. A disturbance source has been integrated to the wing glove to generate the desired disturbances so that the transition process could happen accordingly. Plasma actuators have been chosen for their fast response and compact design besides the absence of moving parts that can influence the flow destabilization. The wind tunnel experiments were conducted at the ONERA research facilities in Toulouse. Its turbulent intensity was between $0.5 \cdot 10^{-3} < Tu < 0.5 \cdot 10^{-2}$ for a free stream velocity between $5\ to\ 75\ m/s$. Surface hot-wire sensors were attached to the wing glove aiming to capture the T-S waves amplitude and phase so that the plasma actuators could properly act. His results have shown a delay on the boundary layer transition for both in-flight and wind tunnel cases.

Hoesslin et al. (2017) applied a temperature decline method using infrared thermography to qualitatively detect the laminar to turbulent transition of the boundary layer and to find the respective heat transfer coefficients. The tests were conducted on a wing based on the NACA0018 airfoil with 51 mm of chord. The image results have been computationally post processed to find the transition point and the heat coefficients. To validate the results, hot film measurements have also been done. The model surface has been coated with a low thermal conductivity but with high emissivity material and heated by light radiation and has been tested for some configurations of Reynolds number and angle of attack.

Aiming to evaluate a numeric-computational method for the utilization of plasma Dielectric Barrier Discharge actuators (DBD) to control de transition caused by cross flow instabilities in boundary layers of swept wings, Wang, et al. (2018) also have conducted material experimentation. The numerical approach consisted of a nonlinear parabolized instability equation (NSPE) method. The tested wing cross section corresponds to the NFL-04015 airfoil, and was projected with 45º of sweep angle, 1,2 m of chord an 1,2 m of wingspan and the wind tunnel where the experiments were conducted has a test section of 1,2 m x 1,2 m x 3 m. The plasma actuators have been placed close to the leading edge. Thus, the idea is to use the plasma actuators to generate disturbances to counter pose the CF vortices modes that influence the transition process and thus to reduce their energy retarding the process. Finally, they have tested the actuators to generate the control disturbances in a harmonic and subharmonic manner. For the first case they concluded that it only works if the actuator acts on the opposite of the disturbance velocity, otherwise it can even enhance it. For practical applications it is not robust enough because it is difficult to be precise about the location of the disturbance. For the sub-harmonic case, when exciting the sub-harmonic mode (and thus not aiming the prime mode) the CF has been weakened, suppressing the prime mode, and demonstrating a good efficiency on this technique.

Continuing in the realm of comparative material experimentation and numerical-computational simulations, Beck et al. (2018) investigated methods to reduce viscous drag within a boundary layer section, aiming to establish a laminar regime across a broader area. They applied it to all the aircraft wetted areas, that included a generic fuselage model associated with some airfoil profiles. Their results have shown that, for instance, for the supercritical airfoil DLR F15 at Mach 0.7 and Re = 3000000, the applied suction has retarded the transition of the boundary layer by 85%. However, due to some hypothesis considerations, the authors affirm that the results are quite conservative.

Gleichauf et al. (2021) studied the application of post processing image technics for thermography flow visualization aiming to identify the transition to turbulence on wind turbines in operation, since a method to artificially change the temperature contrast (by heating or cooling the rotor) is not applicable in this case. The tests, though, have been conducted with a cylinder and a wing built after a DU96W18 airfoil as models in a wind tunnel facility. However, no precooling or heating have been used. Thus, there is the proposition to take a series of IR images of the transition phenomenon and post-process it to reduce the noise of the image and increase its contrast by evaluating the difference on the temporal fluctuations between the images registered on the series taken. The post-processing image treatment suggested is based on the principal component analysis (PCA) that is already used on structure thermography analyses but not yet used for flow thermography analyses. It evaluates the spatial and temporal image information, in this case, associated to the temperature of the model's surface, especially at the transition to turbulence border of the boundary layer, and differently from other already used methodologies, it does not assume a harmonic base when treating a series of images.

As shown in previous references, the idea of contrasting numeric-computational results to material results is of great matter. Thus, Boiko et al. (2021) studied the determination of the transition front of the boundary layer in a swept wing via thermographic camera and compared the experimental results with a computational simulation performed with ANSYS Fluent. Then, the calculated velocity profiles were used for hydrodynamic analysis or the stability of the boundary layer to implement a N-factor model regarding the evolution of the Tollmien-Schlichting instabilities and the crossflow instabilities. The wind tunnel where the experiments were conducted is a subsonic one with a test section of 1 m x 1 m x 4 m the turbulence level was 0.02 %. The swept wing model had 45º of sweep angle and has been tested at zero degrees of attack angle. It has a cross-section after a NACA 67 1-215 with 0.7 m of chord length. It was built in acrylic, and its interior is filled with a ribs and stringers system to guarantee a rigid model. Finally, the test velocities varied from 10 m/s to 50 m/s. For the thermography visualization, the model has been pre-heated to present a better contrast in the infrared images. The heating system consists of 15 W halogen bulbs spread uniformly along mirrored panels. The images have been taken in sequence frames of 50 fps up to 70 fps instead of just single frames.

As present in the previous section, the attachment line can contaminate the boundary layer and conduct the flow to turbulence early then it should. Therefore, Methel et al. (2022) tried a method for laminar flow control for preventing the wing’s attachment line contamination by turbulent structures for when the wing is attached to a wall, such as in-flight and in various wind tunnel conditions. This becomes a problem because if the wing flow is contaminated since the attachment line, and proper conditions are met, the flow over the wing will become turbulent from the beginning, increasing the drag force over the wing if compared to a non-turbulent flow. For studying the flow control, they have experimentally tested in a subsonic closed circuit wind tunnel with a test section of 1.8 m x 1.8 m x 1.4 m a swept wing model applying techniques of infrared thermography and hot film measurements for the determination of the transition front and its characterization. The velocity during the experiment varied from 5 m/s to 85 m/s with low turbulent levels to not allow previous turbulent contamination on flow over the model due to the freestream flow. The tested model has been specially developed for the study of the attachment line transition and contamination, consisting in a semi-cylindrical leading edge of 0.2 m of radius and extended by straight side panels completing a chord length of 1.2 m, where a 50º of sweep angle has been applied. The flow control method applied consisted of the suction of the flow by chambers placed along the leading edge.

For passive flow control, Zoppini et al. (2022) used discrete roughness elements for the conditioning of the boundary layer on a swept wing model. They tested some configurations of the elements regarding their height and chordwise locations. The methods applied counted on experimental and numeric-computational approaches to predict the transition front to turbulence and quantify the transition characteristics. Thus, experiments of infrared thermography and planar particle velocimetry have been applied while in the numerical field, simulation analyses based on nonlinear parabolized stability equations, all to reconstruct and analyze the growth of the crossflow instabilities.

Eguea (2022). has experimented in his PHD thesis the influence of a propeller in the transition front to turbulence of boundary layers at a laminar straight wing model for the combinations of distances of the propeller to the wing and different propeller velocities. For comparison, he also tested the clean wing, without the utilization of a propeller, which happens to be the same wing in which the present swept wing model was based on. The straight wing model of 1.3 m of wingspan and 0.5 m of chord has been manufactured in aluminum and tested in a blow down, low-speed closed-circuit wind tunnel facility with a test section of 1.68 m x 1.29 m x 3.00 m. Thus, the model with the propeller position variations has been experimented under a pressure transducer for obtaining the pressure distribution and under an infrared thermography camera for obtaining the position of the transition front to turbulence. The IR images obtained were then treated by a Python image process code for a better detection of the transition front. The straight wing IR images that are used to compare the swept wing results of the present work have been extracted from the work just mentioned.

All the before mentioned works have been introduced due to their pertinence to the experimental analysis of boundary layer transition from laminar to turbulent states, with a particular focus on swept wings and the application of infrared thermography as a visualization technique, whether coupled with flow control mechanisms. The subsequent works presented in this section continue to concentrate on transition determination, employing either numerical-computational approaches or experimental methodologies, as well as exploring various flow control techniques. While some of these works extend beyond the past six years, they exhibit noteworthy features that justify their inclusion and discussion. They serve as exemplars of alternative perspectives to be considered for future research endeavors, such as numeric-computational approaches and flight testing.

Studying passive flow control, Zhang and Yin (2019). used of riblets to decrease the surface drag on swept wings with the riblets disposition depending on the riblets angle to the flow. The work has been conducted via computational methods and validated by previous experiments from the same authors. They have simulated a channel flow and a considered infinity swept wing with 30º of sweep angle. For first, they have concluded that with the increasing of the inclination between the riblets and the flow, the friction drag decreases while the pressure drag increases almost in a quadratic way. Regarding the swept wing, two cases were simulated, one with the riblets and one without it. However, the simulation resulted in a cross flow that was not strong and so the conclusion is that the crossflow was, and the turbulence fluctuation is suppressed by the riblets resulting in a reasonable friction drag reduction while like the channel flow case, the pressure drag has also increased.

Another famous technique for flow control is blowing air jets at specific locations on the wing. Then, Hirokawa (2020) studied the reduction of the friction drag on a straight wing by passive blowing. Their work happened in both wind tunnel testing and with computational simulations. The straight wing which cross section corresponds to the Clark-Y airfoil has 0,4 m of chord and 0,548 m of span. The Reynolds number tested were $0{,}65 \cdot 10^6$ and $1{,}55 \cdot 10^6$. To generate the blow in a passive way, a tubular system has been installed, which near the leading edge generates a suction area and conducts the suctioned flow to an exhaustion area near the trailing edge. Thus, the pressure differential allows the air injection with no need for an active mechanism. Results have shown that the velocity profile over the wing has been modified due to the air injection with a decrease of the frictional drag consequently. Between the wind tunnel testing and the simulations some differences in the results were noticed and they argued that it is due to the blockage ratio between the model and the wind tunnel test section.

Also concerning about the attachment line contamination, Aldeman and Rolston (2016) proposed the utilization of a small device called Gaster Slot. It as a passive control flow device that would not allow the contamination of the leading edge to turbulent structures, maintaining the boundary layer on the wing or at least a portion of it is as laminar. Thus, a swept wing model has been experimentally tested. Two models of 40º and 45º in aluminum have been manufactured with a better superficial treatment applied to up to 10 % of the chord. The wing was placed in the wind tunnel test section at a six-component aerodynamics balance and coupled to a turntable to allow different angulation. Endplates have been attached to allow a 2D hypothesis.

Kleinubing et al. (2013) proposed an experimental methodology to visualize the transition phenomenon via an infrared camera. Since the thermal interaction that happens on the turbulent boundary layer is different from the one that happens on the laminar one, the infrared camera is supposed to be able to differentiate the laminar to the turbulent flow. The proposition of the infrared camera is due to the reason that it is a non-invasive method and thus it shall not influence the transition turbulence process. The wind tunnel is the same as the one used by Eguea (2022). Two straight wings have been tested. The first one has been manufactured after a NACA0012 airfoil with 1,50 m of chord and the second one after a supercritical airfoil with 1 m of chord. Both with the same span of the wind tunnel so that they can be considered as a 2D representation and were placed at 5º of angle of attack with the flow infinity velocity set to 28 m/s. Vortex generators have been coupled to the leading edge to allow the transition process to happen. For comparison matters on the transition point location, a flow-viz technique, and simulations in XFLR5 software have also been accomplished. The models had been heated to allow a better contrast between the flow and the surface and aluminum stripes were attached to the model to serve as markers along the wing chord for the infrared visualization. Because of a higher energy transfer capability of the turbulent boundary layer, and since the infinity air flow is cooler than the surface it has been observed a sudden cooling on the turbulent part of the flow.

Merz, Richter, Raffel (2014) experimentally tested the utilization of a high-rate infrared camera to register the boundary layer transition location. They have applied the differential infrared thermography method (DIT) for transition detection, which consists of the image intensity difference between two subsequently recorded images. This technique is used to find the temporal temperature gradient and so the instantaneous position of the transition when a pitch rate is applied. Their results were then compared to CFD simulations based on the e^N transition prediction methods. They have heated the model for a better contrast in the image acquisition via radiation with a tungsten filament spotlight. The halogen had 2000 W of power and counted with a parabolic reflector. The wing model has a NACA0012 as a cross section with 0.3 m of chord and 1 m of span and was built with carbon fiber. The wind tunnel is an open section blowdown model of 1.05 m x 0.7 m x 1.5 m. The infinity velocity was set to be 50 m/s with a Reynolds number of approximately 10^6. Also, the wing leaves some space between the wind section walls so that the flow cannot be considered as 2D near the free ends.

As the lest review, Crawford et al. (2013) used infrared thermography for the boundary layer transition detection of swept wings in both wind tunnel and flight test fields and have also compared the results between the technics of infrared and naphthalene flow visualization. The motivation for using the infrared visualization instead of the naphthalene is reasoned on the fact that although the naphthalene approach provides good results (because the turbulent region sublimates faster than the laminar, creating a different pattern of the residual substance on the wing surface), it must be applied all over again for every desired test point to be measured, besides from requiring a complete sublimation of the compound. Regarding the IR thermography three experiments have been proposed to test two infrared techniques: the first one was cooling the model for in-flight test and the second was to heat it for wind tunnel testing and in-flight testing, both aiming to increase the contrast of the image capture. For the cooling in-flight, the model has been attached to the aircraft wing, and for the cooling process it has been soaked into the temperature equivalent to 3200 m MSL until the infrared image shows that the temperature is equalized to the atmosphere. Then, the aircraft dives to warmer air at a lower altitude until a good temperature differential is reached. About the heating technique, the swept wing model has been covered with a heating sheet. Both models were built in aluminum and coated with a thin insulated layer to hold a strong temperature gradient, but that presents low reflectivity in the infrared band as possible. Comparing both in-flight conditions, for the cooling approach, after cooling, the aircraft must dive quickly to be able to test the desired points. Then, it must climb again and then keep cooling it for at least 20 minutes, while the heated model does not need this step but requires the heating sheet apparatus that must be integrated into the model. Nevertheless, it saves a lot of flight costs. Both cases provide good results with the only observation that the intensity of the color registered for the turbulent and laminar parts of the boundary layer is inverted. Regarding the comparison between the infrared and the naphthalene visualization, the major difference is the efficiency of the thermography technique since it shows almost instantaneously the transition front. After all the experiments have been accomplished, the images have been treated under post-processing to better evaluate the transition front giving each pixel a temperature value.

CHAPTER IV

4. METHODOLOGY

This chapter is dedicated for presenting the experimental design of the swept model, including its manufacturing process, the project variables considered in the study of boundary layer transition, the laboratory facility and equipment employed, a description of the experiments conducted with the swept wing model (including the determination of pressure fields, aerodynamic forces, and the detection of boundary layer transition via infrared thermography), and the methodologies applied for each of these experiments. However, before introducing the swept wing model, a summary of the straight model in which it was based is next presented.

4.1 Swept Wing Model Construction Background

To analyze the transition front to turbulence of the swept wing model and then compare its results with the straight wing case regarding only the sweep angle, the swept and straight models must present the same aerodynamics characteristics, with the only difference between them being the sweep angle itself. However, to enhance both the quality of results and the experimental setup, manufacturing modifications, derived from the insights gained from the previous case are applied on the swept case.

Before delving into the features of the swept wing, it is necessary to provide a summary of the characteristics of the straight wing. This summary serves the purpose of ensuring a more accurate determination of the transition point while mitigating potential sources of contamination, such as those arising from the wind tunnel test section boundary layer and wing tip effects. The straight wing design prioritized the maintenance of a laminar airflow profile along most of its chord length. To achieve this, an optimized symmetrical airfoil profile based on the NACA3609 was employed, and it is presented on Figure 4.1. Its coordinates can be found at APPENDIX VI .

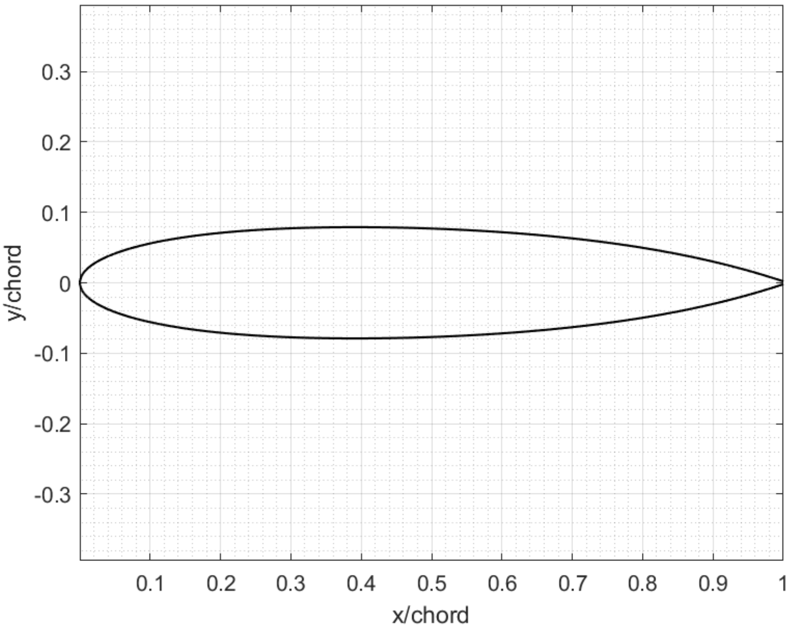

Figure 4.1: Laminar Airfoil (3609) based on NACA's series.

To isolate or at least mitigate three-dimensional effects and simplify the model, the wingspan of the straight wing matches the height of the wind tunnel test section, following the infinite wing hypothesis, presenting a wingspan of 1.3 m and a chord length of 0.5 m. Also, no aspect ratio, torsion angle, or other aerodynamic devices have been applied. The model was designed using CATIA software and manufactured from an aluminum alloy. Subsequently, the model surface underwent a machining process to ensure the smoothest surface as possible. To the pressure field characterization experiment, 64 holes of 0.2 mm of diameter were drilled allowing the passage of the pressure taps. These pressure taps were installed through three hatches on the lower surface of the wing. Also, the interior of the model is hollow, with a small section housing three strings and three ribs that were also machined into the model. Further details regarding the straight model can be found in

Eguea (2022). Thus, two primary experiments were conducted on the straight wing model: pressure field characterization and determination of the boundary layer transition point using infrared thermography. In the pressure transducer experiment, the pressure taps were positioned near the lower end of the wing and connected to the pre-drilled holes mentioned earlier. These taps were connected to a Scanivalve, which interfaced with the pressure acquisition system. For the determination of the boundary layer transition front determination, a white plastic covering was applied to the wing surface to reduce the aluminum reflectivity and enhance thermal energy absorption, thus improving the quality of the infrared images. To aid in identifying the transition front location, silver reflective paint markers were placed from every 10 cm along the airfoil chord. Figure 4.2 represents the installation of the pressure taps inside the wing model.

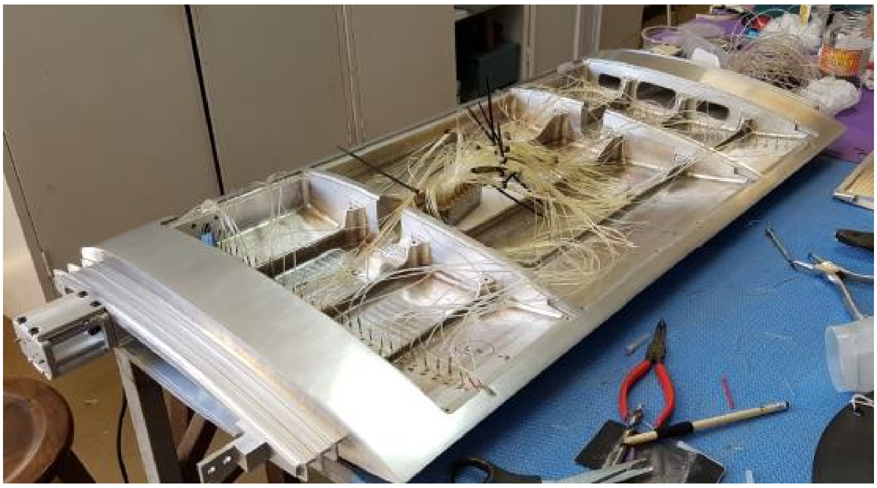

Figure 4.2: Straight Wing configuration for the pressure taps assemble (EGUEA, 2022).

4.2 Swept Wing Model and Manufacture

Differently from the straight model, the swept one was fabricated in fiberglass through a lamination process. The choice of a composite material was driven by its ability to combine low weight with high structural strength. The shift from aluminum, which is not only more costly but also significantly heavier, was motivated by the need to facilitate the installation of the model in the wind tunnel. Furthermore, fiberglass offers improved thermal energy absorption properties, contributing to enhanced contrast in the infrared images obtained during the experiment. Thereby, to ensure that the wing could withstand the aerodynamic loads, it was constructed with internal walls measuring 5 mm in thickness. Also, two aluminum circular bars of 1.3045 m in length and with an external diameter of 5/8 in, were placed along the wingspan to serve as structural strings. To enhance its resistance to torsional moments, two wooden ribs, each of 5 cm in thickness, were internally affixed parallel to the airfoil profile along the chord. The top of the wing features an additional wooden rib, measuring 10 cm in thickness and covered by the fiberglass shell to provide heightened structural support. Similarly, the wing base is also constructed from wood, with a thickness of 15 cm.

The model is secured to the equipment using screws that establish a connection between the wooden base and endplate of the wind tunnel. While the use of a wooden base minimizes the risk of wear and tear on the fiberglass during attachment and detachment, as fiberglass can degrade due to screw movements, additional measures were taken to ensure the most secure fixation possible. Two aluminum discs were affixed to the wooden base, serving as intermediary components to link the screws with the rest of the equipment. This design choice guarantees that the model can be assembled and disassembled multiple times with minimal or no degradation, thereby allowing its reuse in future experiments.

To allow the installation of pressure taps, a single access hatch was integrated, in contrast to the three hatches used in the previous model, since the pressure taps are now positioned in the middle of the wing, requiring only one access point. Also, a hole was drilled through the wooden base and the initial wooden rib to accommodate the passage of the pressure tubes from the exterior to the interior of the model. The hatch is affixed to the rest of the wing using screws and again, instead of fixing it through a metal-to-fiber contact, a specialized aluminum nut is adhered within the holes created for screw insertion. The model has been coated with black paint and subjected to a surface treatment to not only ensure the smoothest possible surface but also to minimize reflectivity and enhance thermal energy absorption. Consequently, the use of white plastic, as employed in the previous model, is no longer necessary. Furthermore, the interior of the model has been painted with black paint aiming to maintain the radiated energy absorbed for a longer time. Figure 4.3 represents the swept wing model.

Figure 4.3: Swept wing model.

The wing dimensions of chord, wingspan (parallel to the wind tunnel wall) and cross section thickness remain consistent with those of the former model. Thus, it possesses 0.5 m cross section chord parallel to the leading edge, yielding 0.55169 m in the parallel chord to the wind tunnel wall due to the 25º sweep angle. The span in the perpendicular direction to the wind tunnel wall measures 1.3 m, with a total span due to the sweep of 1.434 m However, for the wind tunnel assembly on the aerodynamics balance and to create a small clearance to the wind tunnel wall contact with the internal cross-section roof, since the model has a free end, 3 cm of wing had to be removed from the upper wing extremity. This modification is depicted in Figure 4.4.

Figure 4.4: Gap between the swept wing model and the wind tunnel superior wall.

As previously mentioned, a hole measuring 17 mm in radius and 150 mm in depth has been drilled for the pressure field determination experiment, along with two additional holes for securing the metal discs that attach the endplate to the model. This method of attachment was chosen due to the increased likelihood of a metal-to-metal joint remaining secure compared to a metal-to-wood joint. In Figure 4.5 the wing base is depicted with the drilled holes, while Figure 4.6 shows it with the metal discs in place. The screws used for this purpose can be observed in Figure 4.7.

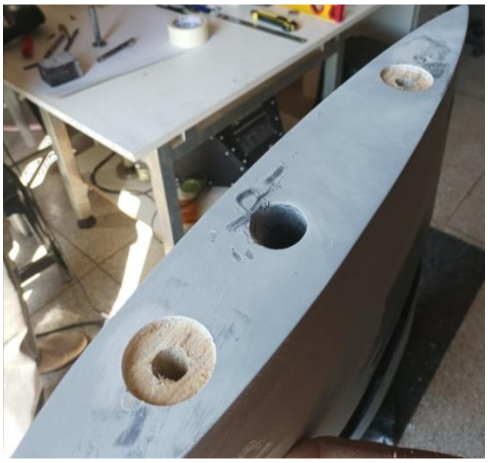

Figure 4.5: Swept wing model base.

Figure 4.6: Swept wing model basis with fixation discs attached.

Figure 4.7: Attachment screws used for the wing model attachment to the endplate.

Figure 4.8 shows the swept model assembled in the wind tunnel. A planning drawing with some measures of this wing, the ribs and the hatch can be found on ANNEX I.

Figure 4.8: Manufactured Swept Wing Model.

The choice of a 25-degree sweep angle was made to align with the typical sweep angles used in commercial aircraft swept wings and to ensure that the wing would fit properly within the wind tunnel test section. A significant design consideration arose during the wing design process to whether the wing chord should be aligned perpendicularly to the leading edge of the wing or to the airflow direction. After consulting aircraft design literature and relevant references, the conclusion was reached that the chord should be aligned with the leading edge. This decision was based on the understanding that aligning it with the airflow would render the impact of the sweep angle negligible. A more complete discussion on this topic is provided in APPENDIX III.

Thus, to be able to accomplish a meaningful comparison between both models, the pressure taps were positioned along the wing's chord with identical spacing as in the previous case. However, instead of placing the pressure taps close to the borders, to diminish border effects, they have been positioned in the wing midpoint. Also, to decrease the wing airflow contamination an endplate was designed to reset the boundary layer within the wind tunnel, thus preventing its influence on the wing. It has a diameter that is twice the chord of the wing. The CAD representation can be found on Figure 4.9.

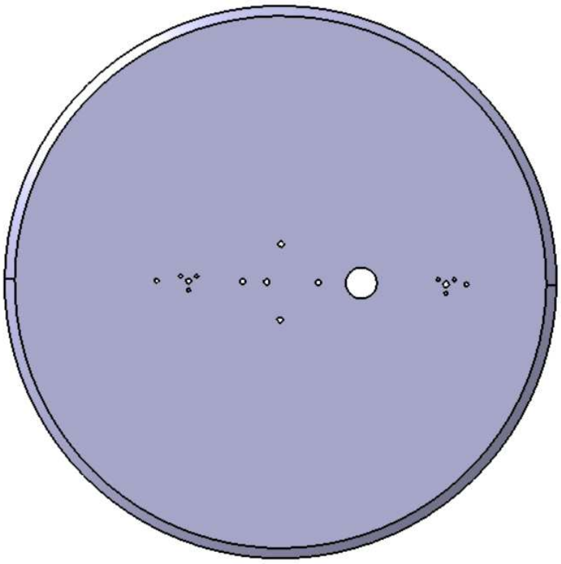

Figure 4.9: Endplate CAD Model.

The five smaller holes located in the middle serve the purpose of attaching the endplate to the aerodynamics balance, while the larger hole accommodates the passage of pressure taps into the wing model. The remaining holes are used to secure the wing model to the endplate. Figure 4.10 illustrates the assembly of the endplate and wing within the wind tunnel.

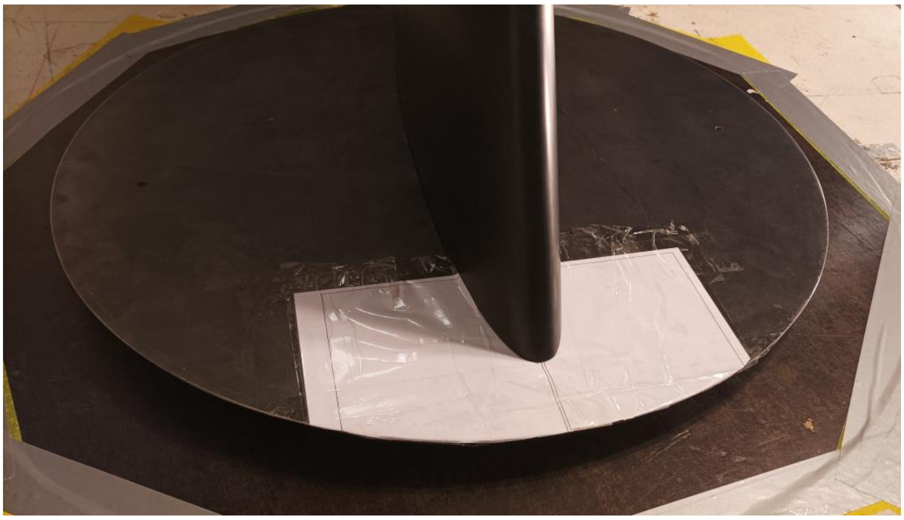

Figure 4.10: Endplate to swept wing model assemble.

4.3 Project Variables

As outlined in the introductory chapter, when considering laminar airflow approaching the wing leading edge, specific conditions may lead to the amplification of disturbances within the boundary layer upon interacting with the wing surface. In the case of straight wings, these initially amplified disturbances, if not mitigated, can evolve into Tollmien-Schilling waves. However, for swept wings, in addition to the appearance of Tollmien-Schilling waves in the parallel flow direction, crossflow instabilities manifest in the orthogonal direction Depending on the situation, the CFI or the previous CFV may cause the amplification of the T-S waves and speed up the transition process.

Then, to propose a comprehensive analysis of the phenomenon, it becomes necessary to establish the variables that influence the transition from laminar to turbulent within the boundary layer. Figure 4.11 variables that influence the transition from laminar to turbulent within the boundary layer.

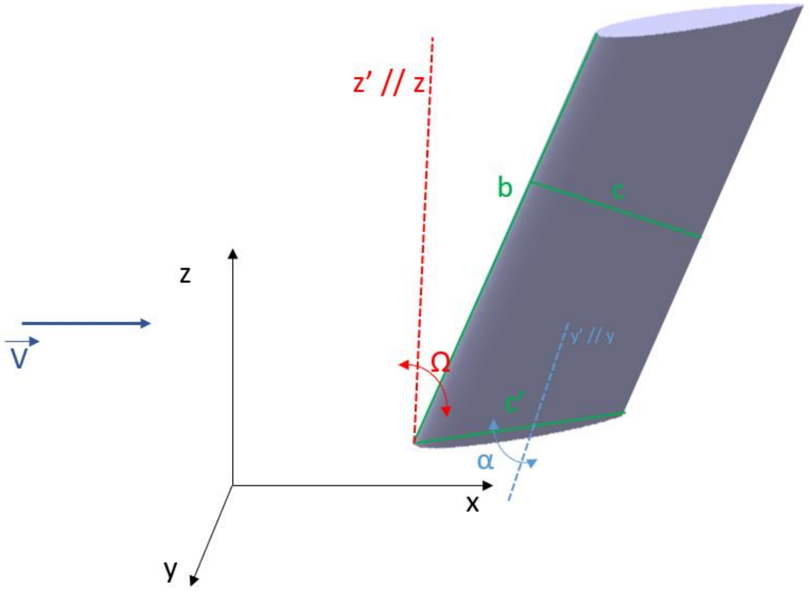

Figure 4.11: Project variables and axis system.

V = velocity; Ω = sweep angle; α = angle of attack; c = chord perpendicular to the leading edge; c' = chord; b = wingspan.

The primary parameter to consider is the Reynolds number, as it significantly impacts flow characteristics. Depending on this parameter, not only can the transition front position along the wing chord shift, but the aerodynamic forces and pressure field intensity may also vary. Moreover, when seeking to compare results between swept wing and straight wing cases, it is essential to ensure that the Reynolds numbers in both experiments are consistent. This alignment ensures that the only differing factor affecting the transition front position between the cases is the wing sweep angle, thereby isolating the crossflow instabilities issue from other variables.

Next, the angle of attack at which the wing is positioned must be taken into account. This is needed because the aircraft adjust its angle during different flight phases, and certain wings are attached to the fuselage at a non-zero angle of attack. Since the transition front position shifts in response to the angle of attack due to alterations in pressure distribution and the interaction of the airflow with the wing, it is essential to conduct experiments that encompass variations in this parameter. Therefore, to establish a meaningful drag polar for the intended experiments, it is necessary to define the range of angles of attack that will be tested.

The Mach number is another factor that must be taken into consideration, as it significantly influences flow characteristics. Typically, for low-speed wind tunnels (in which the experiments described herein are conducted), the Mach number does not reach the transonic or, certainly, the supersonic regime. Consequently, in this scenario, the experiments are conducted within the subsonic regime.

The next parameter to consider is the boundary layer itself, which is characterized by the wing chord, cross-sectional geometry, and pressure coefficient distribution. The interaction between the flow and the body is influenced not only by the variables but also by the wing geometry. Together, they define the pressure distribution, which, in turn, affects the aerodynamic forces of lift and drag. Additionally, the pressure coefficient allows us to identify regions of fluid acceleration and deceleration and to assess the potential for boundary layer separation. Capturing the velocity profile of the boundary layer along the wing chord would provide insights into fluctuations in the mean base flow and, consequently, the frequency of instabilities in the boundary layer that could impact the transition to turbulence. However, velocity measurements of the boundary layer were not conducted in this study due to equipment limitations.

Finally, the last variable to consider is the transition point or the position of the transition to turbulence itself. When examining this variable, it is not only essential to determine the transition point along the wing chord but also to analyze its cause. This is important because the ultimate objective of identifying the transition point is to develop flow control mechanisms. Having a clear understanding of the cause simplifies the process of proposing more effective control devices. Next, the wind tunnel facility, equipment used, and methods applied are presented.

4.4 Materials and Methods

To characterize the boundary layer on the swept wing model and identify the transition front to turbulence, three distinct experiments were conceived and carried out: aerodynamics characterization via the acquisition of the pressure field and the acquisition of the aerodynamics efforts of lift and drag, and the visualization of the transition front to turbulence of the boundary layer via infrared thermography. For the first experiment a pressure transducer and a Scanivalve of 64 channels has been used while for the aerodynamics forces acquisition an external three components aerodynamics balance has been used. For the visualization experiment an infrared camera has been utilized to visualize the process via infrared thermography. All the experiments have been conducted inside a closed wind tunnel facility and the experimental apparatus are next specified.

4.4.1 Wind Tunnel Facility

The wind tunnel testing was conducted within the LAE-1 (Laboratório de Aerodinâmica 1) facility at the Escola de Engenharia de São Carlos (EESC-USP). This wind tunnel is designed as a blow-down, low-speed closed-circuit system featuring a test section measuring 1.68 m x 1.29 m x 3.00 m in dimension. The airflow within the tunnel is generated by an eight-bladed rotor, which is driven by a 110 hp electric motor, thereby allowing for maximum airspeeds of approximately 40 m/s within the test section (CATALANO, 2014). This wind tunnel configuration incorporates two screens positioned at the contraction cone, contributing to the generation of turbulent levels lower than 0.26% (SANTANNA et al., 2014). Moreover, its operational capabilities extend up to approximately Mach 0.12, rendering compressible effects negligible. Figure 4.12 represents the wind tunnel schematic.

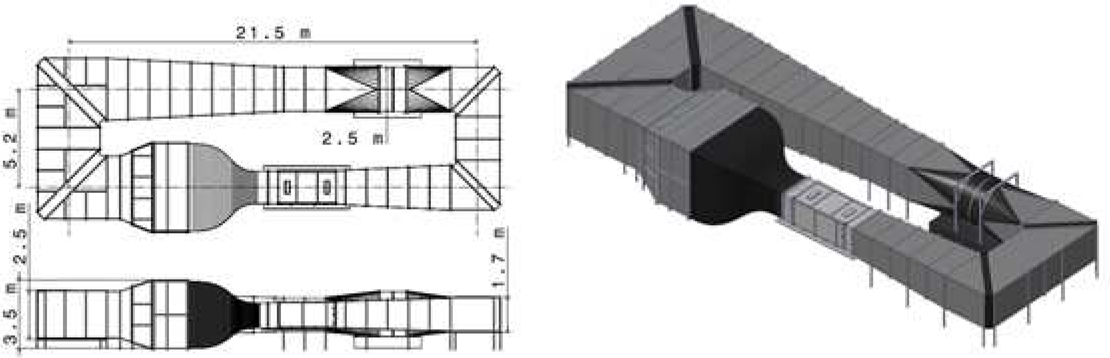

Figure 4.12: LAE-1 Wind Tunnel Schematics

4.4.2 Infrared Thermography Camera

The infrared camera captures the infrared spectrum of the light and filters it to allow only the passage of the infrared range. Then, based on the difference in intensity of the heat emission of each part of the body, it generates an image attributing to each pixel a value in a gray scale based on this intensity difference, translating the infrared spectrum captured into a gray scale image. If desired, artificial coloration may also be applied. Thus, the application of it to identify the transition front is grounded in the higher thermal energy exchange capacity of the turbulent flow if compared to the laminar one because it should be possible to differentiate the regimes due to a difference in the intensity of the gray scale image registered in each portion of the boundary layer between both regimes. However, for such intensity difference to be noticed, the hotter or colder the body is in relation to the mean it is immersed and the less reflective it is, the higher will be the contrast between the body and the mean and higher will be the contrast difference between the laminar and the turbulent portion. Thus, higher should be the resolution of the image registering the transition event (CRAWFORD et al., 2013).

If t the wing exhibits a higher temperature compared to the surrounding airflow, the increased thermal energy exchange capability of the turbulent regime will result in a faster cooling of the turbulent flow region compared to the laminar region. Consequently, in the infrared image, the turbulent portion will appear with a less intense grayscale color. Conversely, if the wing is cooler than the surrounding airflow, the turbulent region will exchange thermal energy more rapidly, causing it to become hotter than the laminar portion. This will be reflected in the infrared image, which will exhibit a higher grayscale intensity. Considering this information, it is essential to exercise caution when heating or cooling the test object. This is necessary to prevent not only the blurring or introduction of noise in the infrared image due to low contrast between the airflow and the object but also to enhance the visibility of the transition front. A higher contrast between the laminar and turbulent flow portions will lead to better detection of the transition front (KLEINUBING et al., 2013).

For this experiment, the choice was made to heat the model rather than cool it due to the practical considerations involved. Cooling the model would necessitate disassembling the wing from the wind tunnel each time cooling was required. This approach would not only introduce logistical challenges but also increase costs and raise concerns about the safety of immersing the model in a freezing fluid. As a result, cooling the model was deemed impractical for this study. To heat the swept wing model effectively, six halogen lights of 60 watts were installed in two corner fillets, with three lights in each fillet. Additionally, two corner fillets without lights were also installed to ensure symmetry within the wind tunnel test section. Figure 4.13 shows the corner fillets with the lights installed.

Figure 4.13: Allogeneic lights and corner vanes installation into the wind tunnel test section.

Therefore, in the grayscale image obtained, the contrast in intensity between the laminar and turbulent flow regimes must be significant enough to create a discernible line extending across the wingspan of the wing. This line demarcates the transition points where the boundary layer shifts from a laminar to a turbulent state. Consequently, locations with higher heat exchange emissivity rates will yield lower pixel values in the image. If both the airflow and the wing have identical temperatures and emissivity, distinguishing between the two in an infrared image would become exceedingly challenging. To facilitate precise image acquisition, the camera is connected to a computer running specialized camera software responsible for controlling image capture. To enhance image quality, specific points within the area of interest are marked to facilitate camera calibration. These calibration points have been highlighted using aluminum paint, as depicted in Figure 4.14.

Figure 4.14: Calibration points for the infrared camera.

Regarding the equipment setup, the camera was positioned at the midpoint of the wing wingspan to visualize the boundary layer transition front, specifically at half the height of the test section. This placement minimizes the impact of potential three-dimensional effects that could influence other sections of the wing. Also, to avoid potential interference from the reflectivity or refraction effects caused by the acrylic test section wall, a hole with a diameter closely matching that of the camera lens was drilled into the test section wall. This modification ensures optimal visualization and allows the camera to be positioned at the midpoint of the wind tunnel span along the y-axis. The camera configuration is illustrated in Figure 4.15. Besides the image results, the camera software delivers a table with each captured pixel temperature. Then, After the images acquisition, they are computationally processed using a Python code detailed in ANNEX II. This code not only delineates the transition front by employing a border detection algorithm but also calculates the mean position of the transition front in relation to the wing chord.

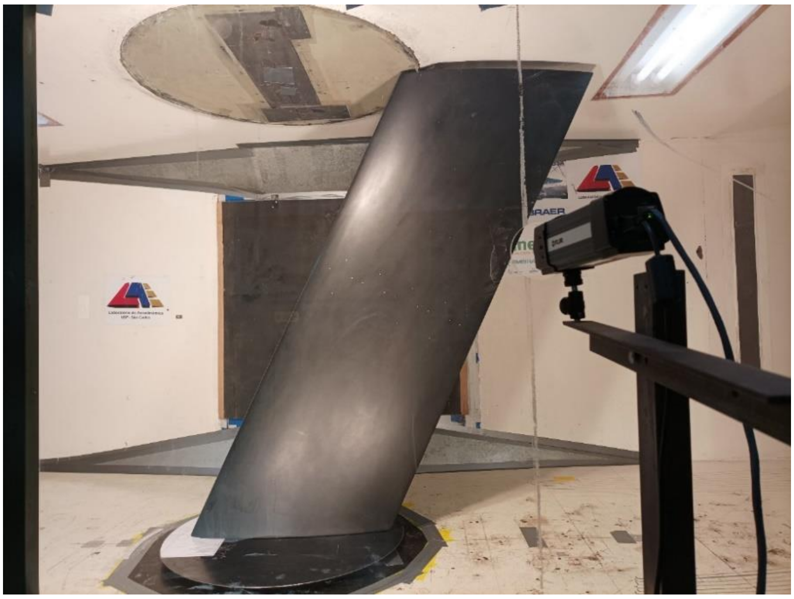

Figure 4.15: Experimental assemble with infrared camera positioning.

The camera used in this experiment is the model FLIR A300 which characteristics are presented in Table 4.1. Its Datasheet is also presented on ANNEX III.

Table 4.1: Infrared Camera Characteristics

Field of View (FOV)	25º x 18.8º
Image Frequency	30 Hz
Image Resolution	320 x 240 px
Thermal Sensivity	0.05 ºC
Zoom	1-8 Digital
Communication Rate	3 Hz
Communication Port	IP-Ethernet
Camera Age	2010
Output Available	MPEG

4.4.3 Pressure Transducer

For the pressure field determination, 64 holes of 2 mm in diameter have been drilled at the middle of the wing alongside its chord perpendicularly to the leading edge. The coordinates for the pressure taps can be found at APPENDIX VII. Then, metal tubes of the same external diameter have been glued into them, internally to the wing, to attach the pressure taps. Then, the pressure taps are connected to a Scanivalve ZOC33 model pressure scanner that receives and converts the flow signal into an electrical one that is read by the pressure transducer software. The Scanivalve is placed inside the swept wing model connecting the pressure tubes from the module to the wing. The pressure tubes reach the inside of the wing through a hole drilled through the wing’s wooden base. Also, it is important to be sure that one of the 64 channels is registering the wind tunnel dynamic pressure at a free airflow condition and that another channel registers the wind tunnel static pressure to be used as a reference value during the data treatment. Finally, the experiment is run for each Reynolds number varying the angle of attack. Then the wind tunnel is reset and the measurements for the next Reynolds number begins. Figure 4.16 represents the Scanivalve used while its Datasheet is presented in ANNEX III.

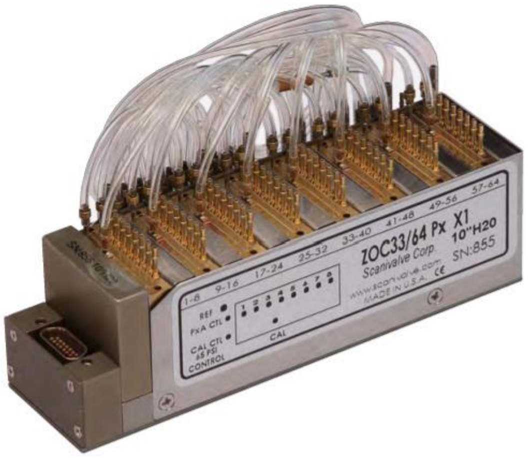

Figure 4.16: Scanivalve ZOC33/64 Px X1.

4.4.4 Aerodynamics Balance and Aerodynamics Efforts Determination

The aerodynamics efforts of lift and drag have been determined via an external three components aerodynamics balance manufactured and designed by the Universidade de São Paulo (USP) laboratories. To determinate the aerodynamic efforts, the endplate is attached to the balance axe that is free to move and rotate so that the efforts can be registered, allowing it to vary the model's angle of attack. Since the wing is attached to the balance through the axe, when the wind blows, the wing is displaced. The displacement of the axe is then sensed by the balance so that in the parallel component to the balance the cargo cells translate the movement into the drag force and the displacement in the orthogonal direction is translated into the lift force. All this information is captured by the balance modulus and translated into the effort's information at the balance software in a computer. All the validation process (calibration and hysteresis verification) has already been done at Eguea (2022). Figure 4.17 represents the aerodynamics balance, with the next topic presenting the experiment's test matrix.

Figure 4.17: Three Components Aerodynamics Balance.

4.5 Experiments Description

The previous section concerned the experimental assembly, equipment's description, and their functionality. This section, though, shall present the experiment's goals, the measure objectiveness, and their test matrix.

4.5.1 Pressure Field Determination

The pressure field determination aims to establish the pressure coefficient distribution across the wing model at designated measurement points. For this study case, interest lies in examining the distribution along the wing chord since the transition front is moves along the chord. To mitigate three-dimensional effects, the center section of the wing, specifically a 500 mm section parallel to the wing leading edge, has been selected for measurement, which will allow a direct comparison to straight wing model. Thus, this experiment serves a dual purpose. Firstly, it characterizes the interaction between the airflow and the wing, shedding light on potential boundary layer separation. Secondly, it generates valuable data for future works involving numerical-computational methods. Many emerging methods rely on semi-empirical approaches, which necessitate access to pressure field data. Hence, this experiment not only contributes to understanding the airflow behavior over the wing but also supports the development of numerical-computational approaches in the quest to identify the boundary layer transition front.

In the experiment, a specific Reynolds number is selected initially set at an angle of attack 0 º. After ensuring the airflow has achieved stable conditions, the pressure transducer is triggered by a computer signal to commence data collection. For each channel, a determined number of signals is captured during a certain amount of time, registering the total number of samples. a Matlab script computes the mean value for each channel, recorded in a DAT file in terms of pressure in Pascal. These data are then transformed into pressure coefficient values. The angle of attack is then incrementally adjusted, and the data acquisition process is repeated. This sequence is reiterated for all the desired angles of attack at the same Reynolds number. Upon completing the experiment for all the designated angles of attack at a given Reynolds number, the wind tunnel is deactivated, and the wing angle of attack is reset to zero. The procedure is then repeated for another Reynolds number until the final Reynolds number is reached. Table 4.2 outlines the test matrix for pressure field determination, encompassing five Reynolds numbers ranging from 450000 to 915000 and varying angles of attack from 0 to five degrees. It is worth noting that the mean temperature throughout the experiments remained at 17.8 ºC.

Table 4.2: Pressure Field Determination Test Matrix

Reynolds Number x10³	**Angle of Attack [°]**					
	0	**1**	**2**	**3**	**4**	**5**
450	✓	✓	✓	✓	✓	✓
650	✓	✓	✓	✓	✓	✓
720	✓	✓	✓	✓	✓	✓
765	✓	✓	✓	✓	✓	✓
915	✓	✓	✓	✓	✓	✓

4.5.2 Lift and Drag Acquisition

The lift and drag, when expressed as lift and drag coefficients, provide essential information concerning the interaction between the wing and the airflow, particularly in the context of aerodynamic forces. The efficiency of an aircraft is heavily contingent on the lift and the drag, as they significantly influence its overall performance. Given that the present wing design does not adhere to modern wing configurations, a high lift-to-drag ratio is not anticipated. Nevertheless, it is crucial to establish the CL x alpha and Cd x CL curves to elucidate the wing behavior. The CL x alpha curve serves to determine the maximum attainable angle of attack for a specific combination of Reynolds number and environmental conditions. Simultaneously, the drag polar characterizes the wing aerodynamic efficiency, indicating the optimal CL value at which the aircraft can operate with minimal fuel consumption. In the context of boundary layer transition to turbulence, under conditions where the Reynolds number or angle of attack remains constant, it is anticipated that higher Cd values will result in the transition occurring closer to the wing's leading edge in comparison to instances with lower Cd values.

Similar to the pressure field determination, a specific Reynolds number is chosen, and the angle of attack is initially set to zero. Subsequently, the wind tunnel is activated, and once the airflow has achieved a state of stability, the data acquisition process commences. Following completion of the measurements for all desired angles of attack, the wind tunnel is deactivated, and the procedure is then repeated for the subsequent Reynolds number. Initially, the objective was to construct a comprehensive CL x Alpha curve. However, as the Reynolds number increased, a smaller range of angles of attack was designated due to the concurrent growth in lift force, which is contingent upon both the angle of attack and the Reynolds number. Consequently, to maintain safety precautions, even though the model was securely affixed, limits for the angle of attack were imposed for higher Reynolds numbers to preclude any potential incidents.

Furthermore, in the determination of drag force, it is essential to note that the endplate, designed to mitigate the three-dimensional effects that impact the wing by resetting the wind tunnel boundary layer, contributes to the overall drag recorded by the balance acquisition system. This is because the endplate is affixed to the wing and moves in concert with it, leading to a displacement in the aerodynamic balance. Regarding the lift force, since the endplate is a symmetrical body in both the orthogonal and parallel directions to the balance axis, its influence on the registered lift is negligible. Consequently, after conducting experiments involving the assembly of the endplate with the wing, a comprehensive test involving the same range of Reynolds numbers was performed solely for the endplate. This allowed the drag contribution of the endplate to be isolated from the previous experiment, resulting in a more accurate determination of the actual wing drag. To calculate the final lift and drag coefficients, it is necessary to apply a wind tunnel correction law to the raw aerodynamic force data. This correction accounts for the blockage ratio of the wing relative to the wind tunnel cross-section, which causes flow acceleration and alters the measured values of angle of attack, lift, and drag. Following these steps, the CL x α curve and the drag polar can be computed and presented. Table 4.3 presents the lift and drag acquisition test matrix.

Table 4.3: Aerodynamics Efforts Acquisition Test Matrix

Reynolds Number x10³	Mean Temperature [ºC]	Angle of Attack [°]														
		0	1	2	3	4	5	6	7	8	9	10	11	12	13	14
450	21.9	✓	✓	✓	✓	✓	✓	✓	✓	✓	✓	✓	✓	✓	✓	✓
650	22.4	✓	✓	✓	✓	✓	✓	✓	✓	✓	✓	✓	✓	✓	✓	✓
720	22.6	✓	✓	✓	✓	✓	✓	✓	✓	X	X	X	X	X	X	X
765	18.4	✓	✓	✓	✓	✓	X	X	X	X	X	X	X	X	X	X
915	18.8	✓	✓	✓	✓	✓	X	X	X	X	X	X	X	X	X	X

4.5.3 Transition Front Detection Via Infrared Thermography

The primary objective of this third experiment is to accurately locate the transition front of the boundary layer, marking the shift from laminar to turbulent flow conditions, in terms of the relative airfoil chord distance. As detailed in earlier sections, the success of this test hinges on ensuring that the tested swept wing model exhibits a temperature difference from the mean airflow. This temperature difference is crucial for achieving higher contrast in the resulting infrared images, distinguishing between the model and the surrounding air, as well as between the laminar and turbulent regimes. To achieve this temperature difference, the halogen lights are turned on with the wind tunnel switched off for approximately half an hour or until the model reaches an adequate temperature. This allows for a noticeable contrast between the model and the air in the test section where it is placed. Subsequently, with the wing set to a zero-degree angle of attack, the wind tunnel is activated. Once the desired velocity is attained, and the airflow reaches a stable equilibrium, the camera is activated to initiate image capture. After obtaining enough images, the camera software converts them into grayscale. The model is then adjusted to different angles of attack, and the image capture process is repeated. This process is carried out for all specified angles of attack for the chosen Reynolds number. After completing it, the wind tunnel is turned off, and the procedure is repeated for each of one of the Reynolds numbers. Like the previous experiment, for infrared visualization, the maximum angle of attack decreases with increasing Reynolds number due to safety precautions. Upon concluding all experiments, the raw images undergo processing using a Python image processing code (presented in ANNEX II).

This code is responsible for detecting the transition front by overlaying it on the grayscale image and providing the relative airfoil chord distance of the transition front as a mean value derived from all the transition points. The specific points tested are documented in Table 4.4.

Table 4.4: Infrared Visualization Test Matrix

Reynolds Number x10³	**Mean Temperature [ºC]**	**Angle of Attack [°]**														
		0	**1**	**2**	**3**	**4**	**5**	**6**	**7**	**8**	**9**	**10**	**11**	**12**	**13**	**14**
450	**15**	✓	✓	✓	✓	✓	✓	✓	✓	✓	✓	✓	✓	✓	✓	✓
650	**20**	✓	✓	✓	✓	✓	✓	✓	✓	✓	✓	✓	✓	✓	✓	✓
720	**23**	✓	✓	✓	✓	✓	✓	✓	✓	✓	X	X	X	X	X	X
765	**25**	✓	✓	✓	✓	✓	✓	X	X	X	X	X	X	X	X	X
915	**30**	✓	✓	✓	✓	✓	✓	X	X	X	X	X	X	X	X	X

Following the characterization of the model design, manufacturing choices, experimental setup, and procedures, the subsequent chapter documents the results obtained from the experiments and provides comprehensive discussions.

CHAPTER V

5. RESULTS AND DISCUSSIONS

The ensuing sections are dedicated to the exposition of the results obtained from the experiments detailed in the previous section, followed by their subsequent analysis. This examination is focused on investigating the effects of both Reynolds number and angle of attack on the transition of the boundary layer to a turbulent state in the swept wing model. Furthermore, in the pursuit of comprehending the influence of the wing sweep angle, particularly concerning the transition front behavior, it is pertinent to present and compare the results achieved with those derived from EGUEA, J.P., 2022.

5.1 Pressure Field Results

Next figures contain the pressure coefficient distribution curves for each Reynolds number and angle of attack measured. The tables with all the raw pressure data as much as their conversion into CP can be found in APPENDIX IV.

5.1.1 Pressure Field Distribution – Re = 450000.

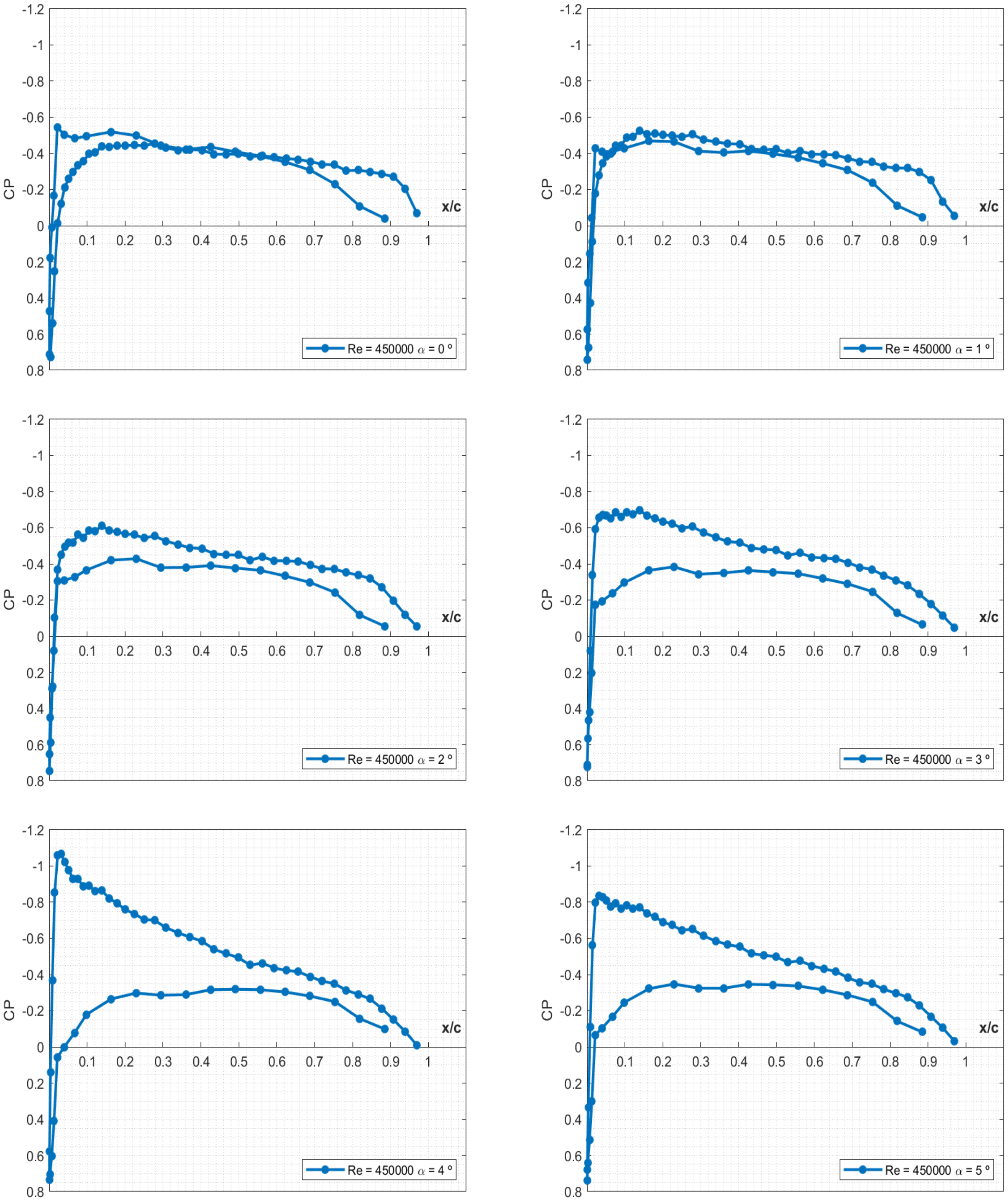

Figure 5.1: Swept Wing Pressure Field for Re = 450000 and $\mathbf{0}\,° \leq \boldsymbol{\alpha} \leq \mathbf{5}\,°$

5.1.2 Pressure Field Distribution – Re = 650000

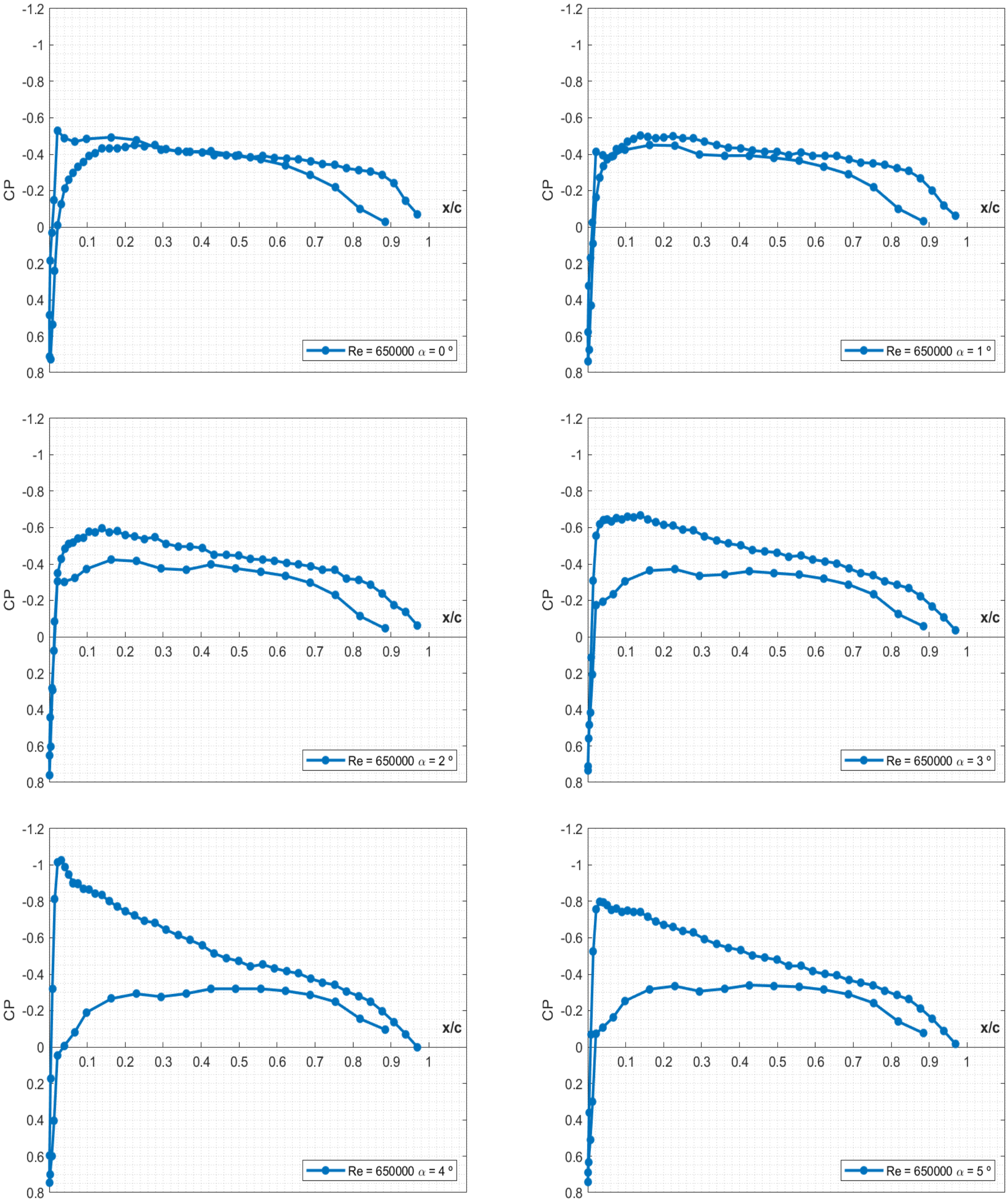

Figure 5.2: Swept Wing Pressure Field for Re = 650000 $\mathbf{0}° \leq \boldsymbol{\alpha} \leq \mathbf{5}°$

5.1.3 Pressure Field Distribution – Re = 720000

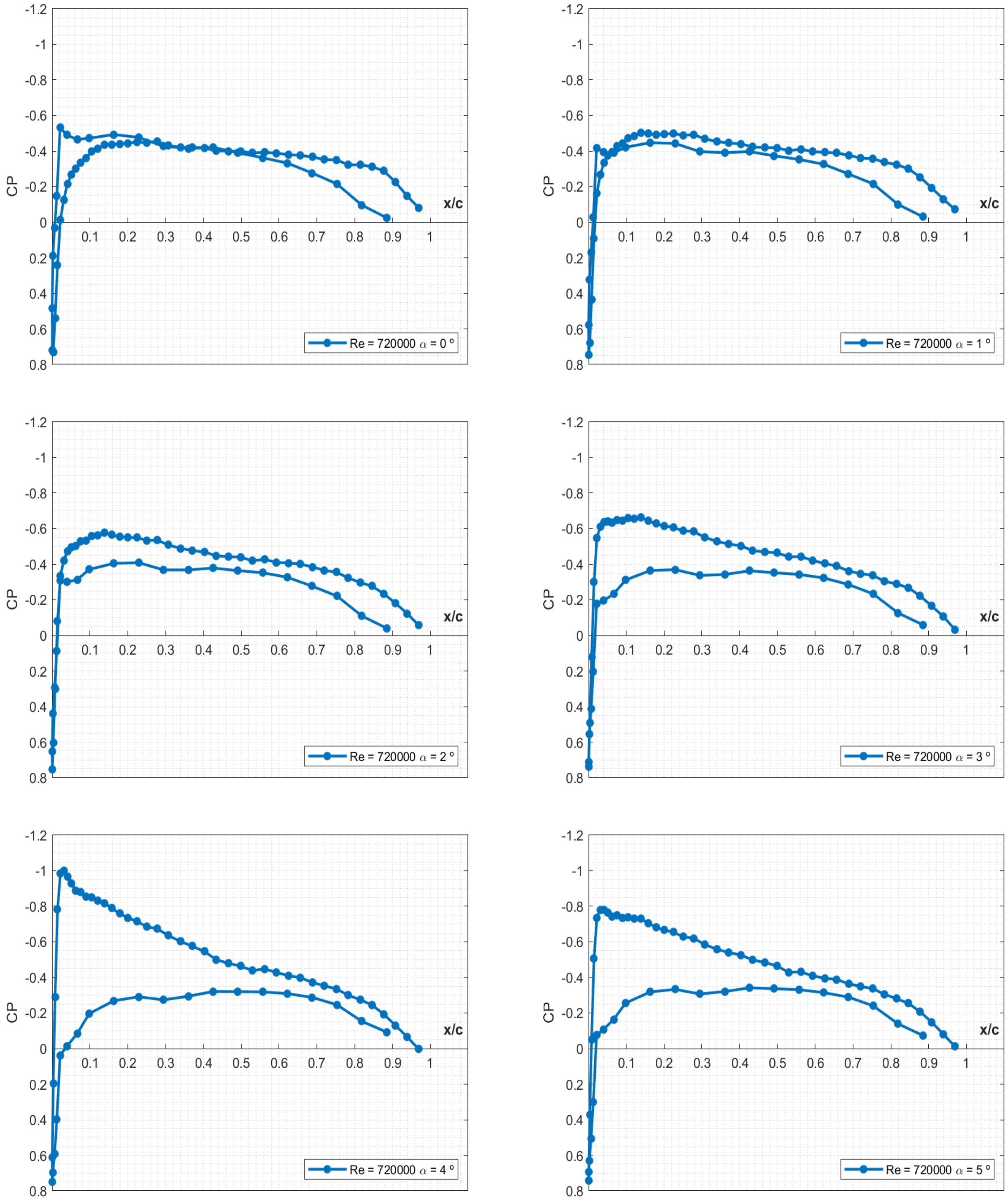

Figure 5.3: Swept Wing Pressure Field for Re = 720000 $\mathbf{0}^{\circ} \leq \boldsymbol{\alpha} \leq \mathbf{5}^{\circ}$

5.1.4 Pressure Field Distribution – Re = 765000

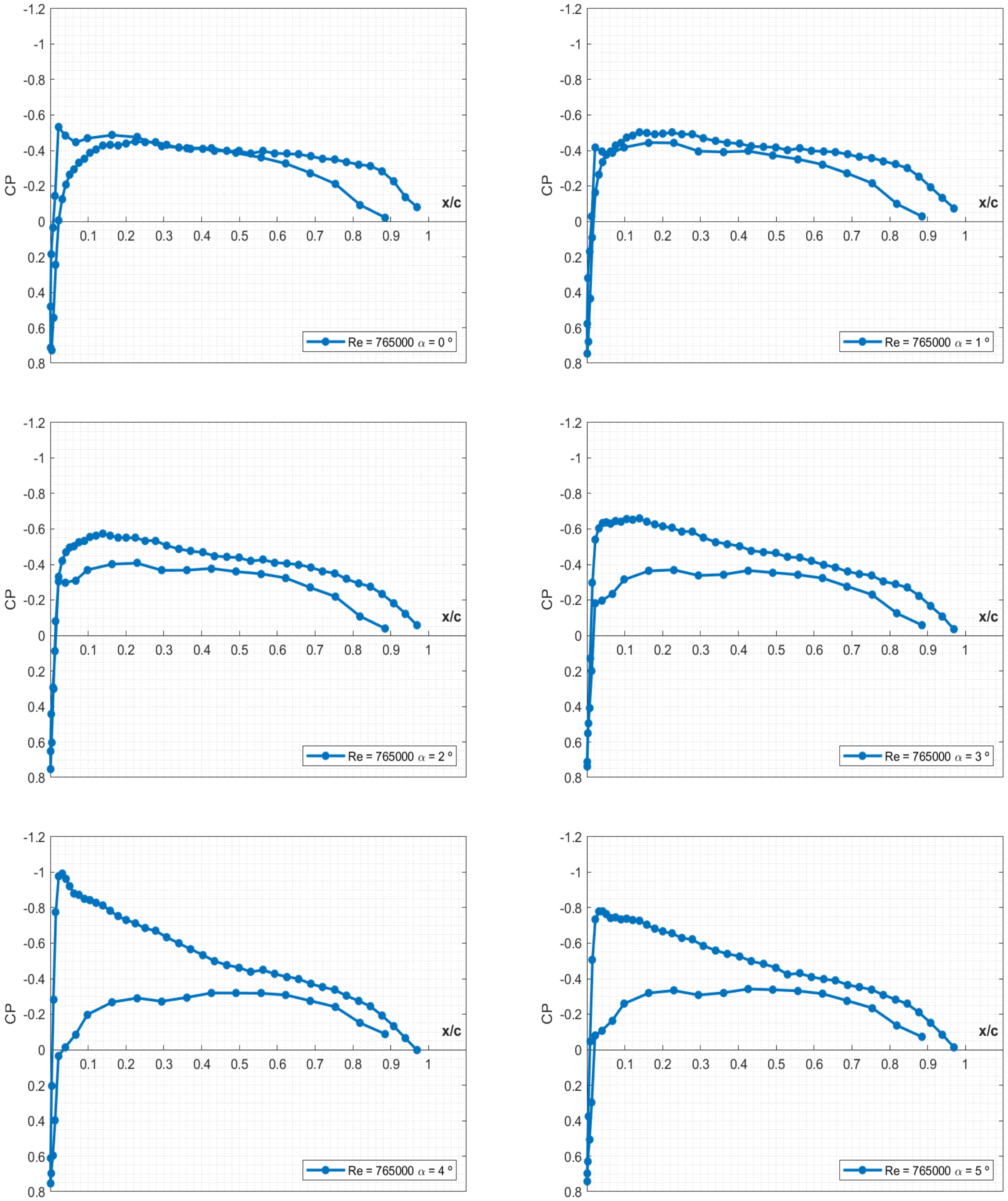

Figure 5.4: Swept Wing Pressure Field for Re = 765000 $\mathbf{0}\,° \le \boldsymbol{\alpha} \le \mathbf{5}\,°$

5.1.5 Pressure Field Distribution – Re = 915000

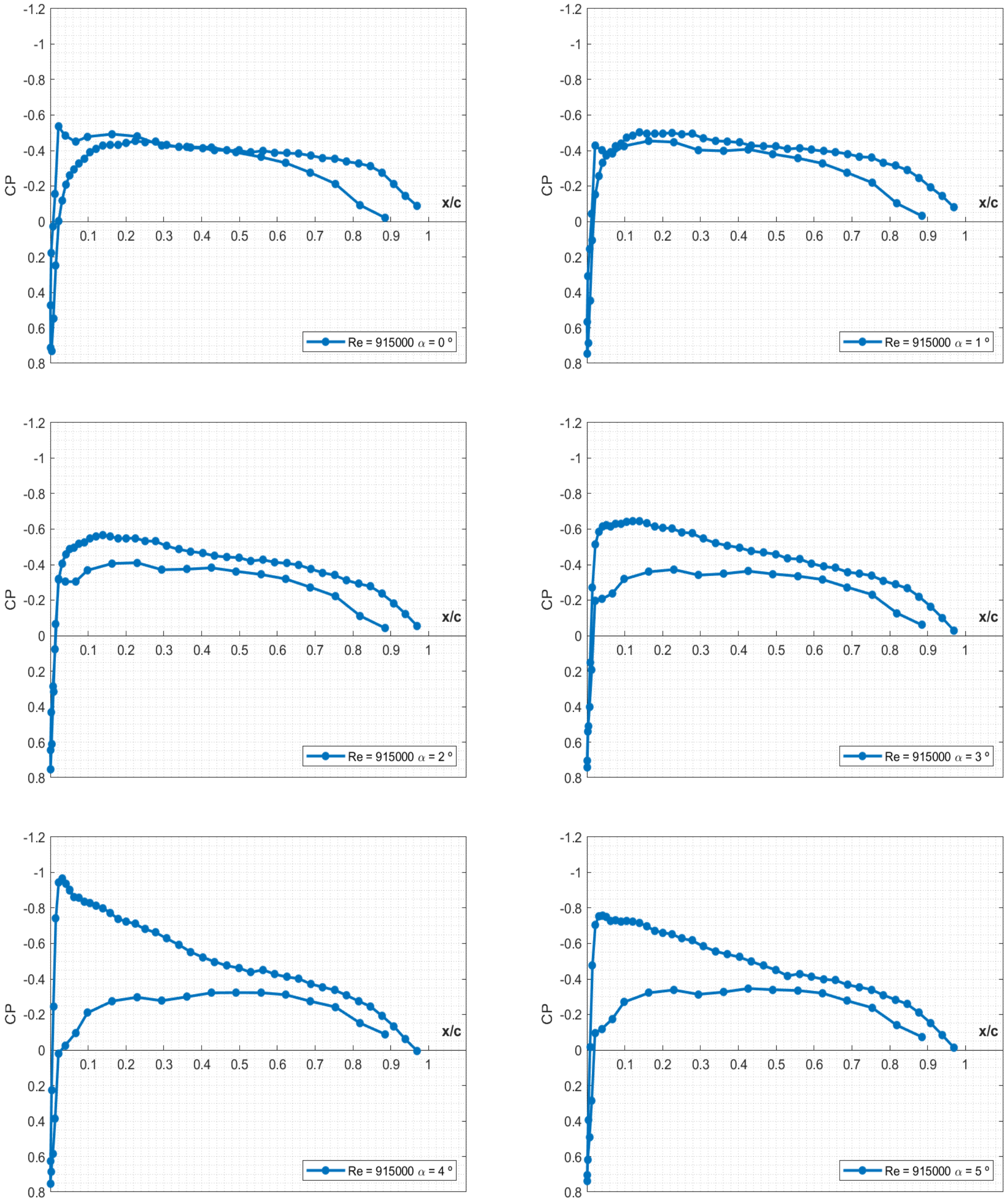

Figure 5.5: Swept Wing Pressure Field for Re = 915000 $0° \leq \alpha \leq 5°$

5.2 Lift and Drag Measurements

Before presenting the $CL\ x\ \alpha$ and drag polar curves, it is necessary to reiterate that the drag contribution resulting from the presence of the endplate must be subtracted from the drag value obtained through the aerodynamics balance. Also, it is essential to apply a wind tunnel correction, which is caused by the blockage ratio introduced by the presence of test bodies within the wind tunnel. This correction is necessary because the test body, owing to its proximity to the tunnel walls, alters the airflow characteristics upstream and downstream of the body by inducing airflow contraction. In essence, as the system can be regarded as mass-conservative and the air density remains relatively constant during the measurement, any constriction of the airflow area results in increased air velocity. This, in turn, leads to a change in the perceived angle of attack and the aerodynamic forces recorded by the equipment, particularly in the case of a wing model. Therefore, the results presented herein incorporate corrections based on a correction model (BARLOW, RAE, POPE, 1999). It is also worth noting that, for the sake of readability, tables are not displayed in the main text. However, for a more comprehensive understanding of the results or for reference, the results table can be found in APPENDIX V. Next topics include the endplate correction curve and the $CL\ x\ \alpha$ and drag polar final curves.

5.2.1 End Plate Lift and Drag

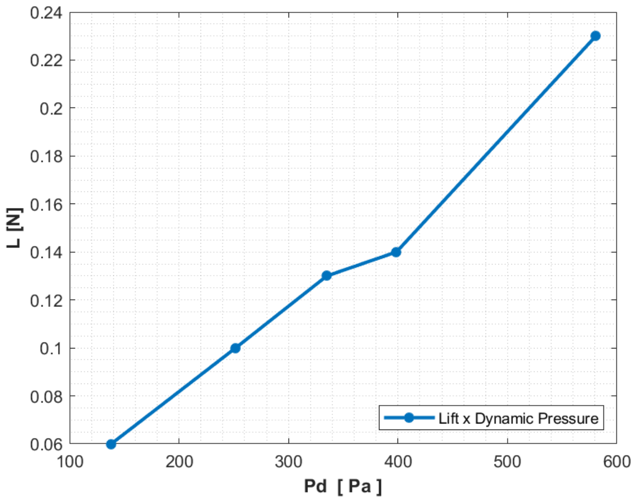

Figure 5.6: Endplate Lift x Dynamic Pressure

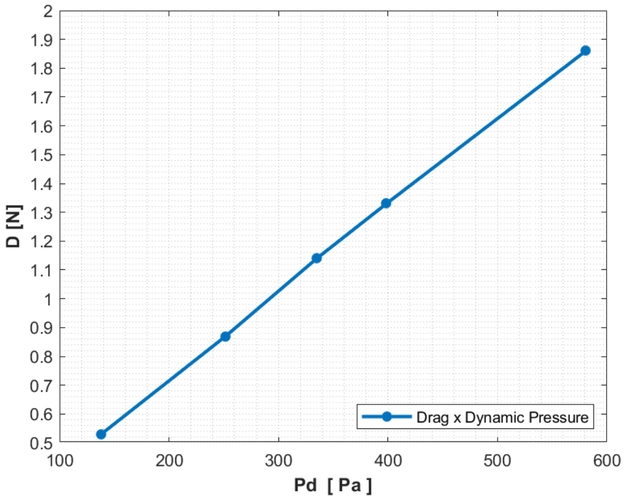

Figure 5.7: Endplate Drag x Dynamic Pressure

Some comments are already pertinent at this stage. As seen on Figure 5.6 the endplate lift contribution is negligible, although the recorded values are not precisely zero. This phenomenon is primarily due to system oscillations that are detectable by the aerodynamic load cells, resulting in the conversion of electrical potential differences into lift data. Additionally, since there is no downward force acting on the endplate and it is practically impossible to achieve a perfect alignment within the wind tunnel for all three axes, the airflow presence can induce deflections in any direction. Consequently, this perturbation is also transferred to the coupled balance axis, potentially accounting for the increase in recorded lift values with higher dynamic pressure levels. Concerning drag, the situation differs since the value registered is now considerable as depicted in Figure 5.7 and must be deducted from the combined wing and endplate system to isolate the drag of the wing.

5.2.2 $CL\ x\ \alpha$ Results

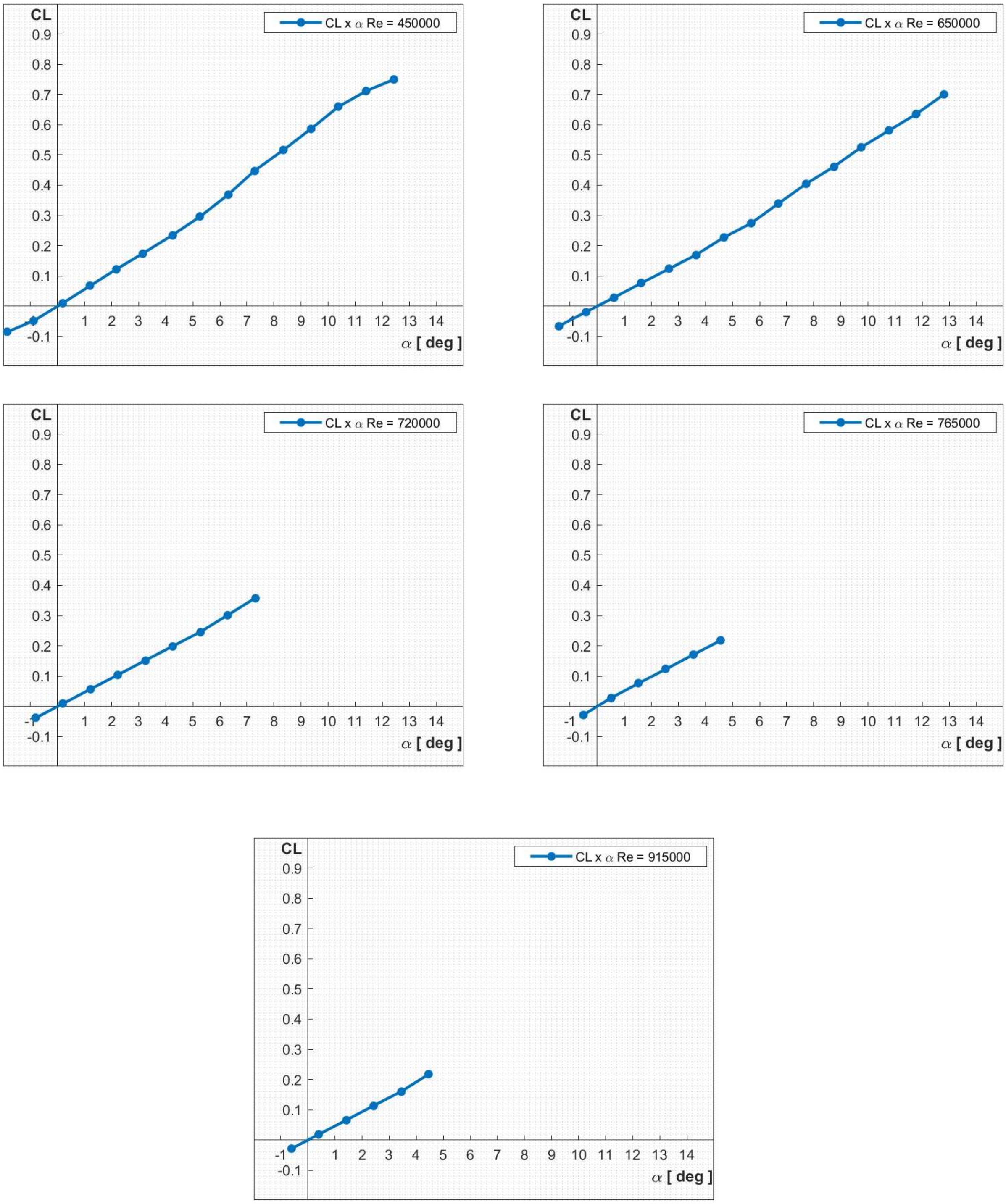

Figure 5.8: Swept Wing $CL\ x\ \alpha$ for each Reynolds Number

5.2.3 Drag Polar Results

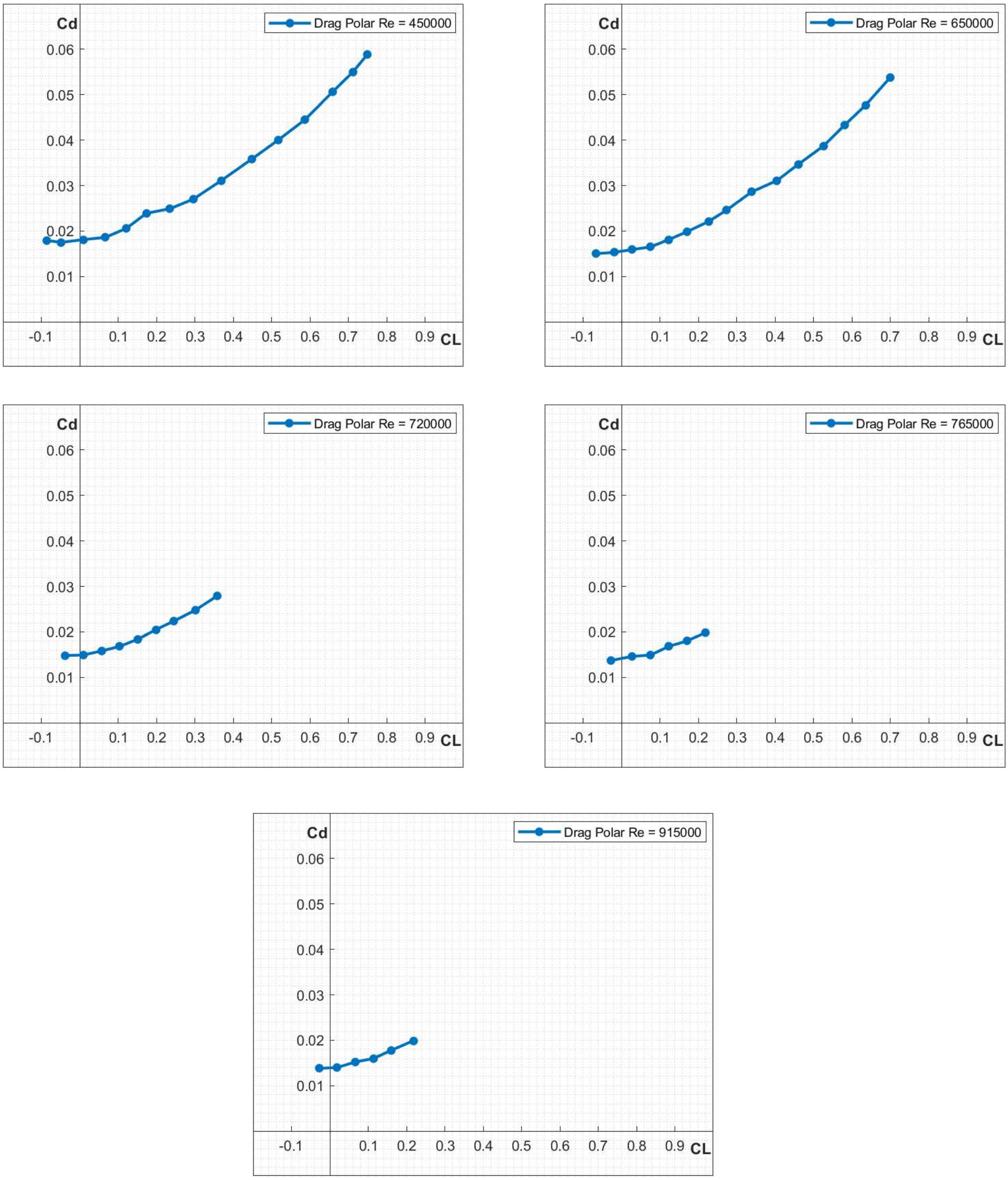

Figure 5.9: Swept Wing Drag Polar for each Reynolds Number

5.3 Boundary Layer Transition Front Detection

Next topics contain the infrared thermography results for the boundary layer transition to turbulence front detection. Not only the swept model results are herein presented, but later they are compared to straight model results so that the influence of the sweeping angle can be analyzed. The figures shown had already been processed by the border detection code presented in ANNEX II, so that the transition front can be more easily spotted. Nevertheless, the raw images can be found at APPENDIX VIII, if needed for complementary analyzes. Just as an example, Figure 5.10 shows a raw image contrasted to a computationally tread on. For all the images presented, the leading edge of the models (straight and swept), is in the left corner of the image and in the same way, the air flows from the left to the right.

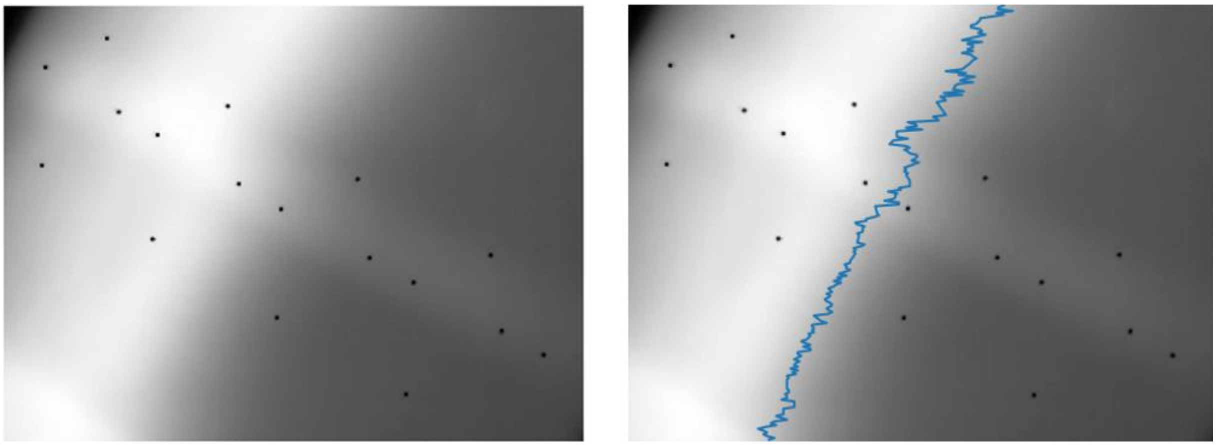

Figure 5.10: Image comparison for raw and tread images for the swept wing boundary layer transition detection at 4 ° of angle of attack and Re = 450000. Left: Raw image. Right: Treated image.

Next subtopics present the evolution of the transition front for each Reynolds Number tested and for the variation of the angle of attack. After, the medium value for the transition front is translated into a point and is plotted in a graphic of the transition to turbulent position in relation to the chord length to the angle of attack for each Reynolds number.

5.3.1 Swept Wing Infrared Images - Re = 450000

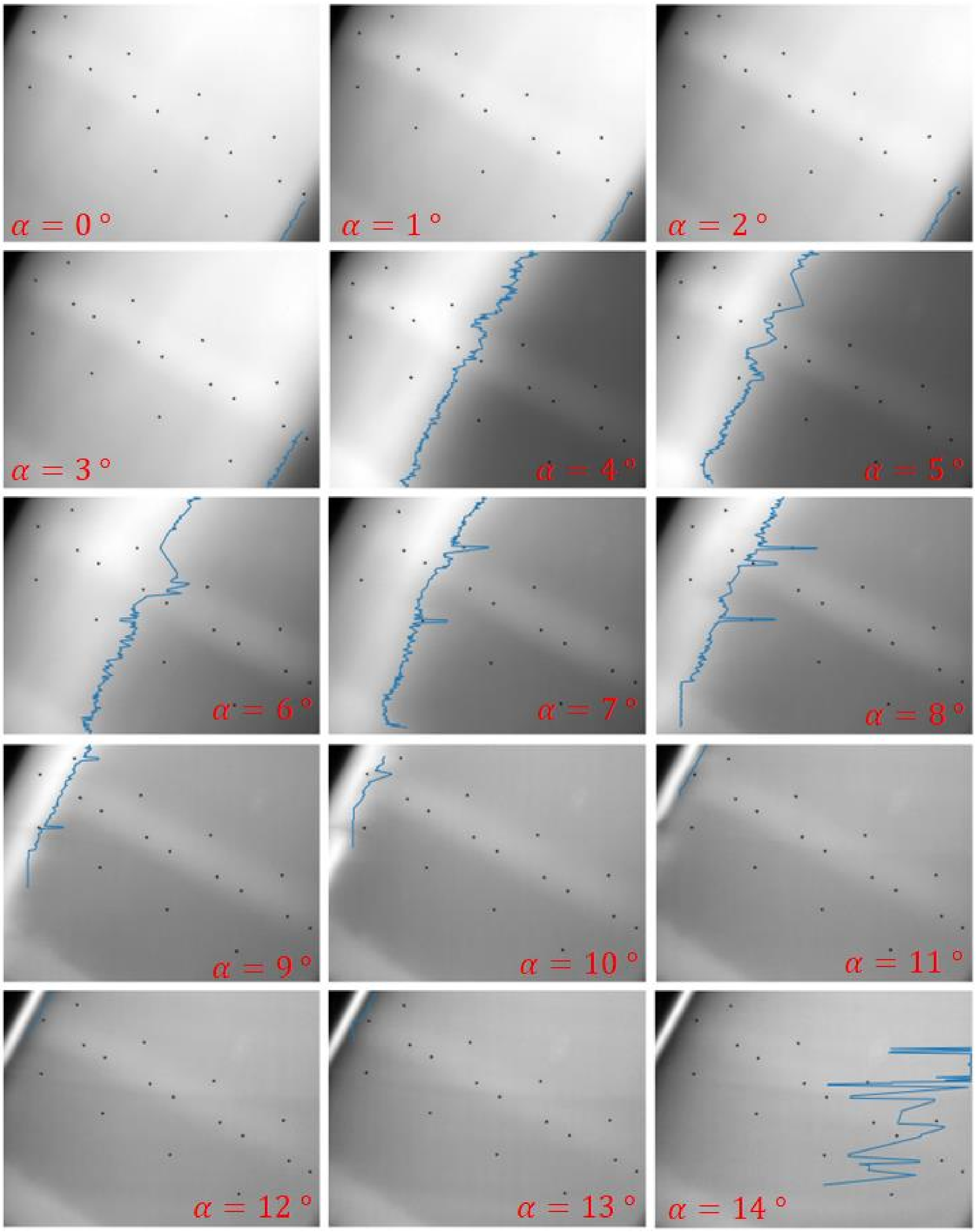

Figure 5.11: Infrared Results for Transition Line Detection at Re = 450000.

5.3.2 Swept Wing Infrared Images - Re = 650000

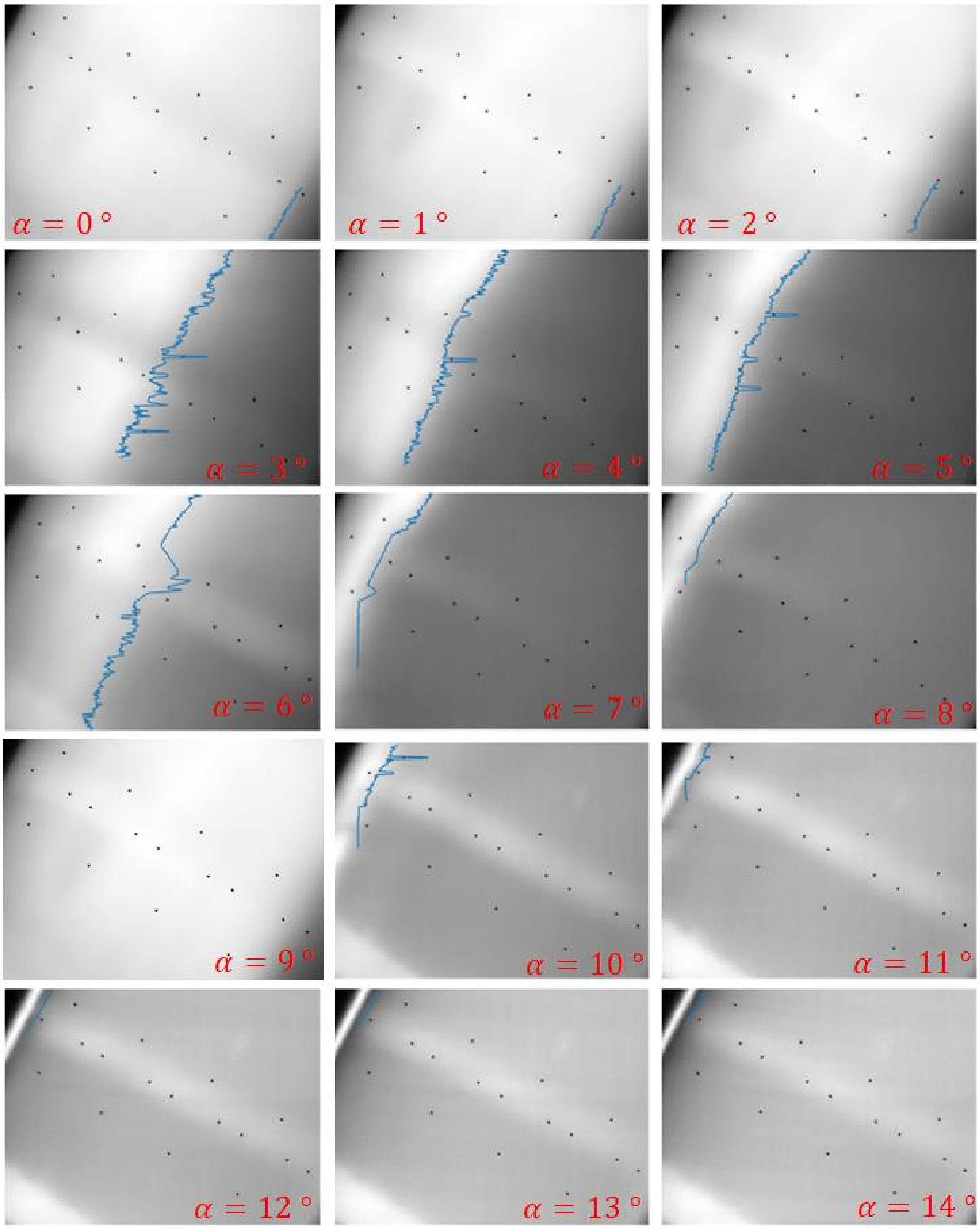

Figure 5.12: Infrared Results for Transition Line Detection at Re = 650000.

5.3.3 Swept Wing Infrared Images - Re = 720000

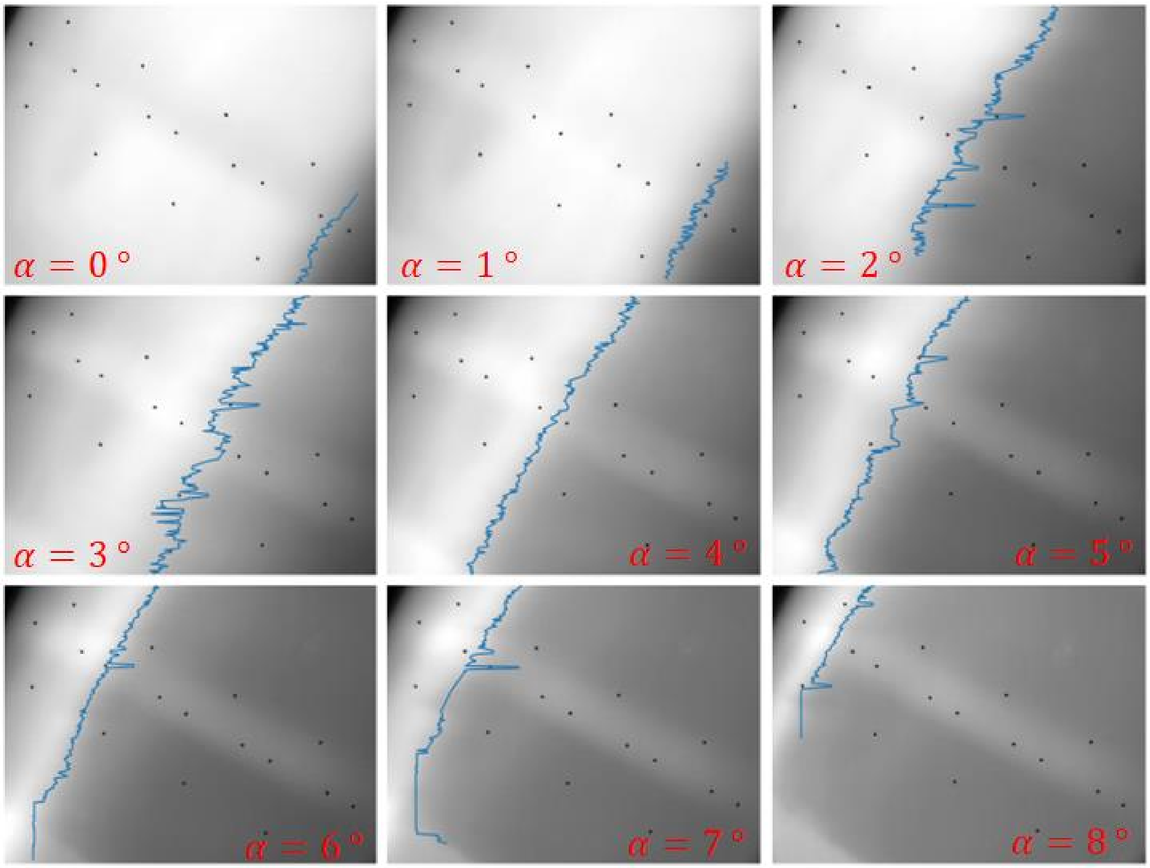

Figure 5.13: Infrared Results for Transition Line Detection at Re = 720000.

5.3.4 Swept Wing Infrared Images - Re = 765000

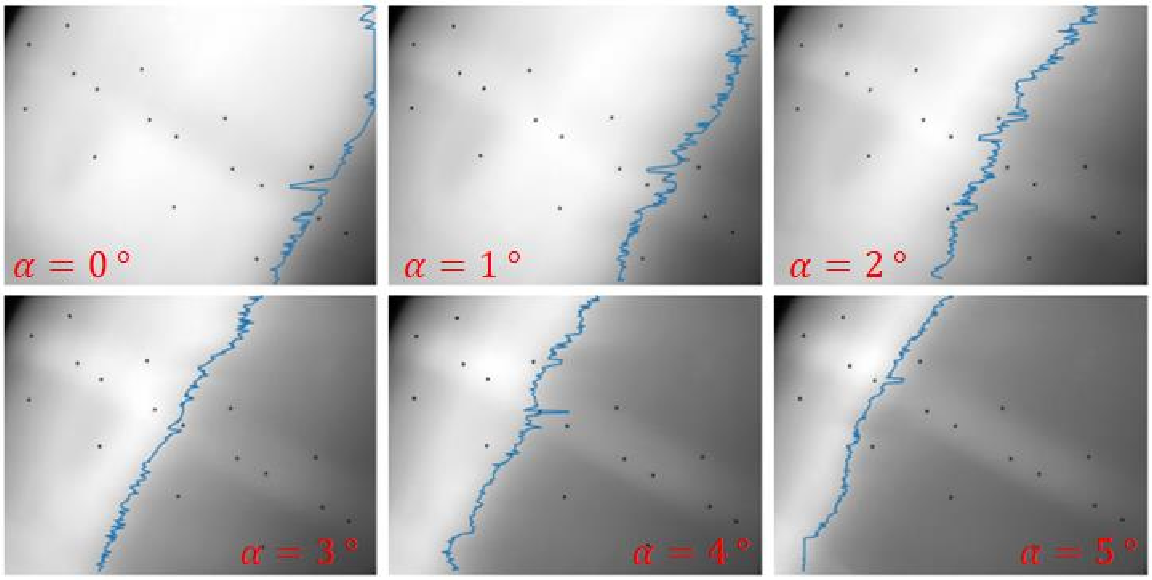

Figure 5.14: Infrared Results for Transition Line Detection at Re = 765000.

5.3.5 Swept Wing Infrared Images - Re = 915000

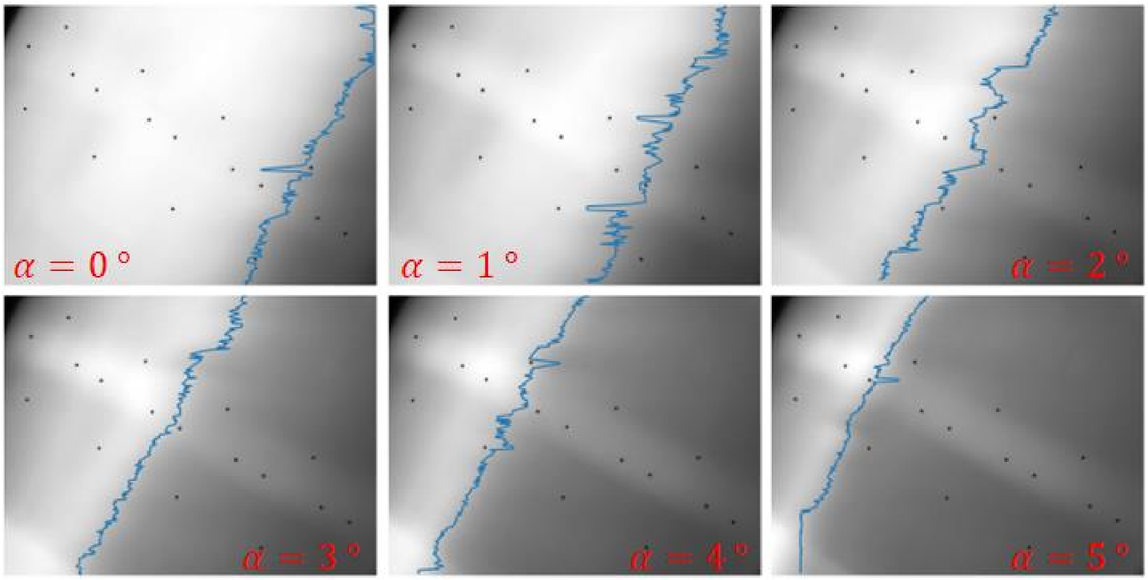

Figure 5.15: Infrared Results for Transition Line Detection at Re = 915000.

5.3.6 Transition Front position in terms of wing cord in function of the angle of attack.

Table 5.1: Medium Value for the Transition Front to Turbulence Position

$\alpha\,[\,^\circ\,]$	Re = 450000	Re = 650000	Re = 720000	Re = 765000	Re = 915000
	x_{tr}/c	x_{tr}/c	x_{tr}/c	x_{tr}/c	x_{tr}/c
0	0.772	0.759	0.785	0.788	0.747
1	0.747	0.756	0.788	0.716	0.671
2	0.742	0.680	0.548	0.586	0.535
3	0.741	0.527	0.563	0.472	0.456
4	0.456	0.412	0.460	0.400	0.374
5	0.378	0.354	0.377	0.327	0.311
6	0.444	0.288	0.307	-	-
7	0.351	0.232	0.274	-	-
8	0.290	0.170	0.253	-	-
9	0.189	-	-	-	-
10	0.141	0.144	-	-	-
11	0.098	0.100	-	-	-
12	0.091	0.094	-	-	-
13	0.087	0.089	-	-	-
14	-	0.083	-	-	-

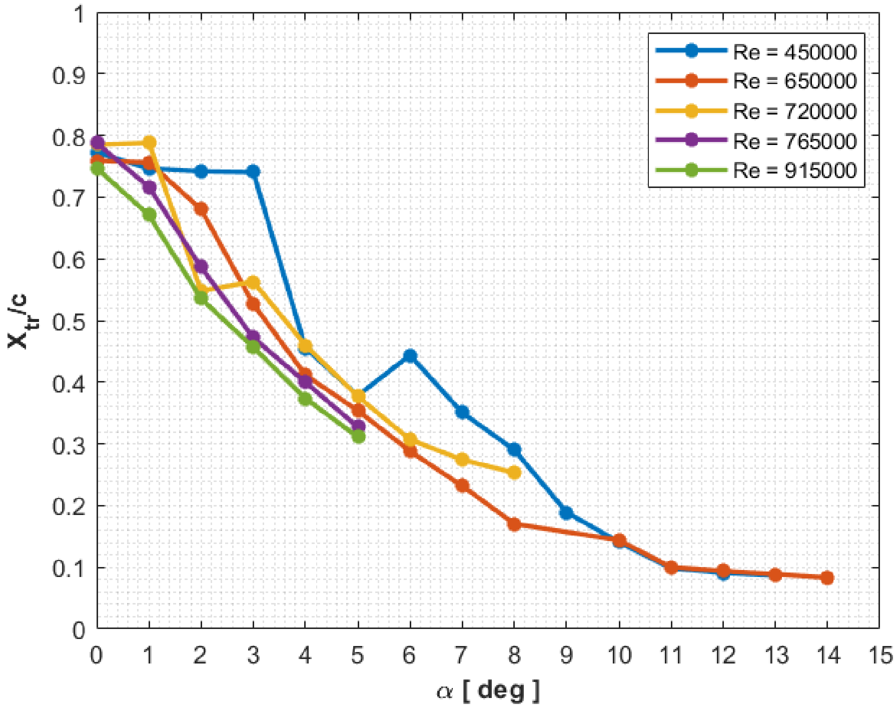

Figure 5.16: Swept Wing Transition to Turbulence Position in Function of the Angle of Attack

5.4 Swept Wing Experiments Results Discussion

the phenomenology chapter, it is anticipated that the only transition mechanisms affecting the tested swept wing model are the TS waves and the CFV. Consequently, an increase in both Reynolds number and angle of attack should result in the advancement of the transition front. Under constant environmental conditions for pressure and temperature, the increasing of Re means that higher velocity values are acting on the wing and thus higher kinetic energy is being inserted in the system This increase in energy may lead to the accelerated development and manifestation of instabilities Similarly, by increasing the alpha angle augments the velocity differential between the upper and lower body, thereby increasing the kinetic energy of the upper body and, in turn, the energy transferred to the instabilities.

Thereby, a careful look at the IR images and at Fig 5.16 at Sec 5.3 elucidates that, in general, an increase in the angle of attack leads to the transition front moving progressively closer to the wing leading edge. Furthermore, it is evident that the heating method employed to enhance the IR image contrast has proven effective, as even in the raw IR images, the transition front position is discernible and further enhanced by the image processing code. With respect to the line drawn to represent the transition front to turbulence, it is important to note that it is not perfectly straight, mirroring the dynamic and chaotic nature of the transition front, which may undergo changes in position due to minimal variations in the system. Nonetheless, the transition front, when initial conditions remain relatively constant, tends to assume a mean position along both the chord and the wingspan. Regarding the effects of an increased angle of attack, the following points provide discussions on each notable behavior:

- Exceptions to the observed behavior were noted in the cases of Re = 450000 to $\alpha = 4\,°$ and $\alpha = 5\,°$ and Re = 720000 to $\alpha = 2\,°$. In these instances, the transition front position was closer to the leading edge compared to the subsequent angle of attack for the respective Reynolds number. This deviation suggests that, in these specific scenarios, additional boundary layer mechanisms may be influencing the wing beyond the typical crossflow Instability (CFI) and Tollmien-Schlichting (TS) waves. One plausible explanation is related to the airfoil profile, which is designed to promote laminar flow and is subjected to a relatively low Reynolds number. Under these conditions, it is conceivable that air molecules lose kinetic energy, potentially leading to boundary layer separation. Upon reattachment to the wing, rather than forming a laminar boundary layer, turbulence is initiated, causing the transition through laminar separation, a mechanism less commonly observed. This hypothesis could be further substantiated if pressure coefficient distribution plots exhibited signs of boundary layer detachment, such as abrupt variations or discontinuities around the transition position detected in the infrared images. However, since these plots appear to be relatively smooth in this regard, conclusive inferences are challenging to draw. While some minor fluctuations in the pressure coefficient distribution do exist, they may be attributed to typical experimental variability. Another conceivable explanation for these observations is that, at certain angles of attack, different types of instabilities that affect the system become more prominent or exhibit altered behavior, thereby causing discontinuities in the transition front position plot.

- For the first two tested Reynolds numbers, where it was possible to explore a significant portion of the polar at higher angles of attack near the stall point (specially for Re = 450000, as seen in Sec 5.2.2) the transition front has shifted so close to the leading edge that laminar flow was nearly absent.

- A particular focus should be directed towards Re = 450000 to $\alpha = 14\,°$, where the transition front advanced significantly to the extent that the image processing code could not accurately pinpoint its location, resulting in the generation of a somewhat random curve. It is also conceivable that under this condition, a stall or, at the very least a stall imminence occurred, as evidenced by the observed behavior in the corresponding $CL\ x\ \alpha$.

Regarding the increasing of the Reynolds number, as expected, the transition front is consistently moving forward. However, there are exceptions noted for Reynolds numbers of 650000 and 720000 where the transition front, in general, appears to be positioned farther from the leading edge (again, except for the before mentioned $\alpha = 2\,°$ condition). Although the absolute position between the corresponding alpha angles for the same Re is not much, this could mean that the crossflow influence in the flow is changing around Re = 720000. One possibility is that, even though the model sweep angle is expected to favor stationary modes, the crossflow instability might be transitioning from a stationary characteristic to a traveling one due to increased pressure gradients or perturbations within the system. This shift could alter the influences of CFI and TS waves on the transition process. Usually, this kind of behavior that disrupts the order of previous steps, in this case the evolution of the transition front with the Reynolds number, is caused by a change of the process characteristics that is governing the phenomenon.

Regarding the pressure coefficient and aerodynamic forces experiments, it can be affirmed that they exhibit no discrepancies, thereby reinforcing the validity and reliability of the results obtained from the infrared analysis of the boundary layer transition to turbulence.

The works presented at bibliography review chapter that employed similar techniques did not focus on illustrating the evolution of the boundary layer on a swept wing model concerning Reynolds number and angle of attack, as is the primary focus of this research. Nonetheless, it is still possible to make relative comparisons. For example, Boiko et al. (2021) conducted tests on a 45° swept wing model using a thermography camera with a free stream velocity of 50 m/s and zero angle of attack. Under these conditions, the boundary layer transition was observed at 82 % of the wing chord. In the present work, at a Reynolds number of 915,000 (approximately 30 m/s free stream velocity) with zero angle of attack, the transition occurred at 74.7 % of the chord. One might anticipate that, given the higher velocity and sweep angle in Boiko et al. (2021) study, the transition should occur further forward compared to the present work. However, the differences in wing cross-section and, likely, wing chord, highlight the significant influence of geometry on the transition location. Nevertheless, both studies found the transition closer to the trailing edge. Moreover, for this angle of attack, it is likely that the T-S waves were the predominant transition mechanism. Therefore, for a deeper understanding of the swept wing's behavior during the transition phenomenon, the next section compares the infrared results of the swept wing with those of the straight-wing case.

5.5 Swept x Straight Wing IR Image Comparison

In this section, a comparative analysis is conducted between the straight model examined in Eguea (2022) and the swept wing model of the present study, focusing on the position of the boundary layer transition front. It is essential to note that while the Reynolds Numbers tested do not match precisely, they are in proximity. Additionally, as the previous study primarily aimed to investigate the influence of the propeller on boundary layer transition, the range of angles of attack for each Reynolds number differs. Consequently, the comparison is made by aligning the closest Reynolds number to the matching angle of attack. Table 5.2 provides the information regarding the corresponding test points for each model. In the last column, with all other parameters held constant, the velocity difference between each Reynolds number is highlighted to illustrate that there is no significant deviation when comparing similar Reynolds numbers. Subsequently, like the previous analysis, the mean value of the transition front is plotted to facilitate the comparison.

Table 5.2: Matrix for Swept x Straight Models Comparison

Re Swept Model	**Re Straight Model**	**Angle of Attack Range [deg]**	**Velocity Difference [m/s]**
450000	486000	0 to 7	1.20
650000	655000	2 and 5	0.18
765000	787000	2 and 5	2.22
915000	950000	0 to 5	1.17

5.5.1 $\boldsymbol{Re_{swept} = 450000 \ \ x \ \ Re_{straight} = 486000}$

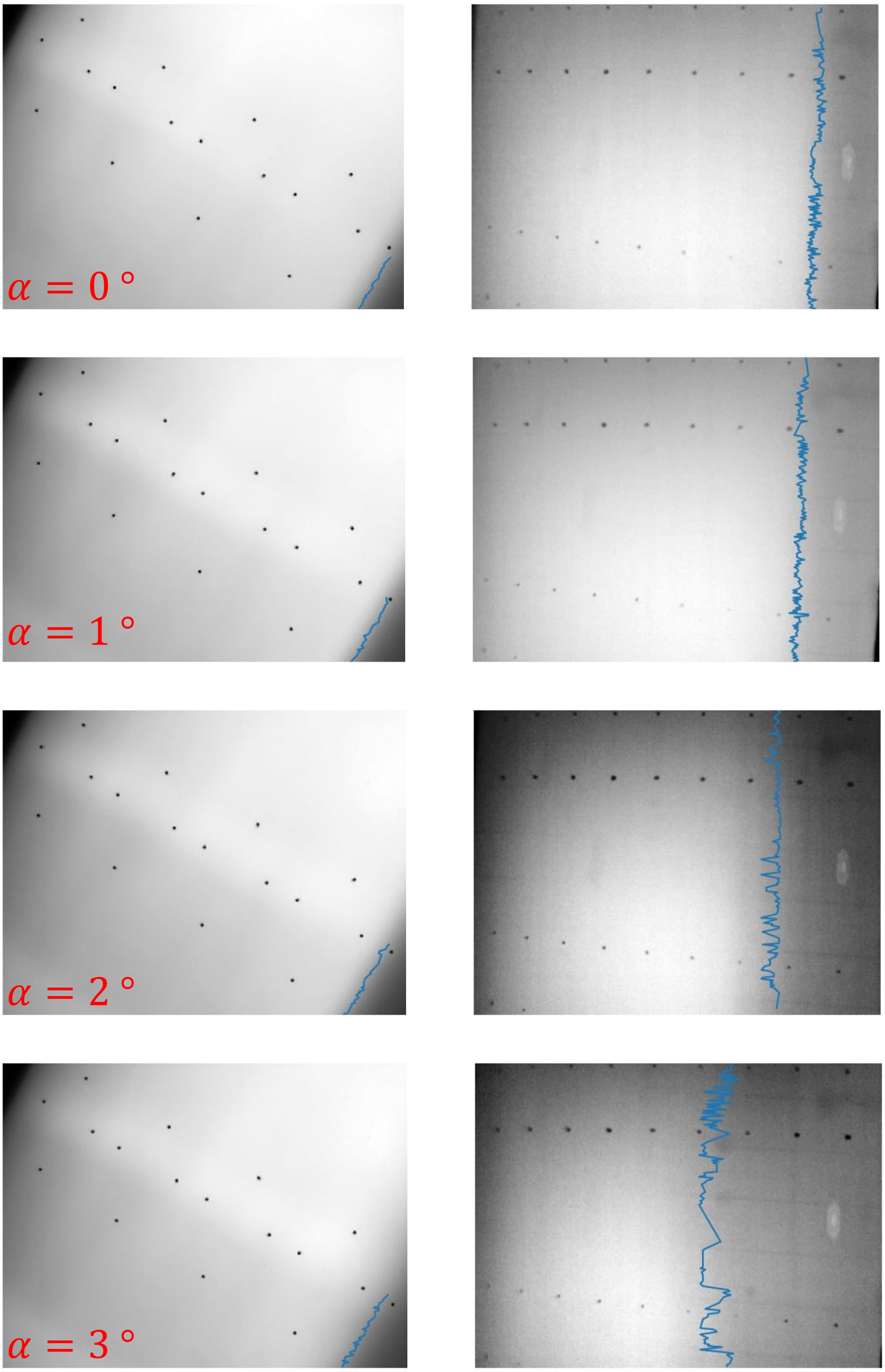

$(a)\ Swept\ Wing$ $(b)\ Straight\ Wing$

Figure 5.17: Swept x Straight wing comparison for Re = 450000 and $\mathbf{0}\,° \le \boldsymbol{\alpha} \le \mathbf{3}\,°$

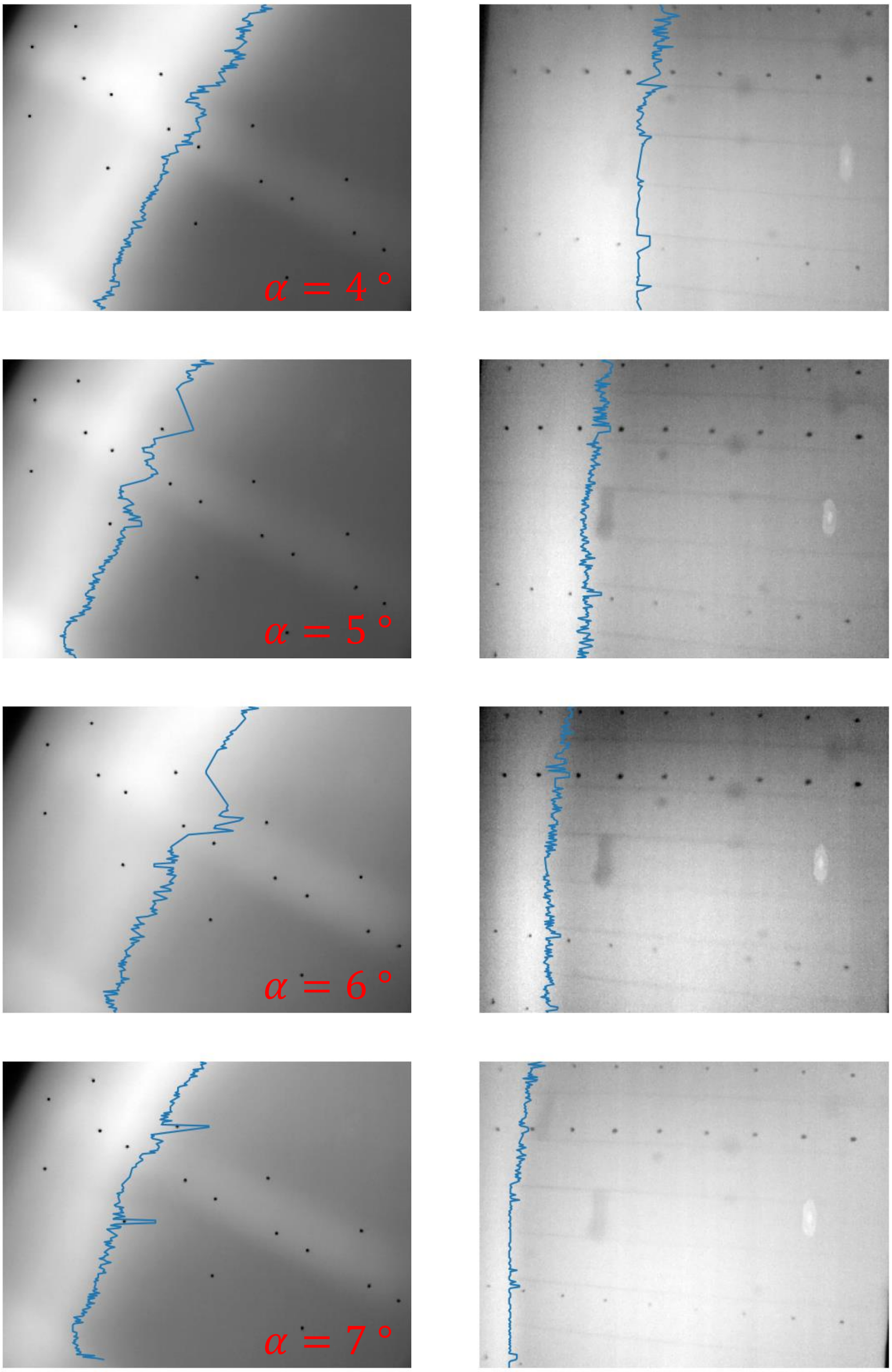

$(a)\ Swept\ Wing$ $(b)\ Straight\ Wing$

Figure 5.18: Swept x Straight wing comparison for Re = 450000 $\mathbf{4}\,° \leq \boldsymbol{\alpha} \leq \mathbf{7}\,°$

5.5.2 $Re_{swept} = 650000 \;\; x \;\; Re_{straight} = 655000$

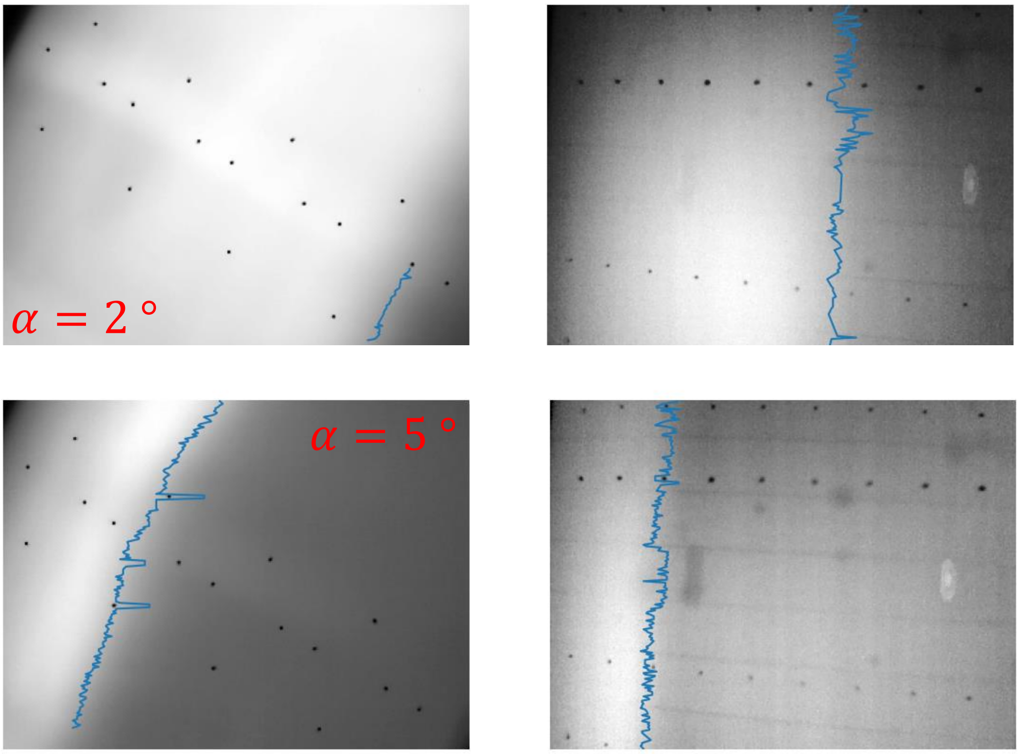

$(a)\ Swept\ Wing$ $(b)\ Straight\ Wing$

Figure 5.19: Swept x Straight wing comparison for Re = 650000 $\mathbf{2}° \le \boldsymbol{\alpha} \le \mathbf{5}°$

5.5.3 $\boldsymbol{Re_{swept} = 765000 \quad x \quad Re_{straight} = 787000}$

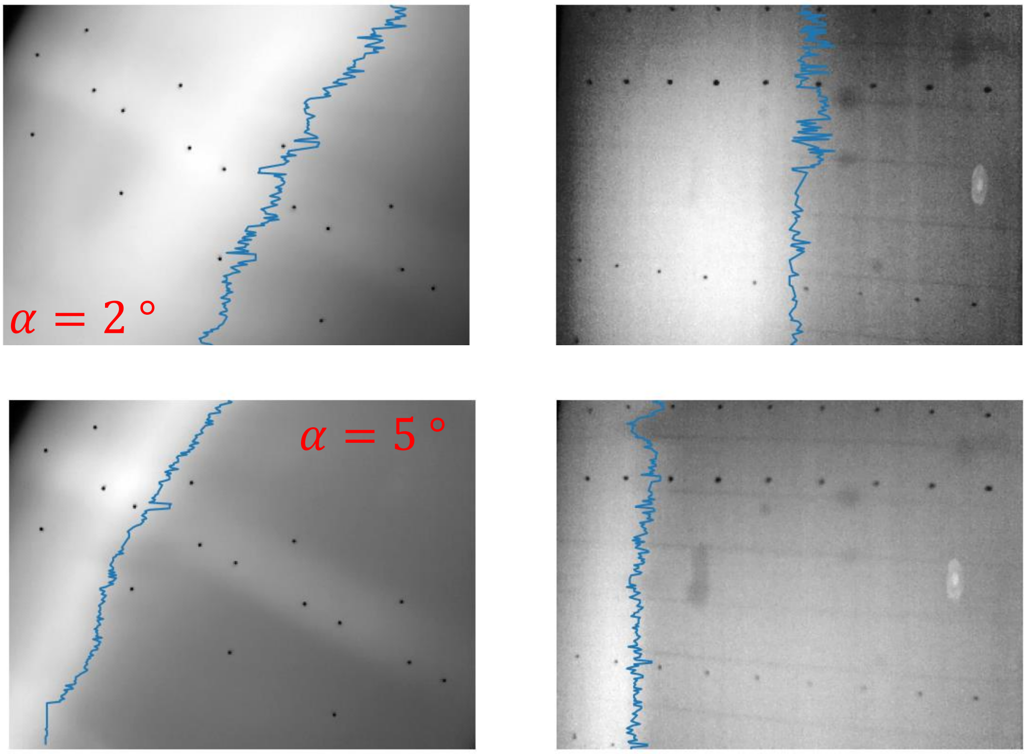

$(a)\ Swept\ Wing$ $(b)\ Straight\ Wing$

Figure 5.20: Swept x Straight wing comparison for Re = 765000 $\mathbf{2}° \leq \boldsymbol{\alpha} \leq \mathbf{5}°$

5.5.4 $Re_{swept} = 915000$ x $Re_{straight} = 950000$

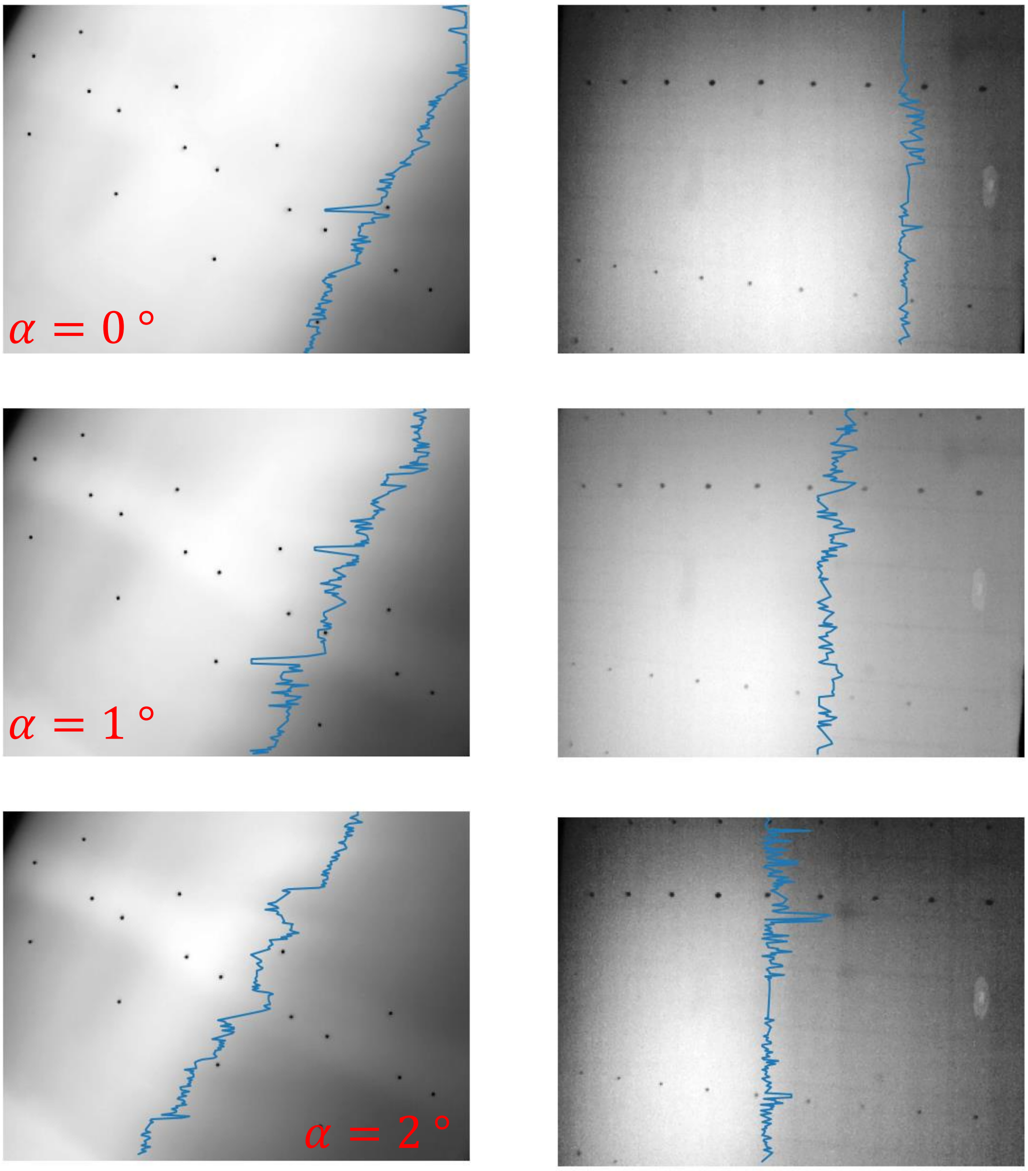

(a) $Swept\ Wing$ (b) $Straight\ Wing$

Figure 5.21: Swept x Straight wing comparison for Re = 915000 $\mathbf{0}° \le \boldsymbol{\alpha} \le \mathbf{2}°$

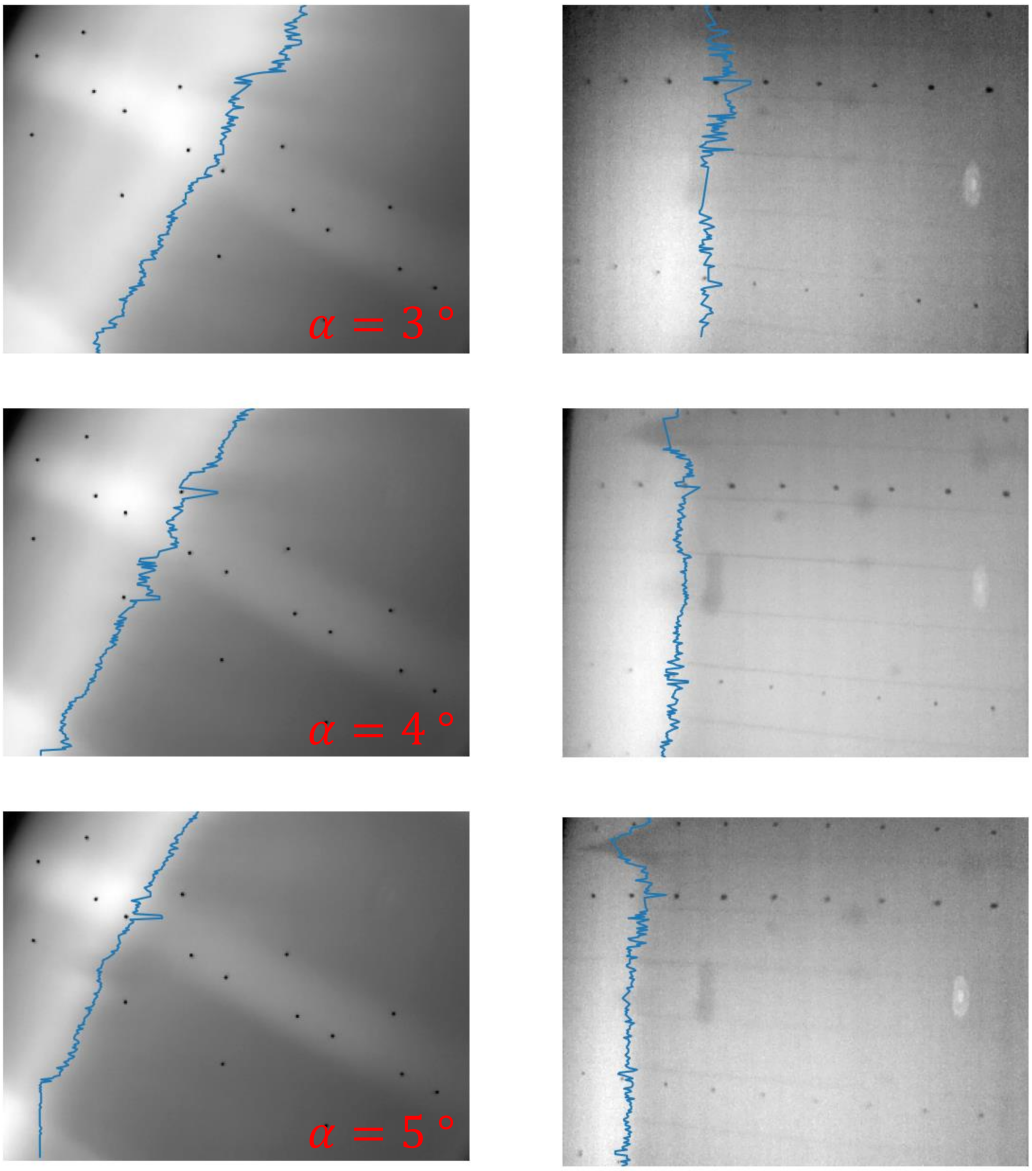

(a) *Swept Wing* (b) *Straight Wing*

Figure 5.22: Swept x Straight wing comparison for Re = 915000 $\mathbf{3}° \leq \boldsymbol{\alpha} \leq \mathbf{5}°$

5.5.5 Transition Front position in terms of wing cord in function of the angle of attack.

Table 5.3: Transition Front to Turbulence Position for the Swept x Straight Models

Alpha	Swept 450000	Straight 486000	Swept 650000	Straight 655000	Swept 765000	Straight 787000	Swept 915000	Straight 950000
	x_{tr}/c	x_{tr}/c	x_{tr}/c	x_{tr}/c	x_{tr}/c	x_{tr}/c	x_{tr}/c	x_{tr}/c
0	0.772	0.878	-	-	-	-	0.747	0.788
1	0.747	0.820	-	-	-	-	0.671	0.640
2	0.742	0.761	0.680	0.661	0.586	0.571	0.535	0.501
3	0.741	0.627	-	-	-	-	0.456	0.389
4	0.456	0.459	-	-	-	-	0.374	0.290
5	0.378	0.320	0.354	0.289	0.327	0.243	0.311	0.216
6	0.444	0.250	-	-	-	-	-	-
7	0.351	0.186	-	-	-	-	-	-

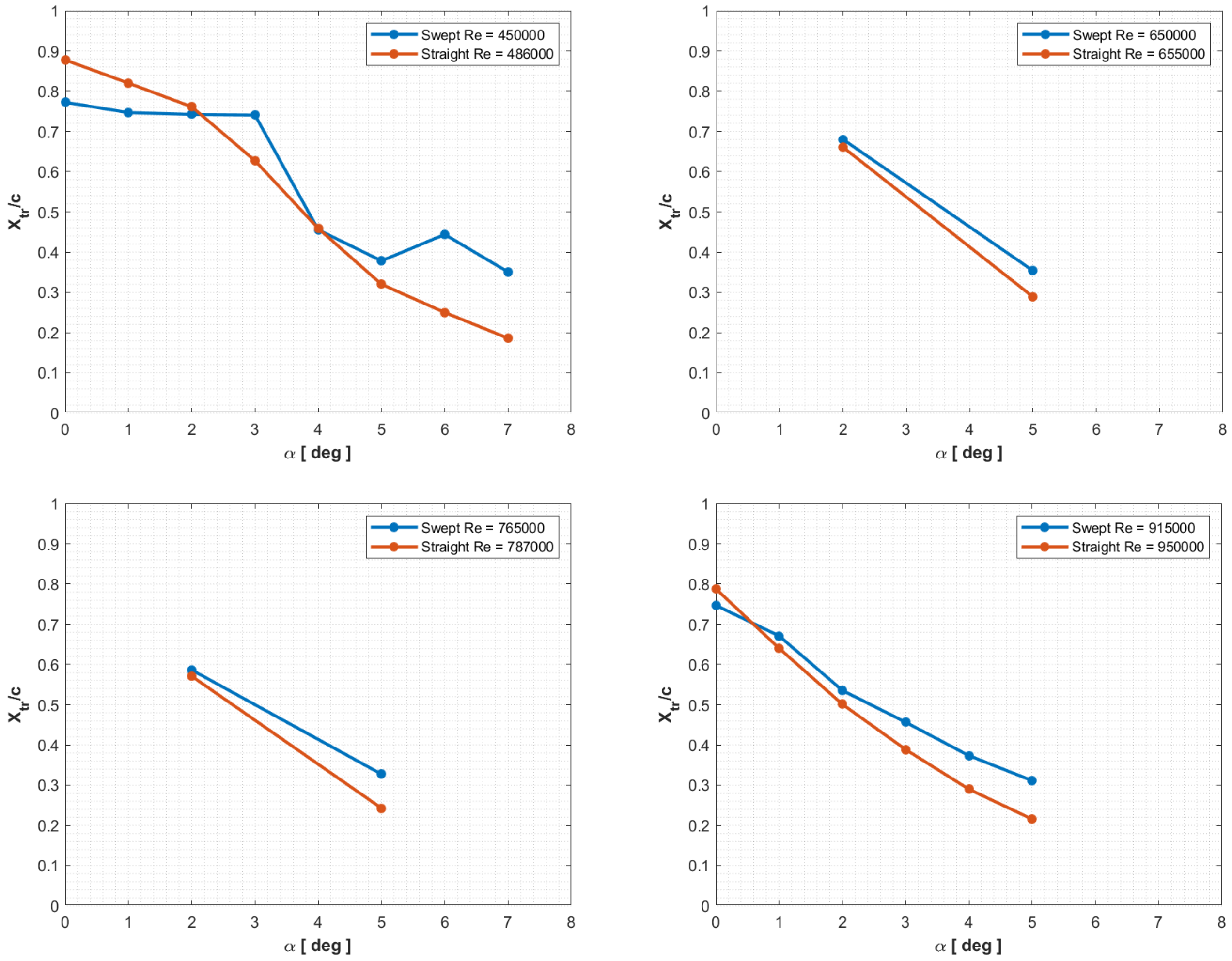

Figure 5.23: Swept x Straight Wing Transition to Turbulence Position in Function of the Angle of Attack

5.6 Swept x Straight Wing Infrared Results Discussion

As both models underwent testing using the same equipment, it becomes feasible to isolate the impact of wing material on the obtained IR images. Consequently, while both models produced high-quality images, it is discernible that the images from the swept model, constructed from fiberglass and coated with black matte paint, exhibited superior quality. Besides, there was no need to involve the model in any other material to guarantee the images quality.

Regarding the results themselves, once again, they did not entirely align with the initial expectations. Given that the swept wing model involves two transition mechanisms (T-S waves and CFI), whereas the straight wing should only have T-S waves, one might initially assume that the interplay between T-S waves and CFI would advance the transition for all combinations of Reynolds numbers and angles of attack. Consequently, the swept wing would exhibit a transition closer to the leading edge than the straight model. However, this hypothesis may indeed hold true, but there might be other phenomena influencing the transition of the straight wing.

Although the swept wing did exhibit a transition location closer to the leading edge for small angles of attack, suggesting that the influence of stationary crossflow instabilities on the evolution of Tollmien-Schlichting (T-S) waves plays a role, a counterintuitive behavior was observed for higher angles of attack in the straight wing. Initially, one might expect the straight wing transition process to be solely driven by T-S wave evolution, which could lead to a delayed transition location when compared to its swept counterpart, where crossflow is also present to accelerate the process. Given the significant differences in transition locations for higher and lower angles of attack, it is difficult to discount the influence of crossflow on the swept wing behavior. However, for lower alpha angles, the transition locations for both wings should theoretically coincide or at least be in closer proximity. Therefore, a plausible explanation is that at higher alpha angles, the laminar airfoil used may cause boundary layer separation on the straight wing, resulting in a transition driven by this alternative mechanism rather than T-S wave evolution.

As suggested by Borodulin et al. (2019b), the transition to turbulence can also be triggered by laminar separation. This is especially pertinent for laminar airfoils, such as the one utilized in the current and prior studies, where the transition to turbulence may not be solely induced by T-S waves. Instead, it can occur due to boundary layer detachment and the formation of recirculation bubbles. The theory posits that laminar flow is more prone to experiencing boundary layer detachment, leading to the flow's inability to progress to a turbulent state. Consequently, it detaches from the surface, and, upon reattachment, the flow is turbulent, originating from a recirculation bubble. In the broader context, this phenomenon is interpreted as a transition to turbulence process, as the flow reintegrates with the wing.

While not within the scope of the current study, with the intention of delving further into this subject and potentially laying the groundwork for future research, the laminar airfoil employed was subjected to simulation in XFLR5 to ascertain whether the simulation would identify a similar discontinuity, which might once again indicate the presence of a recirculation bubble. Simulations were conducted at Reynolds numbers of 486000 and 950000 at the angles of attack of 0 and 2 º. Figure 5.24 presents the results and Table 5.4 contrasts the transition front results obtained from the software simulation with those from the wind tunnel experiments.

Table 5.4: Wind Tunnel x XFLR5 Transition Front Position Resutls

Alpha	Wind Tunnel 486000	XFLR5 486000	Wind Tunnel 950000	XFLR5 950000
	x_{tr}/c	x_{tr}/c	x_{tr}/c	x_{tr}/c
0	0.878	0.871	0.788	0.827
2	0.761	0.749	0.501	0.610

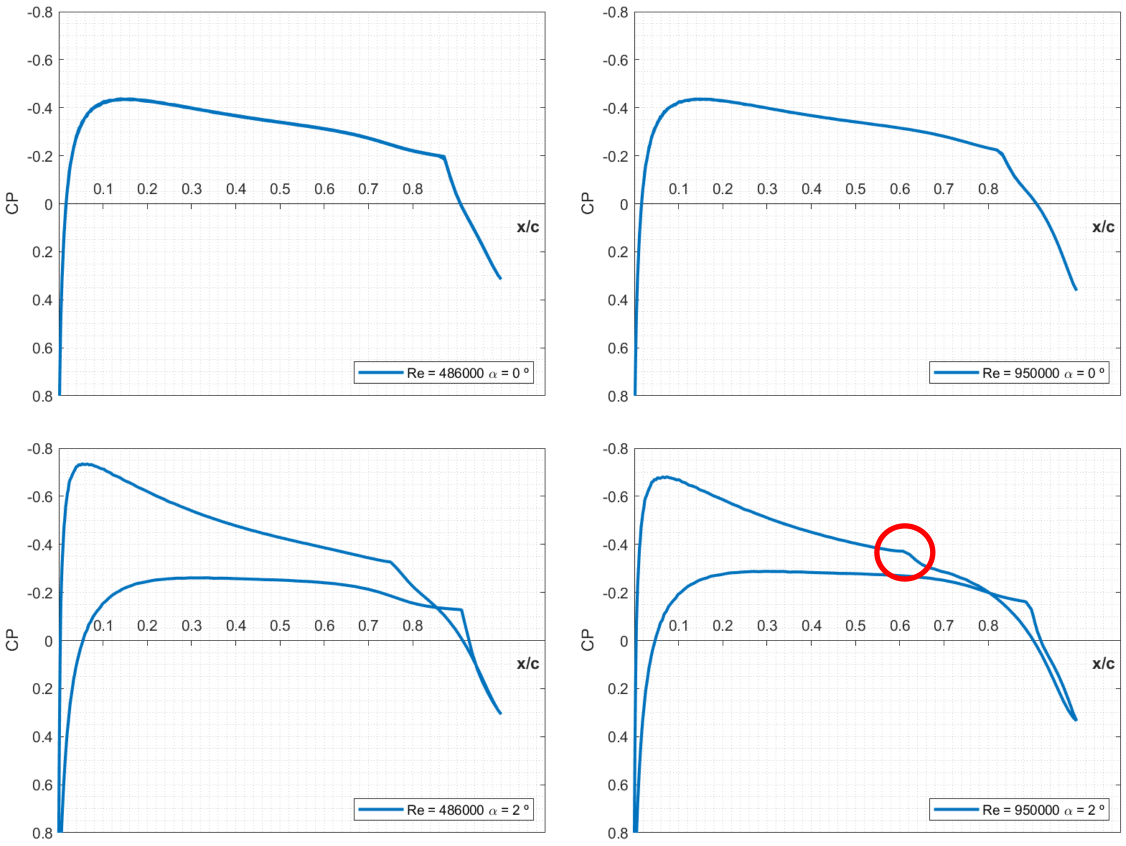

Figure 5.24: Pressure Distribution simulated at XFLR5 for the Straight Wing

As observed in the plots, the discontinuity in the simulated pressure distribution occurs at values closely aligned with the transition front detection results obtained via infrared thermography in the wind tunnel experiments. This alignment is particularly evident in the instance where the straight wing exhibited a transition front position closer to the leading edge than its swept counterpart, which lends support to the notion of the transition process being influenced by a recirculation bubble. Also, after XFLR5 results, the transition front happens really close to the discontinuity "edge", which provides another indicator of the potential influence of a recirculation bubble in the transition process. These insights, while preliminary, highlight the need for further experiments and simulations to develop a more precise theoretical understanding of the observed phenomena. Such future endeavors may include conducting a broader range of experiments involving varying Reynolds numbers and angles of attack, as well as comprehensive mapping of the three-dimensional velocity field within the boundary layer on this wing.

Still, although the very same airfoil has been used on the swept wing, the presence of the crossflow may be altering the whole picture, and for this specific case, instead of advancing the transition front location in comparison to its straight counterpart, the crossflow may be energizing the boundary layer and doing so, letting it attached to the wing not allowing the presence of recirculation bubbles to appear since there were no discontinuations observed in the pressure distribution of the swept wing.

Upon analyzing Figure 5.23, for all of Re = 450000, it is clear that the for the swept wing, until 2 º of alpha, the transition location is closer to the leading edge, which could be attributed to the presence of the CFI which appear to advance the development of the T-S waves, and thus advancing the transition location. After 2 º of alpha, the straight wing presents the more advanced transition location, probably due to the phenomena before described which usually is more prominent when increasing the angle of attack. For the highest Reynolds, the crossing point is now around 1 º of alpha, and besides there are only two points for each intermediary Reynolds numbers, it appears to keep the tendency of the crossing point, this time being located around 2 º of alpha, inside the interval of the lowest and highest Reynolds number.

To conclude the discussion of the results in this work, the following section offers a comparative analysis of the present findings concerning the model used, applied techniques, and the outcomes achieved in relation to other research efforts.

CHAPTER VI

6. CONCLUSION

The frictional parcel of the drag force that acts on a wing is the one that shows the most reducing potential for the future of the aeronautic industry. This frictional drag arises from the viscous interaction of airflow with the wing surface, making it highly susceptible to aerodynamic phenomena occurring within the boundary layer. These phenomena include the state of the boundary layer, whether it is turbulent or laminar, as well as the attachment of the boundary layer to the wing surface. It is well-established that a turbulent boundary layer results in higher viscous forces compared to a laminar one. Therefore, this study focuses on characterizing the boundary layer on a swept wing model and comparing it to a straight-wing case to understand the behavior of the transition front position between them, utilizing infrared thermography. Also, to corroborate with the infrared results of the swept wing, the pressure field and aerodynamic efforts of the swept wing have been analyzed.

The infrared thermography results have indicated that, in general, the transition front on the swept wing model moves closer to the leading edge as the Reynolds number and angle of attack increase, consistent with theoretical expectations. However, in specific situations, an unexpected inversion of this behavior was observed when increasing the angle of attack, causing the transition to occur closer to the leading edge than in the previous case. Another unanticipated situation occurred during the analysis of Reynolds number evolution when, at Re = 720,000, transition front values were found further from the leading edge than in the previous Reynolds experiment. At this point, these are only preliminary observations. Unfortunately, due to the unavailability of suitable equipment, it was not feasible to measure the velocity field within the boundary layer. Nonetheless, this limitation does not diminish the quality of the results. Monitoring the evolution of the transition front via an infrared camera represents a significant advancement in our understanding of the complex transition phenomena, particularly for swept wings. This work is a valuable contribution to the field, as it provides material experimentation and evaluation of the transition phenomenon on swept wings across a wide range of Reynolds numbers and angles of attack.

The second segment of this discussion focused on examining the disparities in the transition front location between straight and swept wings. It was observed that until around 2º of angle of attack, the presence of Crossflow Instabilities (CFI) could be advancing the development of Tollmien-Schlichting (T-S) instabilities. However, for higher angles of attack, the hypothesis of boundary layer detachment and the emergence of recirculating bubbles might be altering the transition process. To reinforce this concept, a pressure field simulation for the straight wing indicated boundary layer detachment or at least the presence of a recirculation bubble at the transition location. This hypothesis would gain further support through the acquisition of three-dimensional velocity field data.

Finally, it is expected that with the methods presented for boundary layer transition detection, the present work can be used to be presented as another step for future ones to be based on so that the transition to turbulence on wings can be each time better understood being it via material experimentation on numeric-computational simulations so that soon the Brazilian laboratories may be able to propose active flow control devices and techniques. Also, it may be used as a tool to attract investments for the laboratories involved in the acquisition of new equipment that would aid in the boundary layer transition mechanisms involved.

6.1 Future Works Perspective

Subsequent research efforts should aim to further investigate the discrepancies and either validate or invalidate the hypotheses proposed in this study. Additionally, experimentation involving wing configurations closer to those utilized in commercial aviation, including aspects such as aspect ratio, torsion angles, and concepts related to aerodynamic devices, should be conducted. These investigations collectively contribute to the ongoing pursuit of reducing viscous drag, enabling the operation of more fuel-efficient aircraft or those powered by environmentally friendly fuel sources.

The data generated in this study, spanning from pressure data to the detection of transition front positions via infrared thermography, can serve as a foundational resource for future research endeavors. These endeavors should encompass the acquisition of velocity field data within the boundary layer and the establishment of a comprehensive database to facilitate the development of mathematical models for describing or predicting the transition behavior in this wing configuration.

To offer a more comprehensive explanation for the observations made, it is imperative to conduct experiments that involve the measurement of boundary layer velocity fields. These experiments would enable the verification of instability frequencies, their nature, and whether the predominance of specific instability types such as Tollmien-Schlichting (T-S) waves, stationary Crossflow Instabilities (CFI), or traveling CFI is subject to change. Furthermore, these experiments could confirm the presence of boundary layer detachment or the existence of recirculating zones. Consequently, they would shed light on whether the transition to turbulence behavior is influenced by shifts in the predominance of specific transition mechanisms.

REFERENCES

ABBAS, A.; BUGUEDA, G.; FERRER, E.; FU, S.; PERIAUX, J.; PONS-PRAT, J.; VALERO, E.; ZHENG., Y. **Drag Reduction via Turbulent Boundary Layer Flow Control.** Science China – Technological Sciences, 2017. https://doi.org/10.1007/s11431-016-9013-6

ALDERMAN, J.; ROLSTON, S.. **A Method of Reducing the Drag of Transport Wing**. Washington, D.C: AIAA Aviation 2016-3115. 34th AIAA Applied Aerodynamics Conference, 2016. https://doi.org/10.2514/6.2016-3115

ANDERSON, J. D. Jr. **Fundamentals of aerodynamics**. 5. ed. New York, NY: McGraw-Hill Series in Aeronautical and Aerospace Engineering, 2010. 1131 p. (a)

ANDERSON, J. D. Jr. **Introduction to Flight**. 8. ed. New York, NY: McGraw-Hill Series in Aeronautical and Aerospace Engineering, 2015. 928 p. (b)

BARLOW, E. B; RAE, W. H. Jr.; POPE, A. **Low-speed wind tunnel testing**. 3. ed. New York, NY: John Wiley & Sons, 1999.

BECK, N.; LANDA, T.; SEITZ., A; BOERMANS., L; LIU., Y; RADESPIEL., R. **Low-speed wind tunnel testing**. New York, NY: Energies 2018, 2018. 252 p. https://doi.org/10.3390/en11010252

BELISLE, M.J. **Aerodynamic design for swept-wing laminar flow**. December 2013. Doctor of Philosophy Thesis. Texas A&M University.

BOIKO, A. V.; BORODULIN, V. I.; IVANOV, A. V.; KIRILOVSKIY, S. V.; MISCHENKO, D. A.; POPLAVSKAYA, T. V. **Validation of a laminar-turbulent transition prediction technique for a swept-wing boundary-layer flow**. Journal of Physics: Conference Series 2057 012081, 2021. https://doi.org/10.1088/1742-6596/2057/1/012081

BORODULIN, V.i.; KACHANOV, Y.s.; IVANOV, A. V.; HANIFI, A. **Laminar-turbulent transition delay on a swept wing.** AIP Conference Proceedings, 2016. DOI 10.1063/1.4964007. (a) https://doi.org/10.1063/1.4964007

BORODULIN, V.i.; IVANOV, A. V.; MISCHENKOFI, D. A.; ÖRLÜ, R.; HANIFI, A.; HEIN, S. **Experimental and theorical study of swept-wing boundary layer instabilities:** Unsteady crossflow instability. Phys. Fluids 31, 064101, 2019. (b) https://doi.org/10.1063/1.5094609

CRAWFORD, B. K.; DUNCAN, G. T. JR; WEST, D. E.; SARIC, W.S. **Laminar-turbulent boundary layer transition imaging using IR thermography**. Optics and Photonics Journal. 2013 233-239 p. https://doi.org/10.4236/opj.2013.33038

CUSHMAN-ROISIN, B.; BECKERS, J. M. **Introduction to Geophysical Fluid Dynamics:** Physical and Numerical Aspects. 1. ed. Pearson Education, Inc, 2006. 720 p.

DAGENHART J.R.; SARIC W.S. **Crossflow stability and transition experiments in swept-wing flow**. Hampton, Virginia: National Aeronautics and Space Administration. Langley Research Center. 1999.

EGUEA J. P. **Influência de hélices pusher na camada limite e forças aerodinâmicas de uma asa laminar.** 2022. 138 f. PHD Thesis - Universidade de São Paulo (USP). São Carlos, SP, Brazil.

FENDT, M.; DUVELLEROY, M. Airbus' "BLADE" laminar flow wing demonstrator makes first flight. **Airbus**, 2017. Available in: https://www.airbus.com/en/newsroom/press-releases/2017-09-airbus-blade-laminar-flow-wing-demonstrator-makes-first-flight. Access: 22 May 2023.

GLEICHAUF D.; OEHME F.; SORG M.; FISCHER A. **Laminar-turbulent transition localization in thermographic flow visualization by means of principal component analyses**. Applied Sciences. 2021. https://doi.org/10.3390/app11125471

GUDMUNDSSON, S. **General aviation aircraft design**: Applied methods and procedures. Butterworth-Heinemann. 2014. DOI https://doi.org/10.1016/C2011-0-06824-2.

HIROKAWA S.; ETO K.; FUKAGATA K.; TOKUGAWA N. **Experimental investigation of friction drag reduction on an airfoil by passive blowing**. Journal of Fluid Science and Technology. Vol. 15 No. 2. Paper No. 19-00472. 2020. https://doi.org/10.1299/jfst.2020jfst0011

HUGH W. C. and STEELE W. G. **Experimentation, validation and uncertainty analysis for engineers**. 4 ed John Wiley & Sons, Inc. 2018. ISBN:9781119417989

HOESSLIN, V. S.; STADLBAUER, M.; GRUENDMAYER J.; KÄHLER, C.J. **Temperature decline thermography for laminar-turbulent transition in aerodynamics**. Exp Fluids 2017, p58-129. https://doi.org/10.1007/s00348-017-2411-1

KLEINUBING M.; BIDINOTTO J. H.; CATALANO, F. M.; BELO E. M. 22nd International Congress of Mechanical Engineering (COBEM 2013). November 2013. Ribeirão Preto, SP, Brazil. **Thermography applied on boundary layer transition visualization.** p 3-7.

KOWNACKI, A. **Weather Phenomena: What is Kelvin-Helmholtz Instability?** 2019. Available in: https://www.globalweatherclimatecenter.com/weather-education/weather-phenomena-what-is-kelvin-helmholtz. Access in 02 November 2021.

KURZ A. **In-flight application of dieletric barrier discharge plasma actuators for active wave control**. 2017. 122 f. Master Dissertation - Vom Fachbereich Maschinenbau an der Technischen Universität Darmstadt. Darmstadt.

MENDONÇA, M.T. DE; MEDEIROS, M.A.F. DE. **Instabilidade hidrodinâmica e transição para turbulência com aplicações em engenharia e meteorologia**. 159 f. 2006.

MERZ. C. B.; RICHTER K. RAFFEL M. **Unsteady boundary layer transition measurements by differential infrared thermography**. AIAA Journal. 2014. https://doi.org/10.2514/1.J053235

METHEL L.; MÉRY F.; FORTE M.; VERMEERSCH O. The 8th European Congress on Computational Methods in Applied Sciences and Engineering, ECCOMAS Congress 2022. Jun 2022, Oslo, Norway. hal-03716333. **Laminar Flow Control along the attachment Line of a Swept Wing**. https://doi.org/10.23967/eccomas.2022.160

MOSER, K. et al. **Visualization of Taylor–Couette and spiral Poiseuille flows using a snapshot FLASH spatial tagging sequence**. Magnetic Resonance Imaging, 2000. 199-207 p. https://doi.org/10.1016/S0730-725X(99)00121-6

SERPIERI, J. **Cross-flow instability**: Flow diagnosis and control of swept wing boundary layers. 2018. 200 f. PHD Thesis – TU Delft. Delft. https://doi.org/10.4233/uuid:3dac1e78-fcc3-437f-9579-048b74439f55

SILVEIRA NETO, A. **Escoamentos turbulentos:** Análise física e modelagem teórica. 1. ed. Uberlândia, MG: Composer, 2022. 653 p.

SOUZA, L. F. DE; MEDEIROS M.; MENDONÇA, M. T. DE; KLOKER, M. J. **Seeding of Görtler vortices through a suction and a blowing strip**. Journal of the Brazilian Society of Mechanical sciences and Engineering. 2004. https://doi.org/10.1590/S1678-58782004000300003

RANJAN, D. Rayleigh-Bénard Convection. **Gatech**, 2019. Available in: https://staml.gatech.edu/Research/rayleigh_benard.html. Access on 02 November 2021.

VIUNESSA R.; SCHLATTER P. European Drag Reduction and Flow Control Meeting – EDRFCM 2017. 2017. Rome, Italy. **Skin-friction control of the flow around a wing section through uniform blowing**. 3-6.

WANG Z.; WANG L.; WANG Q.; XU S.; FU S. **Control of crossflow instability over a swept wing using dielectric-barrier-discharger plasma actuators**. International Journal of Heat and Fluid Flow 73. 2018. Pg 209-222. https://doi.org/10.1016/j.ijheatfluidflow.2018.07.012

ZHANG Y., YIN Y. **Study on riblet drag reduction considering the effect of sweep angle**. Energies 2019, 12, 3386. 2019. https://doi.org/10.3390/en12173386

ZOPPINI G.; WESTERBEEK S.; RAGNI D.; KOTSONIS S. **Receptivity of crossflow instability to discrete roughness amplitude and location**. Fluid Mech (2022). 2022. vol 939, A33. https://doi.org/10.1017/jfm.2022.220

APPENDIX I

This Appendix is dedicated to summarizing the instability mechanisms that may lead other canonic flows than the boundary layer to the turbulent state. The main biography in which the present Appendix was based is Silveira Neto (2020).

Free Shear Flow

All the free shear flow types already mentioned are characterized for not being contained between any walls and, although they may present certain differences, the processes that causes the laminar to turbulent transition happens in a similar way. Summarizing, jets are formed when there is an inflectional velocity field in surplus in relation to the flow in the surrounding while wakes happen in a deficit situation. Mixture layers are perceived when there are two fluids with different characteristics or properties as different specific mass or velocities forming a shear layer. Thus, to the transition to occur, the flow must obey the situations (that are necessary but not sufficient) following the theorems of Fjortoff and Rayleigh. Thereby, the theorems combined says that, to the transition to occur, the base velocity profile must present an inflection point (for 2D flows) or a inflection line (for 3D flows) since the numerical value of the vorticity must be a maximum on the inflection point (or line). Yet, there is also necessary that at any point of the velocity profile, the multiplication of the second derivate of the velocity between this velocity and the velocity in the inflection must be less than zero. Following the theorems, with the injection of disturbances as mentioned in the last paragraph, one of the wave lengths might be select to be amplified with a maximum rate, which will be developed into instabilities.

The insertion of disturbances in a flow that respects the Fjortoff and Rayleigh theorems may cause the unbalance of the pressure field, that is coupled with the velocity one, granting that the regions of lessen speed present greater static pressure (and the opposite is also true). Therefore, pressure field gradients appear, promoting downward and upward vertical forces, causing the amplification of the disturbances into instabilities with the wave number according to the one selected to be the most amplified one. The instabilities, presenting a wave behavior, are composed of crests and valleys originating regions of compression and expansion of the path lines, which indicates regions of acceleration and deceleration. If the conditions initially imposed are maintained, the instabilities tendency is to be continuously amplified. Thus, the crests are transported into the flow direction more rapidly than the valleys initiating the processes of a furling of the shear layer resulting in the arising the disturbances of periodic natured called as the instabilities of Kelvin-Helmholtz, and they present the same wave number of the disturbances that have been selected to be the most amplified one. Then, with the amplification of the Kelvin-Helmholtz instabilities by non-linear processes they may evolve originating harmonic and sub-harmonic wave lengths by the pairing or the appearance of other wave lengths, creating, greater and smaller structures that may be called as complex whirl structures of multiples wave lengths until the full transition state is reached. Some examples of the Kelvin-Helmholtz instabilities are next shown.

Figure I.1: Kelvin-Helmholtz instabilities occurring in nature. (KOWNACKI, 2019)

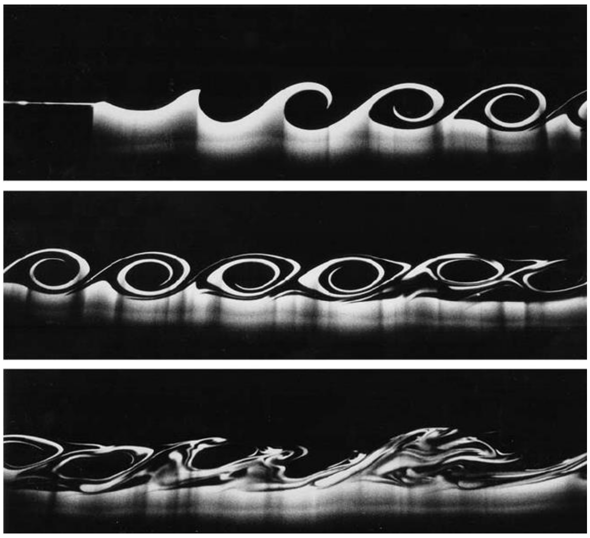

Figure II.2: Kelvin-Helmholtz instability evolution. (CUSHMAN-ROISIN and BECKERS 2006).

Rayleigh Flow

The next type of transition to be approached herein is the one that happens on the Rayleigh flow. When two plates or two surfaces distanced from each other in which a fluid fill this space and the surfaces presents different temperatures, if the upper surface has a lower temperature than the lower surface, this may present a situation that can promote the transition state to turbulence as the system shows an unstable temperature stratification. The upper parcels of the fluid will then present a higher specific mass than the lower parcel (due to the transferred thermal energy from the plates to the fluid), as so there is a tendency of the higher specific mass fluid to descend, while the other parcel tends to ascend. As always, disturbances with a large range of wave lengths must be inserted in the system to induce their amplification as the system is unstable and thus the formation of the first instabilities can occur. If the disturbances are not introduced to the system, the process remains in equilibrium and nothing else happens. Thereby, the introduction of the disturbances might create an unbalanced situation and due to the unstable characteristic of the flow, the ascending and descending movement shall begin, initiating a non-linear amplification system, that if the initial conditions are maintained, is does not returns to the equilibrium state. The pressure field becomes coupled with the velocity field, accelerating the fluid molecules and the formation of the instabilities begins. The first ones to appear (the most amplified ones) are not actually selected but must be the ones that present a wavelength that is numerically equal to the distance between the surfaces. These first instabilities are known as Rayleigh-Bérnard cells with wavelength that is numerically equal to the distance between the plates, and they may present a hexagonal shape, or a roll shape being presented on counter rotation pairs. In this case, instead of monitoring the Reynolds number, it is necessary to analyze the Rayleigh number as, from a critical value, the transition processes to turbulence may occur. This non-dimensional number depends on the temperature difference of the surfaces, the gravitational field, the fluid characteristics, and the geometry of the system. Once the primal instabilities are formed, other wave numbers may be amplified and so the processes continue until the turbulence stage is fully reached. This process is very common in nature on thermal convection flows such as in the processes that happen in the atmosphere and due to the higher-pressure change, may be very dangerous to flights.

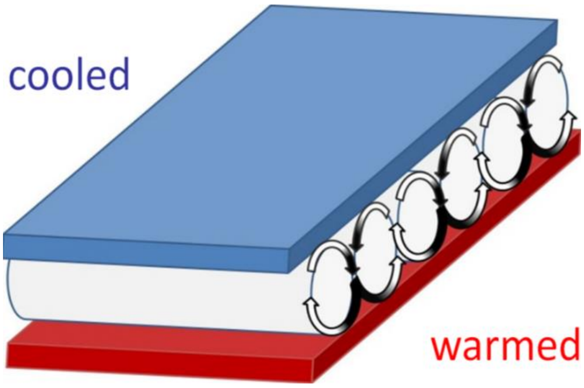

Figure III.3: Scheme of the Rayleigh-Bérnard cells fomrmation. (RANJAN, 2019)

Marangoni Effect

If instead of the system composed of a surface-fluid-surface there is a system composed of a fluid-fluid-surface, if an interface is formed between the fluid and a similar condition as described to form the unstable system as it happens to the Rayleigh flow, there might also happens a transition to turbulence due to interfacial tension effects. The instability process amplification is like the one that happens to form the Rayleigh-Bérnard cells, but this time the temperature difference also modifies the interfacial tension causing the appearing the Marangoni cells, that are hexagonally shaped.

Taylor Couette-Circular Flow

The Taylor-Couette circular flow may form a centrifugal type of instability and it is characterized by a fluid that is inserted inside a cylindrical cavity between two rotating cylinders. Also, the fluid movement depends on the border movements, represented by the cylinders due to the non-slip condition. If the rotating velocity of the internal cylinder is higher than the rotating velocity of the external one, the condition to an unstable flow is formed as it forms a decreasing distribution of the centrifugal force. Then, depending on the velocity difference between them, and if disturbances with a large range of wave lengths are inserted in the system, they might appear the first instabilities of the processes, that are the most amplified ones and that presents a wavelength of the same dimension of the distance between the cylinders (their radius difference). Thus, the instabilities of Taylor-Couette are formed, and they are toroidal shaped and are axisymmetric. If the rotation difference is increased, new instabilities may appear, and as this process continues, new and more complex structures are formed composed by various wave numbers and frequencies until the fully turbulence state is reached. Finally, in order to the transition processes to be initiated, the rotation difference between the cylinders must reach a critical valor.

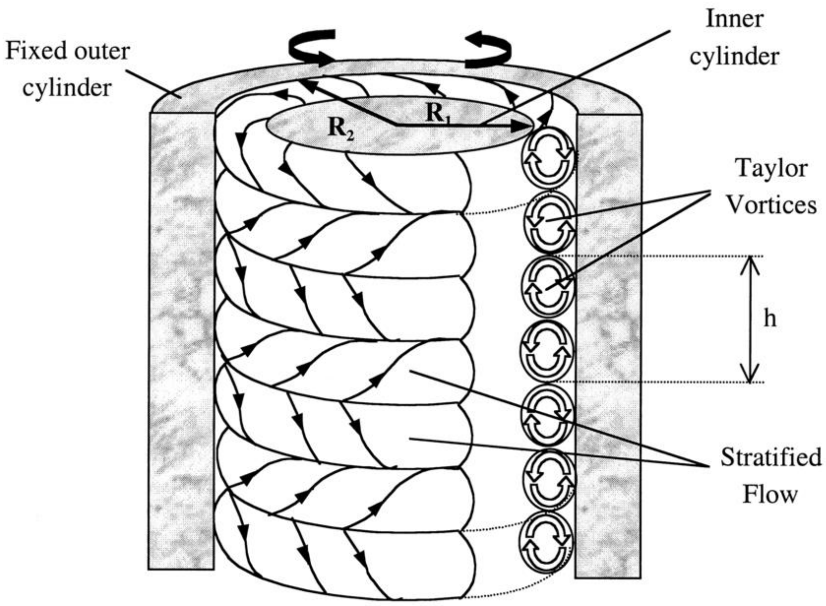

Figure IV.4: Visualization of Taylor–Couette and spiral Poiseuille flows using a snapshot FLASH spatial tagging sequence. (MOSER et al., 2000).

APPENDIX II

In this Appendix, an overview of the Orr-Sommerfeld, Equation, of the Esquire Theorem and of the e^n is presented in order to give a better understanding of the present work. All the equations and descriptions described herein have been already described, summarized and presented in MENDONÇA, M.T. DE; MEDEIROS, M.A.F. DE., 2006 which is the main reference for Appendix B and from which the mathematics equations development have been retrieved.

The Orr-Sommerfeld Equaiton

For parietal flows, where the viscosity effect must always be taken into account, and thus for the boundary layer, the solution of the Orr-Sommerfeld equations must grant the instability diagram where it is possible to, depending on the characteristics of the problem, preview the Critical Reynolds number, the wave length of the disturbances that might be amplified at maximum rate, the neutral curve where the disturbances above it shall be attenuated and also the isolines that represent the amplification rates of the disturbances. It can be applied to laminar and incompressible flows with constant physical properties. The Critical Reynolds number is, though, the Reynolds number where the first disturbances are going to start the amplification processes, resulting, for the boundary layer, on the Tollmien-Schlichting waves. Another interpretation for this parameter is that before the critical Reynolds number, all the disturbances are attenuated. The instability diagram reveals the instability wavenumber as function of the Reynolds Number and the amplification rate of the most amplified wavelength. The solution of the Orr-Sommerfeld equation results at an eigenvalue and eigenvector problem, where there only exists a particular solution for the wavenumber, frequency and Reynolds number. The Orr-Sommerfeld equation is:

$$(U-c)\left(\frac{d^2v}{dy^2}-\alpha^2v\right)-U''v=\frac{i}{\alpha Re}\left(\frac{d^4v}{dy^4}-2\alpha^2\frac{d^2v}{dy^2}+\alpha^4v\right)$$

The boundary conditions are:

- ➔ $u=0$ for $y=0$ so $v'=0$ (from continuity equation)
- ➔ $v=0$ for $y=0$
- ➔ $v\rightarrow 0$ for $y\rightarrow\infty$

Where:

- α: wave number
- c: phase velocity of the wave
- ω: frequency
- U: medium velocity profile
- u: velocity component on the parallel direction to the flow
- v: velocity component on the orthogonal direction to the flow

The medium velocity profile is supposedly known as given by the Blasius solution. Outside the boundary layer the velocity profile U is constant so that $U = U_\infty$ and $U' = U'' = 0$. So, the equation becomes:

$$v^{IV} - [2\alpha^2 + iRe(\alpha U_\infty - \omega)]v'' + [\alpha^4 + iRe\alpha^2(\alpha U_\infty - \omega)]v = 0$$

This is then, an ordinary differential equation with constant coefficients where:

- $v = C_1 e^{qy}$
- $v' = C_1 q e^{qy}$
- $v'' = C_1 q^2 e^{qy}$
- $v''' = C_1 q^3 e^{qy}$
- $v^{IV} = C_1 q^4 e^{qy}$

The substitution of this solution on the Orr-Sommerfeld Equation results in:

$$q^4 - [2\alpha^2 + iRe(\alpha U_\infty - \omega)]q^2 + [\alpha^4 + iRe\alpha^2(\alpha U_\infty - \omega)] = 0$$

Which roots are:

➔ $q = \pm\alpha$

➔ $q = \pm\lambda = \pm\sqrt{\alpha^2 + iRe(\alpha U_\infty - \omega)}$

Then, it is possible to do the arrangement:

$$v = A_2 e^{-\alpha y} + B_2 e^{-\lambda y} + C_2 e^{\alpha y} + D_2 e^{\lambda y}$$

The boundary conditions determine that the disturbances tend to zero when far from the wall ($v \to 0 \; when \; y \to \infty$). Then, $C_2 = D_2 = 0$, then:

$$v = A_2 e^{-\alpha y} + B_2 e^{-\lambda y}$$

Now, it is necessary to verify if λ is positive or negative, choosing the value that grants that v decays with increasing of y. Using this solution, that decays exponentially at the boundary layer external region, as a boundary condition to the border of the boundary layer, the Orr-Sommerfeld equation becomes:

$$v^{IV} + C_3(y)v'' + D_3(y)v = 0$$

Where:

➔ $C_3(y) = -2\alpha^2 - iRe(\alpha U_\infty - \omega)$

➔ $D_3(y) = \alpha^4 + iRe\alpha^2(\alpha U_\infty - \omega) + i\alpha ReU''$

Writing this equation on a matrix formulation composed by four first order differential equations:

$$V' = MV$$

$$V = \begin{bmatrix} v' \\ v'' \\ v''' \\ v^{IV} \end{bmatrix} \qquad M = \begin{bmatrix} 0 & 1 & 0 & 0 \\ 0 & 0 & 1 & 0 \\ 0 & 0 & 0 & 1 \\ -D_3 & 0 & -C_3 & 0 \end{bmatrix}$$

Initiating the calculus at $y = y_m$ with a linear combination of the analytic solution given by equation with the constants C_1, in which y_m is the distance from the wall until the region outside the boundary layer:

$$v = A_2 e^{(-\alpha y)} + B_2 e^{(-\lambda y)}$$

$$V_I = \begin{bmatrix} 1 \\ -\alpha \\ \alpha^2 \\ -\alpha^3 \end{bmatrix} \qquad V_{II} = \begin{bmatrix} 1 \\ -\lambda \\ \lambda^2 \\ -\lambda^3 \end{bmatrix}$$

Where V_I is known as the non-viscous solution and V_{II} is the viscous solution. Since the solutions are linearly independents, the coefficients A and B are irrelevant. At the wall, the linear combination of the viscous and non-viscous solution must satisfy the boundary conditions $v = v' = 0$, so that $V = [v, v', v'', v''', v^{IV}]$, may be given as a linear combination of the four vectors:

$$V_{y=0} = r\begin{bmatrix} 1 \\ 0 \\ 0 \\ 0 \end{bmatrix} + s\begin{bmatrix} 0 \\ 1 \\ 0 \\ 0 \end{bmatrix} + t\begin{bmatrix} 0 \\ 0 \\ 1 \\ 0 \end{bmatrix} + u\begin{bmatrix} 0 \\ 0 \\ 0 \\ 1 \end{bmatrix}$$

So that the boundary condition may be satisfied, $s = r = 0$. Then:

$$C_4 V_{I_{\eta=0}} + D_4 V_{II_{\eta=0}} = t\begin{bmatrix} 0 \\ 0 \\ 1 \\ 0 \end{bmatrix} + u\begin{bmatrix} 0 \\ 0 \\ 0 \\ 1 \end{bmatrix}$$

$$\begin{bmatrix} v_I & v_I' & v_I'' & v_I''' \\ v_{II} & v_{II}' & v_{II}'' & v_{II}''' \\ 0 & 0 & -1 & 0 \\ 0 & 0 & 0 & -1 \end{bmatrix} \begin{bmatrix} C_4 \\ D_4 \\ t \\ u \end{bmatrix} = \begin{bmatrix} 0 \\ 0 \\ 0 \\ 0 \end{bmatrix}$$

For a non-trivial solution, it is necessary that:

$$\begin{vmatrix} v_I & v_I' & v_I'' & v_I''' \\ v_{II} & v_{II}' & v_{II}'' & v_{II}''' \\ 0 & 0 & -1 & 0 \\ 0 & 0 & 0 & -1 \end{vmatrix} = 0$$

This way the Orr-Sommerfeld Equation results on a rigid equation system since both eigenvalues do not present the same magnitude order. During the integration process, it is necessary to grant that the linear independence of the solution is kept. To do so, it is necessary to use the procedure known as orthonormalization of Gramm-Schmidt. In order to grant that the desired solution is crescent on the integration direction, it is necessary to integrate from $y = y_m \; to \; y = 0$. The computational procedure to solve the Orr-Sommerfeld Equation may follow the next steps:

i) Place initial values for Re, α, ω.

ii) Integrate the Orr-Sommerfeld Equation from $y = y_m \; to \; y = 0$

iii) Verify if the boundary condition of $y = 0$ is satisfied by the calculation of the determinant.

iv) Alteration of the initial α value, from a value that is close to the previous one and then follows the integration of the Orr-Sommerfeld equation again.

v) Verification of the boundary condition of $y = 0$.

vi) If the condition is not satisfied, follows the interpolation of α between the previous initial values in order to make the determinant zero;

vii) The value found for α is now used as a new initial value.

Thereby, for the integration of the Orr-Sommerfeld equation the utilization of a finite differences scheme may be applied. It is also important to always grant that both vectors are linearly independents for each integration step so that they are always orthogonal to each other and if necessary, to do so it may be applied an orthonormalization of Gramm-Schmidt.

Finally, as before exposed, the solution for the Orr-Sommerfeld Equation shall result on the Stability Diagram where, given a Reynolds Number, and the disturbance frequency, it is possible to find the amplification rate α_i for a spatial analyzes or the frequency ω_i for a temporal analysis. The unstable region is then delimited for the neutral line. Then, it is necessary to emphasize that the Critical Reynolds number marks the point where the first disturbances start to be amplified and not the point where the flow transitions to the turbulent estate. Also, a disturbance propagating on the flow direction must follow a frequency line given by:

$$F = \frac{\omega}{Re} 10^6$$

An example of a diagram of instability is shown in the next figure.

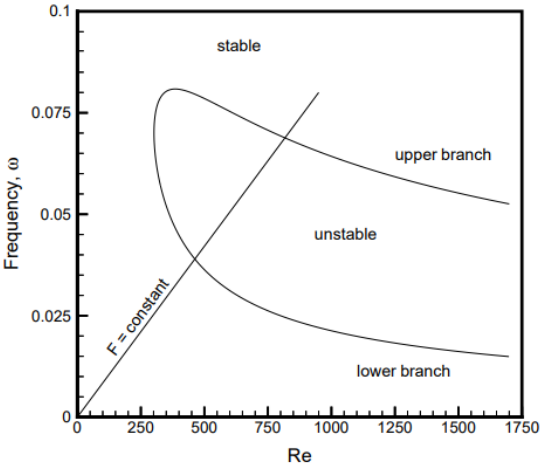

Instability Diagram for Bidimensional T-S waves. Márcio T. de Mendonça and Marcello A.F. de Medeiros (2006)

Another important equation for turbulence is the Reyleigh Equation. It can be comprehended as the consideration of the Orr-Sommerfeld Equation applied for non-viscous flows, such as the Free Shear Flows, and although may not be used for parietal flows, the Reyleigh Equation has shown great importance to the description and theorization of turbulence. As this work is focused on the boundary layer flow, the Reyleigh Equations not explained here with more details

Squire Theorem

The Orr-Sommerfeld equation may be applied also to a tridimensional concept. The equations procedures are not going to be described, but it is necessary to use the concept of the Continuity and Navier-Stokes applied to the disturbance's formulation. Then, the concept of a transversal wave number β is necessary. Also, a tridimensional wave is propagated in relation to a mean flow following an ϕ angle, so that:

$$\tan\phi = \frac{\beta}{\alpha}$$

Then, it is possible to demonstrate that the two-dimensional problem results on a higher amplification rate than the tridimensional one. The Squire Theorem shows that the lowest value for Reynolds Critical number happens for $\beta = 0$. In other words, for the tridimensional problem, the Reynolds number must be substituted for a lower Reynolds number. Thus, it can be implied that β increases the apparent viscosity.

At first, the Squire Theorem may lead to the false conclusion that the action of β on the flow is irrelevant, and only the two-dimensional effect must be considered. However, this is not true because concerning tridimensional mean flows and when non-linear effect must be considered the transversal waves play a major impact. A tridimensional stability diagram is shown on the next figure, for various transversal wave numbers, creating respectively neutral curves. For $b > 0{,}3$, the disturbances are stable for all frequency ω values.

The variable b is defined as:

$$b = \frac{\beta}{Re} 10^3$$

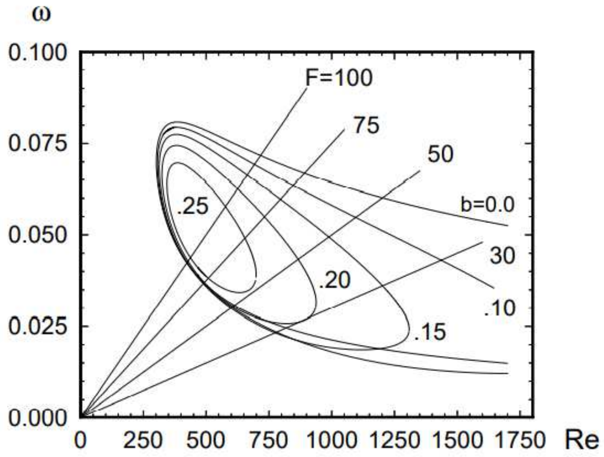

Instability Diagram for Tridimensional Waves

e^n Methodology

This methodology has for goal the determination of the actual transition point from the laminar to turbulent regime on the boundary layer. It appropriates from results determined by the application of the Linear Stability Theory and so the result given by the solution of the Orr-Sommerfeld equation and from results experimentally observed, such as the transition point. The method is considered to be semi-empirical that correlates experimental and numeric-computational data to determinate the value o N. where, the follow, formulation is applied:

$$\frac{A}{A_0} = e^N$$

Where:

- ➔ A is the amplitude at a given x position
- ➔ A_0 is the disturbance amplitude when it crosses the lower branch of the curve determined by the instability diagram.
- ➔ The formulation as presented only applies for two-dimensional flows where $\beta = 0$.

Then, considering a spatial instability N may be given as:

$$N = -\int_{x_0}^{x} \alpha_i(x)dx$$

The application of the method has shown that for two-dimensional flows with only the development of the T-S waves N may vary between 9 and 10. But it is important to have in mind that this value depends on the initial amplitude value A_0. Also, for low-speed flows where the dominant disturbance is of the level of the external disturbance Tu (mean specific kinetic turbulence divided for the mean speed square), N may be given as:

$$N = -8{,}43 - 2{,}24 \ln Tu$$

Also, it is possible to reach the value of N by comparing the value obtained by the solution of the Prandtl equations for the boundary layer for a given external pressure distribution and then analyzing the mean velocity profiles for various values of frequency. The Linear Stability Theory may also consider the gravitational, pressure gradients, curvature, compressibility, thermal energy transfer, turbulence level of the external flow, and others, the calculation of the e^N methodology must also consider these effects on the formulation. For the consideration of non-linear effects e non-parallel streamlines, the utilization of the Parabolized Stability Equations may be used. This concept though will not be herein discussed. For compressible flows, other formulations must also be used.

APPENDIX III

For the current project, a Swept Wing Model must be designed so that experimental tests for the transition point analyze, and identification aided by a wind tunnel must occur. Thus, to be possible to compare data the fairest way as possible between the experimentation of a straight wing, that is already built, and the swept wing, the latter must be projected with the same airfoil profile than for the previous case. However, some doubts and complications may occur due to the existence of the swept angle. Thereby appendix presents a summarization of the construction or design technics used by authors of other works in respect of wind tunnel scaled models of wings.

For the construction of the model, two possibilities concerning the wing profile direction have been thought. The first one is aligning the airfoil profile to the leading edge of the wing. The second one is aligning it to the airflow. It differs from the straight case because the airflow that reaches the wing, considering zero angle of attack, is always parallel aligned to the leading edge. The importance of choosing the right alignment is because depending on it, the swept angle is just going to be negligible, and thus, the problem will return to the straight case, and the purpose of this work (to determinate the transition point to a swept wing model) would not be accomplished.

Due to the mechanism interaction between the wing and the airflow, the present author believes that the cross-section of the swept wing must be aligned with the leading edge of the model. However, to resolve the doubts, some research concerning this matter was done. It is then next presented.

SERPIERI, J., 2018 projected a model of 1,25 m of wingspan, 1,27 m of chord and 45° of sweep angle, built in fiber glass. From what concerns the orientation of the wing profile, from his own words, “It must be noticed that, for the considered swept wing application, the wing sections are presented along the normal to the leading-edge direction.” Also, Serpieri has pointed out that some precautions about the attachment line instability, which may contaminate the wing boundary layer, must be taken. Thus, the airfoil NACA 66018, which was used as the wing cross section, had to be modified so that the leading edge would present around 1 % of the cord length to avoid the attachment line instability.

BORODULIN, V.I et al., 2016 have built a swept wing model of 35° of sweep angle and chord length of 800 mm. The model was equipped with contoured sidewalls in order to provide spanwise base-flow uniformity. The interpretation of the axis system used also leads to the conclusion that the airfoil profile was aligned with the wing leading edge.

BORODULIN, V.I, 2019 designed a 45° swept angle wing model with a chord of 0,7 m and a modified NACA 671-215 cross section airfoil. Interpretations of the wing design also led to the conclusion that the cross-section is aligned to the leading edge, as stringers were placed along the chordwise direction. Also, the model was designed to show a grid formed by the stringers and was thus covered with acrylic sheets.

Then the conclusion is that the model must be constructed with the cross section aligned to the leading edge.

APPENDIX IV

It is registered the table of results for the pressure distribution of the swept wing model.

Table IV.1: Pressure Distribution for $\boldsymbol{\alpha = 0}$ °

x/c	CP				
	Re = 450 000	**Re = 650 000**	**Re = 720 000**	**Re = 765 000**	**Re = 915 000**
0.969652	-0.06806180	-0.06892647	-0.08090595	-0.08071573	-0.08852475
0.939044	-0.20435270	-0.14252220	-0.14668493	-0.13728269	-0.14358679
0.908212	-0.27234903	-0.24076415	-0.22474291	-0.22440755	-0.21060906
0.877192	-0.28523837	-0.28676298	-0.28893425	-0.28315704	-0.27502482
0.846015	-0.29884054	-0.30455084	-0.31182425	-0.31202831	-0.31208857
0.814708	-0.30669634	-0.31288055	-0.32239792	-0.32144817	-0.32722090
0.783296	-0.30453600	-0.32208350	-0.32315298	-0.33460626	-0.33742039
0.751797	-0.33663568	-0.34122310	-0.34993598	-0.34889716	-0.35484965
0.720229	-0.33925428	-0.34556938	-0.35224708	-0.35339815	-0.35807017
0.688605	-0.35490042	-0.36081327	-0.36641517	-0.36647820	-0.37118751
0.656935	-0.36618950	-0.37299483	-0.37576295	-0.37880809	-0.38255276
0.625229	-0.37135396	-0.37638812	-0.38006936	-0.38159478	-0.38525614
0.593493	-0.38027903	-0.37988508	-0.38758548	-0.38401645	-0.38831581
0.561734	-0.38631636	-0.39223810	-0.39309769	-0.39657794	-0.39899787
0.529956	-0.38214842	-0.38219778	-0.38908698	-0.38276534	-0.38927229
0.498163	-0.39684895	-0.39437136	-0.39924437	-0.39661570	-0.40018438
0.466360	-0.39526324	-0.39378123	-0.39966927	-0.39661822	-0.40049916
0.434548	-0.39544509	-0.39498144	-0.40035255	-0.39862956	-0.40272690
0.402731	-0.41805962	-0.41024527	-0.41825573	-0.40833891	-0.41247150
0.370913	-0.42099827	-0.41287696	-0.42137070	-0.41094183	-0.41563323
0.339098	-0.41829966	-0.41627025	-0.42116686	-0.41722258	-0.42029106
0.307292	-0.43099987	-0.42874687	-0.43135583	-0.42991245	-0.43210427
0.277611	-0.45564381	-0.44941764	-0.45508989	-0.44818828	-0.45083419
0.250029	-0.44160520	-0.44369570	-0.44721777	-0.44572633	-0.44736114
0.224402	-0.44726429	-0.44992803	-0.45115096	-0.45230160	-0.45320029
0.200602	-0.44209255	-0.44048981	-0.44415735	-0.44051041	-0.44233144
0.178508	-0.44370736	-0.43329253	-0.44022416	-0.42822080	-0.43009274
0.158006	-0.43481139	-0.43338823	-0.43716661	-0.43233916	-0.43306248
0.138993	-0.43753910	-0.43169358	-0.43685655	-0.42860847	-0.42980909
0.121377	-0.40722152	-0.40692774	-0.41375123	-0.40727156	-0.40903478
0.105068	-0.39709626	-0.39144460	-0.39765100	-0.38790070	-0.38906819
0.089990	-0.35659524	-0.35549805	-0.36141974	-0.35289971	-0.35386377
0.076071	-0.33403163	-0.33204806	-0.33478316	-0.32939539	-0.32785567
0.063252	-0.29580733	-0.29615733	-0.30171854	-0.29289911	-0.29242294
0.051483	-0.26129999	-0.26131130	-0.26884628	-0.26215494	-0.26107727
0.040732	-0.21060097	-0.21055549	-0.21537503	-0.20871198	-0.20583535

0.030982	-0.12024469	-0.12404452	-0.12556342	-0.12417243	-0.11877731
0.022233	-0.01180553	-0.00962562	-0.01424560	-0.00731788	-0.00211358
0.014562	0.25180756	0.24229133	0.24135991	0.24300559	0.24794609
0.008124	0.53898078	0.53808181	0.53971371	0.54319490	0.54880432
0.003274	0.72541789	0.72690190	0.73012879	0.72812565	0.73062408
0.000625	0.71158294	0.71182149	0.71812539	0.71377685	0.71383305
0.000340	0.47437408	0.48304750	0.48414667	0.48124336	0.47287976
0.002183	0.17632639	0.18567800	0.19002463	0.18605348	0.17739542
0.006749	0.01006707	0.03147666	0.03224065	0.03601043	0.02726034
0.012794	-0.16765592	-0.14733900	-0.14928313	-0.14463330	-0.15514402
0.021322	-0.54440711	-0.53076889	-0.53126166	-0.53097829	-0.53495017
0.039482	-0.50361512	-0.48949117	-0.48981103	-0.48583246	-0.48336983
0.066586	-0.48316822	-0.46782355	-0.46491999	-0.44493588	-0.44996593
0.098188	-0.49501011	-0.48374929	-0.47224950	-0.46876243	-0.47801323
0.163712	-0.51914488	-0.49323136	-0.49288294	-0.48677142	-0.49258172
0.229236	-0.49851613	-0.47783994	-0.47670807	-0.47483675	-0.47950762
0.294760	-0.44346732	-0.42574435	-0.42750590	-0.42305020	-0.42689643
0.360284	-0.42190023	-0.41308829	-0.41397229	-0.41427730	-0.41945912
0.425808	-0.43524782	-0.41674475	-0.42136496	-0.41273921	-0.41852167
0.491332	-0.40866902	-0.39232582	-0.39016646	-0.38538840	-0.38919791
0.556856	-0.38500706	-0.37021959	-0.36261692	-0.36044919	-0.36340428
0.622380	-0.35244185	-0.33925332	-0.33205002	-0.32630914	-0.32977899
0.687904	-0.30817294	-0.28417514	-0.27646289	-0.27251627	-0.27487434
0.753428	-0.23005863	-0.21696326	-0.21500468	-0.21150874	-0.21243207
0.818952	-0.10795182	-0.09957773	-0.09605016	-0.09312366	-0.09194937
0.884476	-0.04035555	-0.02674360	-0.02518675	-0.02225573	-0.02130703

Table IV.2: Pressure Distribution for $\alpha = 1$ °

x/c	**CP**				
	Re = 450 000	**Re = 650 000**	**Re = 720 000**	**Re = 765 000**	**Re = 915 000**
0.969652	-0.05423565	-0.06019653	-0.07121113	-0.07402933	-0.07887990
0.939044	-0.13433753	-0.11711496	-0.12968123	-0.13203002	-0.14209442
0.908212	-0.25107959	-0.20093125	-0.19232675	-0.19283289	-0.19149143
0.877192	-0.29749828	-0.26646911	-0.25392125	-0.25311367	-0.24661063
0.846015	-0.31923646	-0.30789330	-0.30131133	-0.30132819	-0.29068762
0.814708	-0.31867287	-0.32154337	-0.32394677	-0.32235837	-0.31426457
0.783296	-0.32746329	-0.34103664	-0.33704290	-0.33973133	-0.33083482
0.751797	-0.35177785	-0.35130108	-0.35739017	-0.35859745	-0.36100590
0.720229	-0.35488121	-0.35360331	-0.36052889	-0.36275405	-0.36475887
0.688605	-0.37245473	-0.37134003	-0.37627689	-0.37799827	-0.38088882
0.656935	-0.39092852	-0.38947507	-0.38916397	-0.39185024	-0.39120298
0.625229	-0.39457351	-0.39019601	-0.39279240	-0.39457675	-0.39716612
0.593493	-0.39568603	-0.39221942	-0.39659838	-0.39817342	-0.40379145
0.561734	-0.41346449	-0.41056556	-0.41039901	-0.41243146	-0.41346076
0.529956	-0.40190740	-0.39460131	-0.40201382	-0.40155822	-0.40829848
0.498163	-0.42384319	-0.41417026	-0.41817135	-0.41813922	-0.42273656

0.466360	-0.41947360	-0.41409060	-0.41962616	-0.42023769	-0.42448910
0.434548	-0.42416524	-0.41923278	-0.42327464	-0.42337280	-0.42740307
0.402731	-0.45104885	-0.43288683	-0.44042590	-0.43832949	-0.44504114
0.370913	-0.45391800	-0.43574669	-0.44557787	-0.44409021	-0.45109269
0.339098	-0.46361600	-0.45113339	-0.45348481	-0.45380072	-0.45471738
0.307292	-0.47599286	-0.46784646	-0.46933305	-0.46930221	-0.46936175
0.277611	-0.50475751	-0.48704100	-0.49257275	-0.49264524	-0.49445722
0.250029	-0.49014097	-0.48711668	-0.48845461	-0.49015834	-0.49078226
0.224402	-0.50016834	-0.49987453	-0.49944013	-0.50190679	-0.50029209
0.200602	-0.50132478	-0.49292801	-0.49510434	-0.49523807	-0.49599828
0.178508	-0.50911979	-0.48693345	-0.49285626	-0.49067792	-0.49435322
0.158006	-0.50718750	-0.49554491	-0.49851512	-0.49777541	-0.49637791
0.138993	-0.52470247	-0.50116506	-0.50418830	-0.50152846	-0.50104268
0.121377	-0.49086557	-0.48250425	-0.48542758	-0.48430934	-0.48429735
0.105068	-0.48908700	-0.47045140	-0.47388362	-0.47172353	-0.47138992
0.089990	-0.44430050	-0.43774621	-0.44193226	-0.44121490	-0.44070746
0.076071	-0.44303427	-0.42637845	-0.42694602	-0.42713845	-0.42266376
0.063252	-0.39903093	-0.38802522	-0.39557601	-0.39398907	-0.39238174
0.051483	-0.38376297	-0.37167860	-0.37616807	-0.37513052	-0.37240521
0.040732	-0.34625913	-0.33489869	-0.33624104	-0.33447505	-0.32974274
0.030982	-0.27780949	-0.26978304	-0.26649618	-0.26519504	-0.25481515
0.022233	-0.17719907	-0.16340252	-0.16444484	-0.16257396	-0.15254725
0.014562	0.08946321	0.09026492	0.09233162	0.09230777	0.10519920
0.008124	0.42785414	0.43273945	0.43414274	0.43574423	0.44602229
0.003274	0.67398592	0.67460099	0.67861919	0.67852441	0.68493457
0.000625	0.74174023	0.74018266	0.74565777	0.74558487	0.74694432
0.000340	0.57545416	0.57894695	0.57839209	0.57645569	0.56574105
0.002183	0.31702604	0.32209304	0.32241464	0.32108717	0.30806394
0.006749	0.15447279	0.17174711	0.16910996	0.16923259	0.15442980
0.012794	-0.04302988	-0.02497401	-0.02704568	-0.02688674	-0.04130863
0.021322	-0.42693192	-0.41361661	-0.41602351	-0.41612145	-0.42620351
0.039482	-0.41112965	-0.39322316	-0.39471114	-0.39483149	-0.40103003
0.066586	-0.40950478	-0.39072178	-0.38950190	-0.38635435	-0.38154234
0.098188	-0.42836649	-0.42385317	-0.42150767	-0.41753893	-0.42560026
0.163712	-0.46913472	-0.44990660	-0.44714150	-0.44476112	-0.45393385
0.229236	-0.46523356	-0.44722597	-0.44265394	-0.44234737	-0.44759801
0.294760	-0.41265206	-0.39798694	-0.39659838	-0.39598162	-0.40260749
0.360284	-0.40424224	-0.39188484	-0.39143210	-0.39163333	-0.39800339
0.425808	-0.41417446	-0.39228713	-0.39690481	-0.39642553	-0.40679902
0.491332	-0.39706205	-0.38002318	-0.37331573	-0.37252004	-0.37974300
0.556856	-0.37735131	-0.36351723	-0.35310307	-0.35109640	-0.35683690
0.622380	-0.34458302	-0.33121831	-0.32573950	-0.32071893	-0.32736615
0.687904	-0.30773059	-0.28976623	-0.27130449	-0.27078426	-0.27477435
0.753428	-0.23762681	-0.21805059	-0.21526002	-0.21499554	-0.21836024
0.818952	-0.11068903	-0.10057317	-0.09982903	-0.09827027	-0.10126595
0.884476	-0.04690908	-0.03029543	-0.03083162	-0.02824369	-0.03142784

Table IV.3: Pressure Distribution for $\boldsymbol{\alpha = 2}$ °

x/c	CP				
	Re = 450 000	**Re = 650 000**	**Re = 720 000**	**Re = 765 000**	**Re = 915 000**
0.969652	-0.05421378	-0.06176832	-0.05687385	-0.05711029	-0.05561027
0.939044	-0.11845791	-0.13545698	-0.12279887	-0.12272863	-0.12221797
0.908212	-0.19565791	-0.17481425	-0.18097762	-0.18112496	-0.18279041
0.877192	-0.27134017	-0.23752895	-0.23413750	-0.23320456	-0.23575603
0.846015	-0.31990820	-0.28541973	-0.27666024	-0.27564642	-0.27759095
0.814708	-0.33759330	-0.31323521	-0.29759037	-0.29383003	-0.29263497
0.783296	-0.35291745	-0.31889737	-0.32267325	-0.31795716	-0.31167193
0.751797	-0.37161439	-0.36791575	-0.35559704	-0.35067555	-0.34025418
0.720229	-0.37311014	-0.36698951	-0.36540822	-0.36239869	-0.35429435
0.688605	-0.39310486	-0.38727826	-0.38460899	-0.38338889	-0.37563498
0.656935	-0.41392078	-0.39772869	-0.40071239	-0.39928789	-0.39784447
0.625229	-0.41697828	-0.40497352	-0.40713081	-0.40590469	-0.40758709
0.593493	-0.41772616	-0.41833961	-0.41066983	-0.41072104	-0.41288677
0.561734	-0.43882070	-0.42384069	-0.42704856	-0.42646621	-0.42756386
0.529956	-0.42067368	-0.42689326	-0.41971527	-0.41923665	-0.42088821
0.498163	-0.44927632	-0.44551880	-0.43967317	-0.43853734	-0.43943708
0.466360	-0.44996554	-0.44928015	-0.44257264	-0.44247868	-0.44306481
0.434548	-0.45573593	-0.45113263	-0.44799016	-0.44799605	-0.44892180
0.402731	-0.48513777	-0.48789642	-0.46847002	-0.46762204	-0.46517046
0.370913	-0.48930975	-0.49558021	-0.47719999	-0.47540636	-0.47408748
0.339098	-0.50736879	-0.49591849	-0.48930837	-0.48742958	-0.48602647
0.307292	-0.52687226	-0.51177335	-0.50889918	-0.50729513	-0.50551516
0.277611	-0.55447773	-0.54766728	-0.53587776	-0.53396912	-0.53131950
0.250029	-0.54348687	-0.53798603	-0.53409104	-0.53439528	-0.53360587
0.224402	-0.56120863	-0.55124338	-0.55024033	-0.55062209	-0.54937683
0.200602	-0.56708900	-0.55895939	-0.55048984	-0.55015306	-0.54797835
0.178508	-0.57703870	-0.57972334	-0.55467701	-0.55196361	-0.54738815
0.158006	-0.58582259	-0.57469746	-0.56559808	-0.56303869	-0.55977022
0.138993	-0.61009928	-0.59511910	-0.57639582	-0.57461810	-0.56757608
0.121377	-0.58129867	-0.57222077	-0.56362494	-0.56166439	-0.55755481
0.105068	-0.58441482	-0.57669090	-0.55803249	-0.55554939	-0.54891298
0.089990	-0.54493863	-0.54513018	-0.53372394	-0.53271839	-0.52694926
0.076071	-0.56103999	-0.54085335	-0.52810568	-0.52676225	-0.51799069
0.063252	-0.51720851	-0.51606629	-0.50332966	-0.50161133	-0.49421657
0.051483	-0.51789040	-0.50862815	-0.49606234	-0.49457089	-0.48720341
0.040732	-0.49612130	-0.48531100	-0.47163908	-0.46966709	-0.45974616
0.030982	-0.45204786	-0.42671607	-0.42141595	-0.41879788	-0.40680304
0.022233	-0.36789700	-0.35035338	-0.33385816	-0.33192709	-0.31709103
0.014562	-0.10372766	-0.08283028	-0.08049982	-0.07959583	-0.06629616
0.008124	0.27697124	0.29261623	0.30096018	0.30250450	0.31734199
0.003274	0.58711305	0.60304452	0.60387916	0.60438111	0.61225468
0.000625	0.74758406	0.75937015	0.75355623	0.75362487	0.75448058
0.000340	0.65399674	0.65256630	0.65214922	0.65195957	0.64499776

0.002183	0.44935697	0.44322735	0.44076298	0.44162132	0.43154814
0.006749	0.29100494	0.28325313	0.29174840	0.29269277	0.28424757
0.012794	0.08059478	0.07549685	0.08642783	0.08689348	0.07833900
0.021322	-0.30403414	-0.30517287	-0.30711475	-0.30647610	-0.31972702
0.039482	-0.30789084	-0.30243844	-0.29977286	-0.29836143	-0.30441646
0.066586	-0.32719634	-0.32213116	-0.31314026	-0.31025100	-0.30382453
0.098188	-0.36574135	-0.37282081	-0.37098347	-0.36961061	-0.36816490
0.163712	-0.42054903	-0.42310372	-0.40508598	-0.40198605	-0.40633573
0.229236	-0.42896632	-0.41519844	-0.40860206	-0.40748829	-0.41071982
0.294760	-0.37948176	-0.37429072	-0.36828188	-0.36687462	-0.37125609
0.360284	-0.38066224	-0.36764996	-0.36818724	-0.36781267	-0.37412400
0.425808	-0.39042864	-0.39677829	-0.37860929	-0.37752354	-0.38188833
0.491332	-0.37731879	-0.37549886	-0.36412626	-0.35966018	-0.36222136
0.556856	-0.36422360	-0.35653907	-0.35211538	-0.34762940	-0.34480443
0.622380	-0.33311337	-0.33482069	-0.32676865	-0.32384017	-0.31917490
0.687904	-0.29729591	-0.29602320	-0.27676062	-0.26930952	-0.27265128
0.753428	-0.24224627	-0.22868937	-0.22123183	-0.21922202	-0.22276127
0.818952	-0.11711613	-0.11284055	-0.10966950	-0.10819132	-0.11147669
0.884476	-0.05533559	-0.04487445	-0.04068727	-0.03973866	-0.04300839

Table IV.4: Pressure Distribution for $\alpha = 3$ °

x/c	CP				
	Re = 450 000	Re = 650 000	Re = 720 000	Re = 765 000	Re = 915 000
0.969652	-0.04617437	-0.03486454	-0.03255429	-0.03378670	-0.02825042
0.939044	-0.11376433	-0.10573481	-0.10587978	-0.10794974	-0.09912366
0.908212	-0.17837767	-0.16619818	-0.16489898	-0.16526615	-0.16347876
0.877192	-0.23257280	-0.22341814	-0.22212415	-0.22393383	-0.22045494
0.846015	-0.28246430	-0.26749233	-0.26839247	-0.26992991	-0.26695129
0.814708	-0.30930526	-0.28581153	-0.28875651	-0.28961293	-0.28831887
0.783296	-0.33616822	-0.30406266	-0.30465846	-0.30439603	-0.30883949
0.751797	-0.36940966	-0.33730950	-0.33736800	-0.33815495	-0.33792823
0.720229	-0.38104490	-0.34983863	-0.34722945	-0.34753047	-0.34940367
0.688605	-0.40701340	-0.37522924	-0.36170537	-0.35893162	-0.35766758
0.656935	-0.42820904	-0.40371109	-0.38917943	-0.38331755	-0.38137035
0.625229	-0.43267398	-0.41434623	-0.40417861	-0.39858559	-0.38928337
0.593493	-0.43677234	-0.42374008	-0.42092008	-0.41879901	-0.40595464
0.561734	-0.46123053	-0.44553892	-0.44277627	-0.43902759	-0.43171777
0.529956	-0.44649403	-0.44084200	-0.44163775	-0.44160889	-0.43413593
0.498163	-0.47785859	-0.46344569	-0.46429321	-0.46415609	-0.45948595
0.466360	-0.47986011	-0.46824272	-0.46887318	-0.47011429	-0.46761330
0.434548	-0.48841608	-0.47493773	-0.47711022	-0.47716108	-0.47522902
0.402731	-0.51794041	-0.50159767	-0.50339113	-0.50356254	-0.49548173
0.370913	-0.52371037	-0.51228087	-0.51402597	-0.51546631	-0.50720261
0.339098	-0.54808059	-0.52936678	-0.52799588	-0.52707962	-0.52224565
0.307292	-0.57319130	-0.55233885	-0.55186749	-0.55101092	-0.54581014

0.277611	-0.60698994	-0.58616230	-0.58462591	-0.58482793	-0.57654095
0.250029	-0.59777413	-0.58835660	-0.58773385	-0.58638378	-0.58297266
0.224402	-0.62350802	-0.60992320	-0.60784776	-0.60615015	-0.60343969
0.200602	-0.63377958	-0.61606964	-0.61478240	-0.61468713	-0.60715249
0.178508	-0.65194727	-0.62905925	-0.62823768	-0.62708594	-0.61336295
0.158006	-0.66778351	-0.64590090	-0.64373712	-0.64057082	-0.63193902
0.138993	-0.69671398	-0.66759964	-0.66187874	-0.65910968	-0.64645660
0.121377	-0.67455057	-0.65788146	-0.65659438	-0.65366926	-0.64436340
0.105068	-0.68636177	-0.66150125	-0.66021120	-0.65718760	-0.64250873
0.089990	-0.66160298	-0.64498394	-0.64457951	-0.64242723	-0.63044560
0.076071	-0.68422094	-0.65352489	-0.64978049	-0.64470544	-0.62956926
0.063252	-0.65168333	-0.63500148	-0.63482156	-0.63114479	-0.61503613
0.051483	-0.66732162	-0.64396688	-0.64212996	-0.63896192	-0.62209700
0.040732	-0.67040822	-0.64217300	-0.63800712	-0.63298605	-0.61421509
0.030982	-0.65459398	-0.61799166	-0.61132658	-0.60461451	-0.58412729
0.022233	-0.59335318	-0.55438500	-0.54721852	-0.54163036	-0.51515366
0.014562	-0.34013461	-0.30783861	-0.30074838	-0.29568731	-0.27165451
0.008124	0.08207719	0.11278220	0.12225037	0.12755699	0.15207419
0.003274	0.46430247	0.48538869	0.49118938	0.49607880	0.51012203
0.000625	0.72398751	0.73379302	0.73689189	0.73925870	0.74115187
0.000340	0.71037274	0.71245065	0.71198238	0.71062701	0.70566599
0.002183	0.56526584	0.55729605	0.55538657	0.55301130	0.54204377
0.006749	0.42116338	0.41817425	0.41433332	0.41061817	0.40307325
0.012794	0.20411156	0.20764962	0.20505205	0.20076782	0.19391226
0.021322	-0.17243907	-0.17381015	-0.17759812	-0.18155711	-0.19459502
0.039482	-0.19376668	-0.19335464	-0.19462997	-0.19683273	-0.20609984
0.066586	-0.23623860	-0.23253970	-0.23323338	-0.23384732	-0.23656791
0.098188	-0.29582246	-0.30598067	-0.31136884	-0.31414283	-0.31788468
0.163712	-0.36447550	-0.36348493	-0.36483056	-0.36378860	-0.35929927
0.229236	-0.38381624	-0.37144127	-0.36966928	-0.36984277	-0.37239949
0.294760	-0.34328719	-0.33554765	-0.33706899	-0.33785187	-0.34083555
0.360284	-0.35008358	-0.34183825	-0.34216935	-0.34306497	-0.34807446
0.425808	-0.36352972	-0.35978105	-0.36314577	-0.36612995	-0.36337505
0.491332	-0.35499575	-0.34976255	-0.35224355	-0.35417061	-0.34728282
0.556856	-0.34628581	-0.34043277	-0.34271848	-0.34215571	-0.33522315
0.622380	-0.31919558	-0.31858988	-0.32279720	-0.32313696	-0.31622187
0.687904	-0.28996452	-0.28694472	-0.28604820	-0.27652207	-0.27271407
0.753428	-0.24634887	-0.23271989	-0.23323625	-0.22965208	-0.23108860
0.818952	-0.12741576	-0.12365359	-0.12607994	-0.12466502	-0.12683998
0.884476	-0.06366022	-0.05784462	-0.05979834	-0.05869293	-0.06018771

Table IV.5: Pressure Distribution for $\boldsymbol{\alpha = 4}$ °

x/c	CP				
	Re = 450 000	**Re = 650 000**	**Re = 720 000**	**Re = 765 000**	**Re = 915 000**
0.969652	-0.03212748	-0.01631262	-0.01188379	-0.01339323	-0.01270215
0.939044	-0.10478716	-0.08727031	-0.08079202	-0.08439272	-0.08347180
0.908212	-0.16789603	-0.15434309	-0.14802753	-0.15081436	-0.15094604
0.877192	-0.22898453	-0.21251262	-0.20765271	-0.20939618	-0.20934757
0.846015	-0.27470356	-0.26176287	-0.25510768	-0.25832067	-0.25886503
0.814708	-0.29783123	-0.28471989	-0.28046206	-0.28383662	-0.28382626
0.783296	-0.31800550	-0.30997981	-0.30530947	-0.30871228	-0.30892076
0.751797	-0.34880321	-0.33950914	-0.33679908	-0.33880860	-0.33974585
0.720229	-0.35637040	-0.35234136	-0.34964526	-0.35218166	-0.35420301
0.688605	-0.38218699	-0.36664744	-0.36380041	-0.36533793	-0.36642055
0.656935	-0.41685646	-0.39285257	-0.38837285	-0.39016822	-0.39263832
0.625229	-0.43173369	-0.40057833	-0.39567097	-0.39743076	-0.39888123
0.593493	-0.44826396	-0.41548117	-0.40838539	-0.40977280	-0.41234838
0.561734	-0.47650499	-0.44551113	-0.43108174	-0.43033026	-0.42972882
0.529956	-0.46736559	-0.44521475	-0.42899370	-0.42428780	-0.41725859
0.498163	-0.49933879	-0.47902148	-0.46523511	-0.46346671	-0.45173562
0.466360	-0.50684720	-0.49142116	-0.48404754	-0.48343681	-0.47497300
0.434548	-0.51606007	-0.50278752	-0.49828002	-0.49820390	-0.49737788
0.402731	-0.55383722	-0.53182022	-0.52578259	-0.52626590	-0.52377565
0.370913	-0.56537902	-0.54539738	-0.54035018	-0.54037253	-0.53919685
0.339098	-0.58595736	-0.56489403	-0.55840931	-0.55980569	-0.55636787
0.307292	-0.61311107	-0.59274924	-0.58572284	-0.58654425	-0.58351506
0.277611	-0.65117475	-0.62864260	-0.62054644	-0.62086551	-0.61697440
0.250029	-0.64538549	-0.63552731	-0.62889574	-0.62996070	-0.62811539
0.224402	-0.67317102	-0.66076721	-0.65479433	-0.65551699	-0.65277547
0.200602	-0.68981148	-0.67120440	-0.66552669	-0.66638433	-0.66161800
0.178508	-0.72027859	-0.69092132	-0.68256901	-0.68162786	-0.67270880
0.158006	-0.73696313	-0.71452716	-0.70593846	-0.70464062	-0.69729099
0.138993	-0.77288156	-0.74168149	-0.72918188	-0.72686435	-0.71736451
0.121377	-0.76360257	-0.74167748	-0.73235548	-0.73123297	-0.72240799
0.105068	-0.78227074	-0.75078099	-0.73930989	-0.73924672	-0.72748782
0.089990	-0.76528498	-0.74318338	-0.73595584	-0.73552596	-0.72443127
0.076071	-0.79470150	-0.76220743	-0.74853565	-0.74727560	-0.73241187
0.063252	-0.77745125	-0.75331619	-0.74259232	-0.74183815	-0.72734589
0.051483	-0.80835182	-0.77844395	-0.76564671	-0.76481309	-0.74800788
0.040732	-0.82752693	-0.79459637	-0.78015988	-0.77910878	-0.75854656
0.030982	-0.83408026	-0.79737188	-0.77993934	-0.77799457	-0.75394617
0.022233	-0.79772103	-0.75537079	-0.73561213	-0.73340341	-0.70455851
0.014562	-0.56331457	-0.52634130	-0.50787527	-0.50591011	-0.47628147
0.008124	-0.10891606	-0.07000849	-0.05213516	-0.04752290	-0.01784255
0.003274	0.33370557	0.35955047	0.37054000	0.37426675	0.39316448
0.000625	0.67824030	0.68813380	0.69362789	0.69627647	0.70446332
0.000340	0.73699252	0.74092052	0.74165285	0.74199696	0.73743458

0.002183	0.64122721	0.63338059	0.62990969	0.63077241	0.61824133
0.006749	0.51236464	0.51001266	0.50581300	0.50544880	0.49287267
0.012794	0.30192339	0.30264254	0.29987311	0.29849027	0.28677377
0.021322	-0.06529821	-0.07118998	-0.07583973	-0.07950985	-0.09558895
0.039482	-0.10391290	-0.10699124	-0.10755562	-0.10805333	-0.11932825
0.066586	-0.16585362	-0.16211692	-0.16355179	-0.16425800	-0.17356207
0.098188	-0.24548540	-0.25271143	-0.25635077	-0.25956344	-0.26973083
0.163712	-0.32200215	-0.31748530	-0.31875714	-0.31968550	-0.32204003
0.229236	-0.34762038	-0.33471908	-0.33287505	-0.33342408	-0.33818296
0.294760	-0.32477923	-0.30642332	-0.30715978	-0.30826861	-0.31357654
0.360284	-0.32427230	-0.31955592	-0.32056449	-0.32056527	-0.32627697
0.425808	-0.34626857	-0.34007786	-0.34162249	-0.34225207	-0.34635914
0.491332	-0.34355761	-0.33562423	-0.33680481	-0.33801201	-0.33975797
0.556856	-0.33705570	-0.33064193	-0.33116509	-0.33150068	-0.33507968
0.622380	-0.31593370	-0.31454559	-0.31473287	-0.31556645	-0.32010502
0.687904	-0.28700207	-0.28918954	-0.28928969	-0.27597664	-0.27698278
0.753428	-0.24893104	-0.24164944	-0.24001593	-0.23521212	-0.23806977
0.818952	-0.14213821	-0.13939219	-0.13923427	-0.13712367	-0.13911100
0.884476	-0.08257784	-0.07603210	-0.07401806	-0.07269349	-0.07402004

Table IV.6: Pressure Distribution for $\boldsymbol{\alpha = 5}$ °

x/c	CP				
	Re = 450 000	**Re = 650 000**	**Re = 720 000**	**Re = 765 000**	**Re = 915 000**
0.969652	-0.01003835	0.00030951	0.00318767	0.00350735	0.00468451
0.939044	-0.08430307	-0.07049947	-0.06534144	-0.06430303	-0.05993308
0.908212	-0.15023061	-0.13613927	-0.12999365	-0.13233042	-0.13324605
0.877192	-0.21241118	-0.19646518	-0.19297450	-0.19176859	-0.19224292
0.846015	-0.26575596	-0.25018691	-0.24520629	-0.24499194	-0.24553788
0.814708	-0.29113414	-0.28015692	-0.27480565	-0.27501381	-0.27522373
0.783296	-0.31335929	-0.30539589	-0.29958905	-0.30371602	-0.30821051
0.751797	-0.35006636	-0.34080038	-0.33608353	-0.33699796	-0.33699987
0.720229	-0.36380768	-0.35457549	-0.35274269	-0.35308382	-0.35464280
0.688605	-0.38734537	-0.37545723	-0.37161310	-0.37035813	-0.37151188
0.656935	-0.41625054	-0.40430980	-0.39814828	-0.39933032	-0.40194221
0.625229	-0.42307721	-0.41580179	-0.41031885	-0.41111652	-0.41129569
0.593493	-0.43654722	-0.43218561	-0.42782518	-0.42630661	-0.42643571
0.561734	-0.46323060	-0.45378685	-0.44812574	-0.44930118	-0.45184815
0.529956	-0.45252499	-0.44238329	-0.43854838	-0.43824168	-0.43749233
0.498163	-0.49414491	-0.47289193	-0.46402387	-0.46355009	-0.46232440
0.466360	-0.51606943	-0.48765586	-0.47898868	-0.47732463	-0.47484579
0.434548	-0.53941647	-0.51353394	-0.50035466	-0.49865636	-0.49713695
0.402731	-0.58506200	-0.55886680	-0.54580334	-0.53455493	-0.52250621
0.370913	-0.60660522	-0.58722898	-0.57576741	-0.56691840	-0.55275172
0.339098	-0.63145545	-0.61375019	-0.60286833	-0.60022053	-0.59335255
0.307292	-0.66038262	-0.64435530	-0.63611196	-0.63429731	-0.62878177

0.277611	-0.70030870	-0.68398437	-0.67372070	-0.67076362	-0.66300013
0.250029	-0.70424632	-0.69173011	-0.68555240	-0.68443218	-0.68050659
0.224402	-0.73639250	-0.72256835	-0.71545329	-0.71374249	-0.71084192
0.200602	-0.75898429	-0.74445097	-0.73525417	-0.73119343	-0.72380033
0.178508	-0.79557403	-0.77324726	-0.75960105	-0.75213658	-0.73879008
0.158006	-0.82181746	-0.80024278	-0.78885006	-0.78314253	-0.77337117
0.138993	-0.86426597	-0.83374601	-0.81859300	-0.81299787	-0.79956955
0.121377	-0.86290210	-0.84421301	-0.83140111	-0.82684811	-0.81426738
0.105068	-0.89015743	-0.86496210	-0.84866333	-0.84227034	-0.82695978
0.089990	-0.88693841	-0.86929119	-0.85545795	-0.84980735	-0.83611635
0.076071	-0.92838235	-0.89886728	-0.87992258	-0.87393739	-0.85635372
0.063252	-0.92771508	-0.90245677	-0.88644150	-0.88098993	-0.86165143
0.051483	-0.97611767	-0.94608533	-0.92729246	-0.92109480	-0.90167015
0.040732	-1.02300241	-0.98976212	-0.96812620	-0.96075052	-0.93733083
0.030982	-1.06569290	-1.02569318	-0.99888862	-0.99279354	-0.96613056
0.022233	-1.05854360	-1.01658480	-0.98619826	-0.97820903	-0.94494662
0.014562	-0.85543750	-0.81202016	-0.78194057	-0.77431108	-0.74270593
0.008124	-0.36735667	-0.32100393	-0.29005476	-0.28163740	-0.24552579
0.003274	0.13926102	0.17429316	0.19772154	0.20266407	0.22695529
0.000625	0.57594022	0.59756735	0.61043258	0.61260475	0.62482619
0.000340	0.73535127	0.74702350	0.75093979	0.75196500	0.75186595
0.002183	0.70458362	0.70155799	0.69792687	0.69640257	0.68675779
0.006749	0.60338620	0.59877322	0.59439085	0.59494942	0.58479364
0.012794	0.40850730	0.40374304	0.39909884	0.39851783	0.38869533
0.021322	0.05815497	0.04739491	0.03822904	0.03644612	0.01977272
0.039482	0.00038863	-0.00630673	-0.01364092	-0.01420097	-0.02590128
0.066586	-0.07677248	-0.07950736	-0.08393329	-0.08483994	-0.09480610
0.098188	-0.17926777	-0.18987708	-0.19657857	-0.19796574	-0.20934864
0.163712	-0.26521334	-0.26563417	-0.26911954	-0.26823883	-0.27547592
0.229236	-0.29788747	-0.29203881	-0.29113168	-0.29108453	-0.29698288
0.294760	-0.28573733	-0.27615342	-0.27392115	-0.27280595	-0.27760226
0.360284	-0.28891235	-0.29274224	-0.29422458	-0.29418563	-0.29927677
0.425808	-0.31635833	-0.31951669	-0.32090622	-0.31976150	-0.32211377
0.491332	-0.31872676	-0.32009551	-0.32014233	-0.31914582	-0.32332808
0.556856	-0.31638033	-0.31971364	-0.31864613	-0.31799521	-0.32264405
0.622380	-0.30358492	-0.30794430	-0.30921810	-0.30865154	-0.31127997
0.687904	-0.28093447	-0.28693796	-0.28761663	-0.27539483	-0.27435834
0.753428	-0.25043079	-0.24810477	-0.24622290	-0.24174954	-0.24252715
0.818952	-0.15623602	-0.15455700	-0.15329522	-0.15070740	-0.15137608
0.884476	-0.09904896	-0.09574648	-0.09300235	-0.08927585	-0.08936674

APPENDIX V

In this Appendix it is registered the table of results for the aerodynamics balance experiments of the swept wing model.

Table V.1: Swept Wing Results for Aerodynamics Balance at Re = 450000

$Re\ x10^3$	α [°]	Dynamic Pressure [Pa]	Lift [N]	Drag [N]	Drag Endplate [N]	CL	Cd	Cd Wing
450	0	135.2	-8.54	2.27	0.524	-0.090	0.0184	0.0240
450	1	135.5	-4.82	2.23	0.525	-0.051	0.0180	0.0235
450	2	135.4	1.05	2.29	0.525	0.011	0.0186	0.0242
450	3	135.5	6.73	2.34	0.525	0.071	0.0191	0.0246
450	4	135.7	12.20	2.54	0.526	0.128	0.0212	0.0267
450	5	135.7	17.51	2.87	0.526	0.184	0.0247	0.0302
450	6	135.7	23.60	2.97	0.526	0.248	0.0257	0.0313
450	7	135.9	29.87	3.18	0.526	0.314	0.0279	0.0334
450	8	135.8	37.19	3.59	0.526	0.391	0.0322	0.0377
450	9	135.5	45.16	4.05	0.525	0.476	0.0372	0.0426
450	10	135.4	52.21	4.47	0.525	0.551	0.0416	0.0471
450	11	135.2	59.36	4.91	0.524	0.627	0.0463	0.0518
450	12	135.0	66.80	5.53	0.524	0.707	0.0530	0.0585
450	13	135.0	72.14	5.96	0.524	0.763	0.0575	0.0630
450	14	134.8	76.02	6.35	0.523	0.806	0.0618	0.0672

Table V.2: Swept Wing Aerodynamics Balance After Wind Tunnel Correction for Re = 450000

$Re\ x10^3$ Corrected	α Corrected [°]	α Corrected Adjusted [°]	CL Corrected	Cd Corrected
454.9	-0.027	-1.857	-0.085	0.0179
454.9	0.957	-0.873	-0.048	0.0175
454.9	2.020	0.190	0.010	0.0181
455.0	3.032	1.202	0.067	0.0186
455.1	3.998	2.168	0.122	0.0206
455.4	4.975	3.146	0.174	0.0239
455.5	6.078	4.248	0.235	0.0249
455.7	7.097	5.267	0.296	0.0270
456.1	8.135	6.305	0.369	0.0311
456.5	9.110	7.280	0.448	0.0358
456.9	10.183	8.354	0.517	0.0400
457.3	11.204	9.374	0.587	0.0445
457.9	12.213	10.384	0.660	0.0507
458.3	13.243	11.413	0.712	0.0550
458.7	14.264	12.434	0.750	0.0589

Table V.3: Swept Wing Results for Aerodynamics Balance at Re = 650000

$Re\ x10^3$	α [°]	Dynamic Pressure [Pa]	Lift [N]	Drag [N]	Drag Endplate [N]	CL [adm]	Cd [adm]	Cd Wing [adm]
650	0	247.3	-11.89	3.53	0.861	-0.070	0.0204	0.0154
650	1	247.2	-3.07	3.58	0.860	-0.020	0.0207	0.0157
650	2	247.6	5.13	3.70	0.862	0.030	0.0213	0.0164
650	3	247.9	14.11	3.81	0.862	0.080	0.0219	0.0170
650	4	247.8	22.67	4.09	0.862	0.130	0.0235	0.0186
650	5	248.0	30.86	4.41	0.863	0.180	0.0254	0.0204
650	6	247.8	41.24	4.82	0.862	0.240	0.0278	0.0228
650	7	247.8	50.96	5.27	0.862	0.290	0.0303	0.0254
650	8	247.8	62.63	5.99	0.862	0.360	0.0345	0.0296
650	9	247.5	73.77	6.44	0.861	0.430	0.0371	0.0322
650	10	247.5	85.55	7.10	0.861	0.490	0.0409	0.0360
650	11	247.3	96.98	7.83	0.861	0.560	0.0452	0.0403
650	12	246.9	107.34	8.65	0.859	0.620	0.0500	0.0451
650	13	246.5	118.31	9.44	0.858	0.680	0.0546	0.0497
650	14	246.1	128.83	10.54	0.857	0.750	0.0611	0.0562

Table V.4: Swept Wing Aerodynamics Balance After Wind Tunnel Correction for Re = 650000

$Re\ x10^3$ Corrected	α Corrected [°]	α Corrected Adjusted [°]	CL Corrected	Cd Corrected
656.7	-0.021	-1.419	-0.066	0.0150
656.7	0.991	-0.407	-0.019	0.0153
656.8	2.009	0.611	0.028	0.0159
656.9	3.023	1.625	0.076	0.0165
657.1	4.038	2.640	0.123	0.0181
657.3	5.053	3.654	0.170	0.0198
657.6	6.070	4.671	0.227	0.0221
657.9	7.078	5.680	0.274	0.0246
658.5	8.085	6.686	0.339	0.0286
658.8	9.117	7.719	0.405	0.0311
659.3	10.131	8.733	0.461	0.0347
659.8	11.156	9.758	0.526	0.0387
660.4	12.175	10.777	0.581	0.0433
661.0	13.189	11.790	0.636	0.0477
661.8	14.196	12.798	0.700	0.0538

Table V.5: Swept Wing Results for Aerodynamics Balance at Re = 720000

$Re\ x10^3$	α [°]	Dynamic Pressure [Pa]	Lift [N]	Drag [N]	Drag Endplate [N]	CL	Cd	Cd Wing
720	0	344.5	-9.66	4.83	1.152	-0.040	0.0200	0.0153
720	1	344.8	3.56	4.85	1.153	0.010	0.0201	0.0153
720	2	345.2	15.02	5.09	1.154	0.060	0.0210	0.0163
720	3	345.1	26.55	5.32	1.154	0.110	0.0220	0.0172
720	4	345.5	37.79	5.75	1.155	0.160	0.0238	0.0190
720	5	345.2	50.53	6.25	1.154	0.210	0.0258	0.0211
720	6	345.2	63.67	6.73	1.154	0.260	0.0278	0.0231
720	7	345.0	77.13	7.33	1.154	0.320	0.0303	0.0256
720	8	345.1	91.02	8.13	1.154	0.380	0.0336	0.0289

Table V.6: Swept Wing Aerodynamics Balance After Wind Tunnel Correction for Re = 720000

$Re\ x10^3$ Corrected	α Corrected [°]	α Corrected Adjusted [°]	CL Corrected	Cd Corrected
727.4	-0.012	-0.811	-0.038	0.0148
727.4	1.002	0.203	0.009	0.0149
727.5	2.014	1.214	0.057	0.0158
727.7	3.027	2.227	0.104	0.0168
727.9	4.042	3.243	0.152	0.0184
728.2	5.057	4.257	0.199	0.0205
728.5	6.075	5.275	0.246	0.0224
728.8	7.091	6.291	0.302	0.0248
729.3	8.103	7.303	0.358	0.0279

Table V.7: Swept Wing Results for Aerodynamics Balance at Re = 765000

$Re\ x10^3$	α [°]	Dynamic Pressure [Pa]	Lift [N]	Drag [N]	Drag Endplate [N]	CL	Cd	Cd Wing
765	0	402.4	-7.27	5.29	1.326	-0.030	0.0187	0.0141
765	1	402.9	8.05	5.57	1.327	0.030	0.0197	0.0150
765	2	402.1	23.06	5.64	1.325	0.080	0.0200	0.0153
765	3	402.7	37.23	6.19	1.327	0.130	0.0219	0.0173
765	4	402.5	50.06	6.56	1.326	0.180	0.0233	0.0186
765	5	402.3	64.16	7.08	1.326	0.230	0.0251	0.0204

Table V.8: Swept Wing Aerodynamics Balance After Wind Tunnel Correction for Re = 765000

$Re\ x10^3$ Corrected	α Corrected [°]	α Corrected Adjusted [°]	CL Corrected	Cd Corrected
772.7	-0.009	-0.511	-0.028	0.0137
772.8	1.014	0.511	0.028	0.0146
772.9	2.023	1.520	0.076	0.0149
773.1	3.037	2.534	0.123	0.0168
773.3	4.051	3.549	0.171	0.0180
773.6	5.063	4.561	0.218	0.0198

Table V.9: Swept Wing Results for Aerodynamics Balance at Re = 915000

$Re\ x10^3$	α [°]	Dynamic Pressure [Pa]	Lift [N]	Drag [N]	Drag Endplate [N]	CL	Cd	Cd Wing
915	0	585.2	-11.44	7.67	1.874	-0.030	0.0187	0.0141
915	1	584.3	7.44	7.78	1.872	0.020	0.0190	0.0144
915	2	584.1	28.58	8.26	1.871	0.070	0.0202	0.0156
915	3	584.6	48.33	8.63	1.873	0.120	0.0211	0.0165
915	4	584.9	70.15	9.40	1.873	0.170	0.0229	0.0184
915	5	585.2	92.58	10.26	1.874	0.230	0.0250	0.0205

Table V.10: Swept Wing Aerodynamics Balance After Wind Tunnel Correction for Re = 915000

$Re\ x10^3$ Corrected	α Corrected [°]	α Corrected Adjusted [°]	CL Corrected	Cd Corrected
924.2	-0.009	-0.607	-0.028	0.0138
924.2	1.003	0.405	0.019	0.0140
924.5	2.015	1.416	0.066	0.0152
924.6	3.030	2.432	0.114	0.0160
924.9	4.048	3.450	0.161	0.0178
925.3	5.064	4.465	0.218	0.0199

APPENDIX VI

Table VI.1: Laminar Airfoil 3609 Coordinates

X	Y
1.00000	0.00200
0.99269	0.00439
0.98149	0.00795
0.97003	0.01145
0.95831	0.01489
0.94637	0.01825
0.93423	0.02153
0.92191	0.02472
0.90943	0.02781
0.89678	0.03081
0.88400	0.03370
0.87109	0.03649
0.85805	0.03917
0.84489	0.04175
0.83162	0.04423
0.81824	0.04661
0.80475	0.04889
0.79117	0.05107
0.77750	0.05315
0.76374	0.05513
0.74988	0.05703
0.73593	0.05883
0.72191	0.06055
0.70782	0.06218
0.69365	0.06372
0.67941	0.06519
0.66511	0.06657
0.65075	0.06787
0.63635	0.06909
0.62189	0.07024
0.60738	0.07131
0.59282	0.07231
0.57823	0.07324
0.56361	0.07410
0.54896	0.07488
0.53429	0.07560
0.51961	0.07625
0.50490	0.07683
0.49020	0.07734
0.47552	0.07779
0.46084	0.07816
0.23636	0.07396
0.22391	0.07301
0.21181	0.07199
0.20010	0.07090
0.18880	0.06974
0.17795	0.06852
0.16756	0.06726
0.15765	0.06595
0.14822	0.06460
0.13929	0.06324
0.13085	0.06185
0.12287	0.06044
0.11535	0.05904
0.10827	0.05763
0.10160	0.05623
0.09533	0.05482
0.08941	0.05342
0.08384	0.05203
0.07859	0.05065
0.07363	0.04928
0.06895	0.04791
0.06452	0.04656
0.06033	0.04521
0.05635	0.04387
0.05259	0.04255
0.04901	0.04122
0.04561	0.03991
0.04237	0.03859
0.03929	0.03728
0.03636	0.03596
0.03356	0.03464
0.03089	0.03332
0.02835	0.03200
0.02592	0.03068
0.02360	0.02935
0.02140	0.02800
0.01929	0.02664
0.01729	0.02527
0.01539	0.02389
0.01359	0.02248
0.01188	0.02106
0.00021	-0.00179
0.00051	-0.00353
0.00092	-0.00526
0.00145	-0.00695
0.00208	-0.00862
0.00284	-0.01025
0.00373	-0.01186
0.00476	-0.01343
0.00593	-0.01498
0.00722	-0.01650
0.00862	-0.01798
0.01011	-0.01945
0.01169	-0.02088
0.01337	-0.02230
0.01514	-0.02369
0.01701	-0.02507
0.01898	-0.02643
0.02105	-0.02777
0.02322	-0.02911
0.02549	-0.03044
0.02788	-0.03175
0.03038	-0.03306
0.03299	-0.03437
0.03574	-0.03567
0.03861	-0.03697
0.04163	-0.03827
0.04480	-0.03957
0.04813	-0.04088
0.05163	-0.04219
0.05531	-0.04351
0.05919	-0.04484
0.06328	-0.04616
0.06759	-0.04751
0.07216	-0.04885
0.07698	-0.05021
0.08209	-0.05157
0.08751	-0.05294
0.09325	-0.05432
0.09934	-0.05572
0.10581	-0.05711
0.11267	-0.05851
0.26866	-0.07597
0.28196	-0.07662
0.29546	-0.07720
0.30914	-0.07769
0.32296	-0.07810
0.33692	-0.07843
0.35100	-0.07867
0.36518	-0.07885
0.37943	-0.07895
0.39377	-0.07897
0.40817	-0.07892
0.42262	-0.07880
0.43710	-0.07861
0.45161	-0.07835
0.46615	-0.07802
0.48071	-0.07763
0.49527	-0.07717
0.50982	-0.07664
0.52437	-0.07604
0.53893	-0.07537
0.55346	-0.07464
0.56797	-0.07384
0.58245	-0.07297
0.59690	-0.07203
0.61131	-0.07102
0.62568	-0.06994
0.64001	-0.06878
0.65428	-0.06755
0.66848	-0.06625
0.68263	-0.06486
0.69672	-0.06340
0.71074	-0.06185
0.72469	-0.06022
0.73856	-0.05850
0.75235	-0.05670
0.76606	-0.05480
0.77969	-0.05281
0.79323	-0.05073
0.80668	-0.04856
0.82003	-0.04628
0.83328	-0.04392

0.44617	0.07847	0.01027	0.01961	0.11995	-0.05991	0.84642	-0.04145
0.43154	0.07870	0.00876	0.01814	0.12767	-0.06130	0.85944	-0.03888
0.41694	0.07887	0.00734	0.01664	0.13586	-0.06268	0.87236	-0.03621
0.40238	0.07896	0.00603	0.01511	0.14451	-0.06405	0.88515	-0.03344
0.38788	0.07898	0.00484	0.01355	0.15364	-0.06539	0.89781	-0.03057
0.37344	0.07892	0.00380	0.01196	0.16326	-0.06670	0.91032	-0.02760
0.35908	0.07879	0.00289	0.01034	0.17335	-0.06798	0.92267	-0.02453
0.34482	0.07858	0.00212	0.00869	0.18390	-0.06920	0.93487	-0.02136
0.33066	0.07829	0.00147	0.00701	0.19490	-0.07037	0.94689	-0.01811
0.31663	0.07792	0.00094	0.00530	0.20633	-0.07149	0.95871	-0.01478
0.30273	0.07747	0.00052	0.00356	0.21814	-0.07254	0.97031	-0.01137
0.28901	0.07694	0.00021	0.00180	0.23031	-0.07351	0.98167	-0.00789
0.27549	0.07632	0.00009	0.00090	0.24281	-0.07441	0.99276	-0.00437
0.26219	0.07562	0.00000	0.00000	0.25561	-0.07523	1.00000	-0.00200

APPENDIX VII

Table VII.1: Pressure Taps Coordinates

Pressure Tap id	$\frac{x_{position}}{chord}$	$\frac{y_{position}}{chord}$	Pressure Tap id	$\frac{x_{position}}{chord}$	$\frac{y_{position}}{chord}$
1	1.0000	0.0015	**33**	0.0900	0.0531
2	0.9697	0.0111	**34**	0.0761	0.0495
3	0.9390	0.0197	**35**	0.0633	0.0457
4	0.9082	0.0276	**36**	0.0515	0.0417
5	0.8772	0.0347	**37**	0.0407	0.0374
6	0.8460	0.0410	**38**	0.0310	0.0329
7	0.8147	0.0467	**39**	0.0222	0.0280
8	0.7833	0.0518	**40**	0.0146	0.0228
9	0.7518	0.0563	**41**	0.0081	0.0170
10	0.7202	0.0602	**42**	0.0033	0.0106
11	0.6886	0.0637	**43**	0.0006	0.0037
12	0.6569	0.0668	**44**	0.0003	-0.0032
13	0.6252	0.0695	**45**	0.0022	-0.0094
14	0.5935	0.0718	**46**	0.0067	-0.0154
15	0.5617	0.0737	**47**	0.0128	-0.0213
16	0.5300	0.0753	**48**	0.0213	-0.0274
17	0.4982	0.0766	**49**	0.0395	-0.0368
18	0.4664	0.0775	**50**	0.0666	-0.0467
19	0.4345	0.0782	**51**	0.0982	-0.0550
20	0.4027	0.0785	**52**	0.1637	-0.0662
21	0.3709	0.0784	**53**	0.2292	-0.0729
22	0.3391	0.0780	**54**	0.2948	-0.0766
23	0.3073	0.0771	**55**	0.3603	-0.0782
24	0.2776	0.0759	**56**	0.4258	-0.0782
25	0.2500	0.0744	**57**	0.4913	-0.0768
26	0.2244	0.0726	**58**	0.5569	-0.0739
27	0.2006	0.0704	**59**	0.6224	-0.0696
28	0.1785	0.0681	**60**	0.6879	-0.0638
29	0.1580	0.0655	**61**	0.7534	-0.0560
30	0.1390	0.0627	**62**	0.8190	-0.0459
31	0.1214	0.0597	**63**	0.8845	-0.0330
32	0.1051	0.0565	**64**	0.9500	-0.0167

APPENDIX VIII

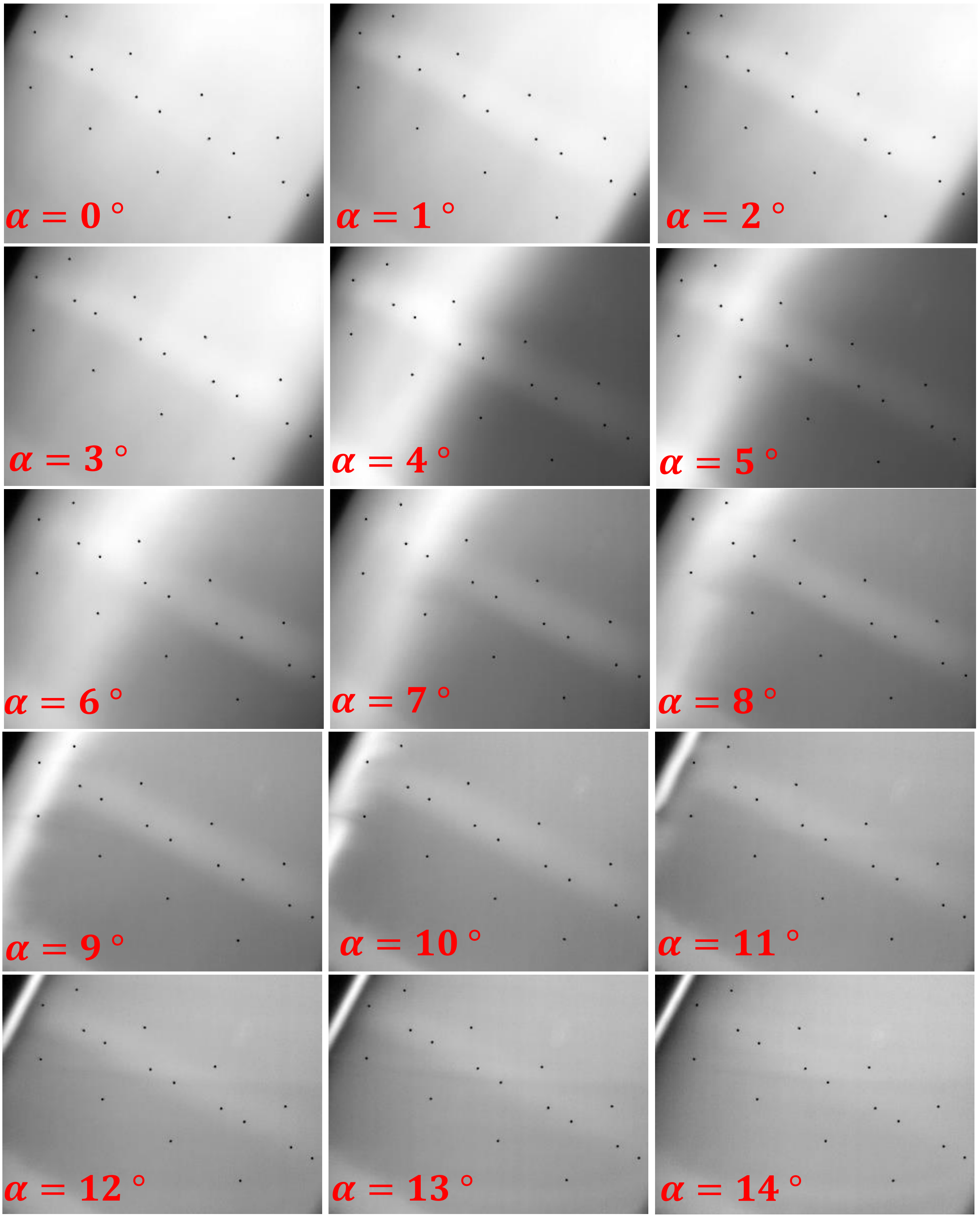

Figure VIII.1: Swept Wing Infrared Thermography for Re = 450000

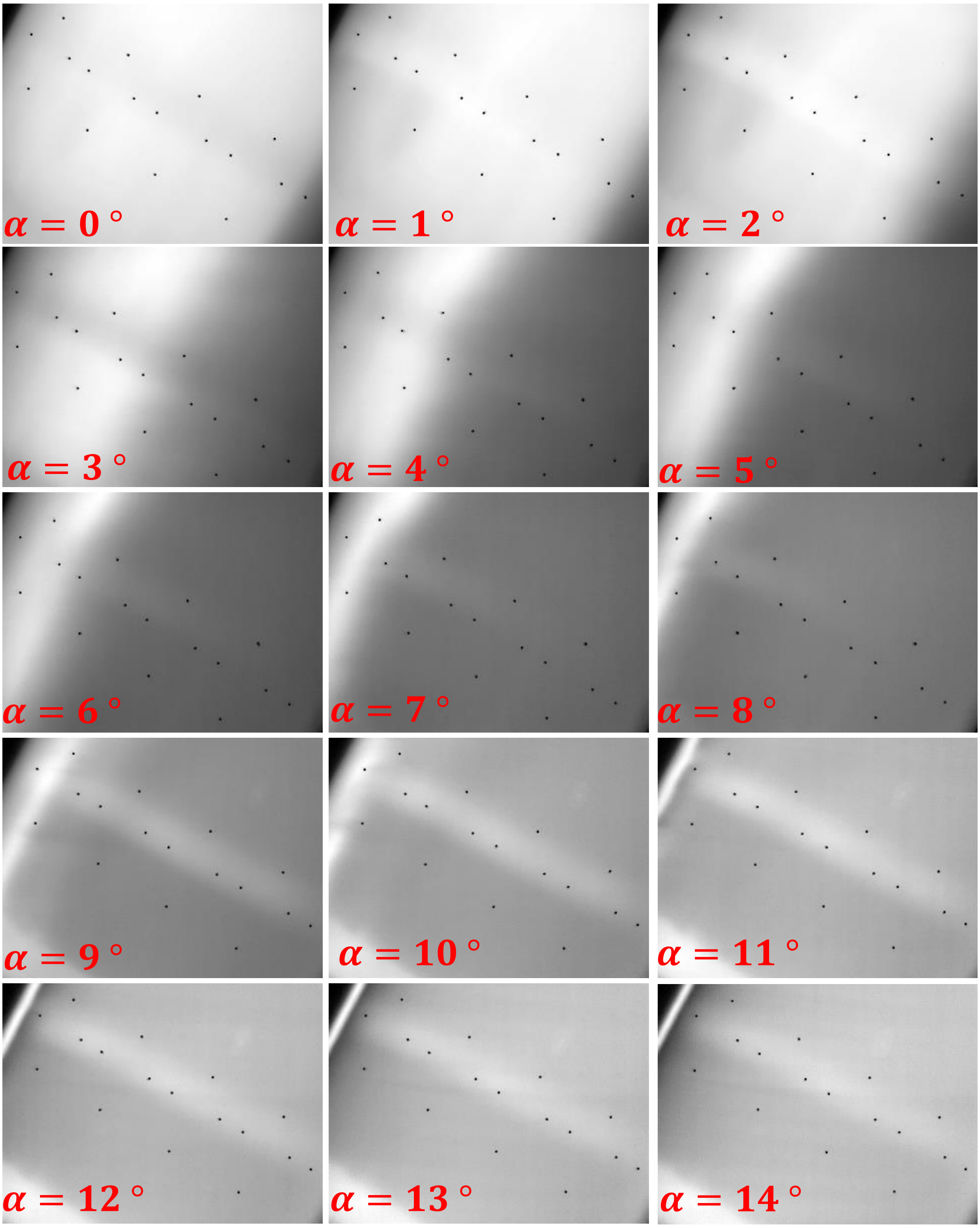

Figure VIII.2: Swept Wing Infrared Thermography for Re = 650000

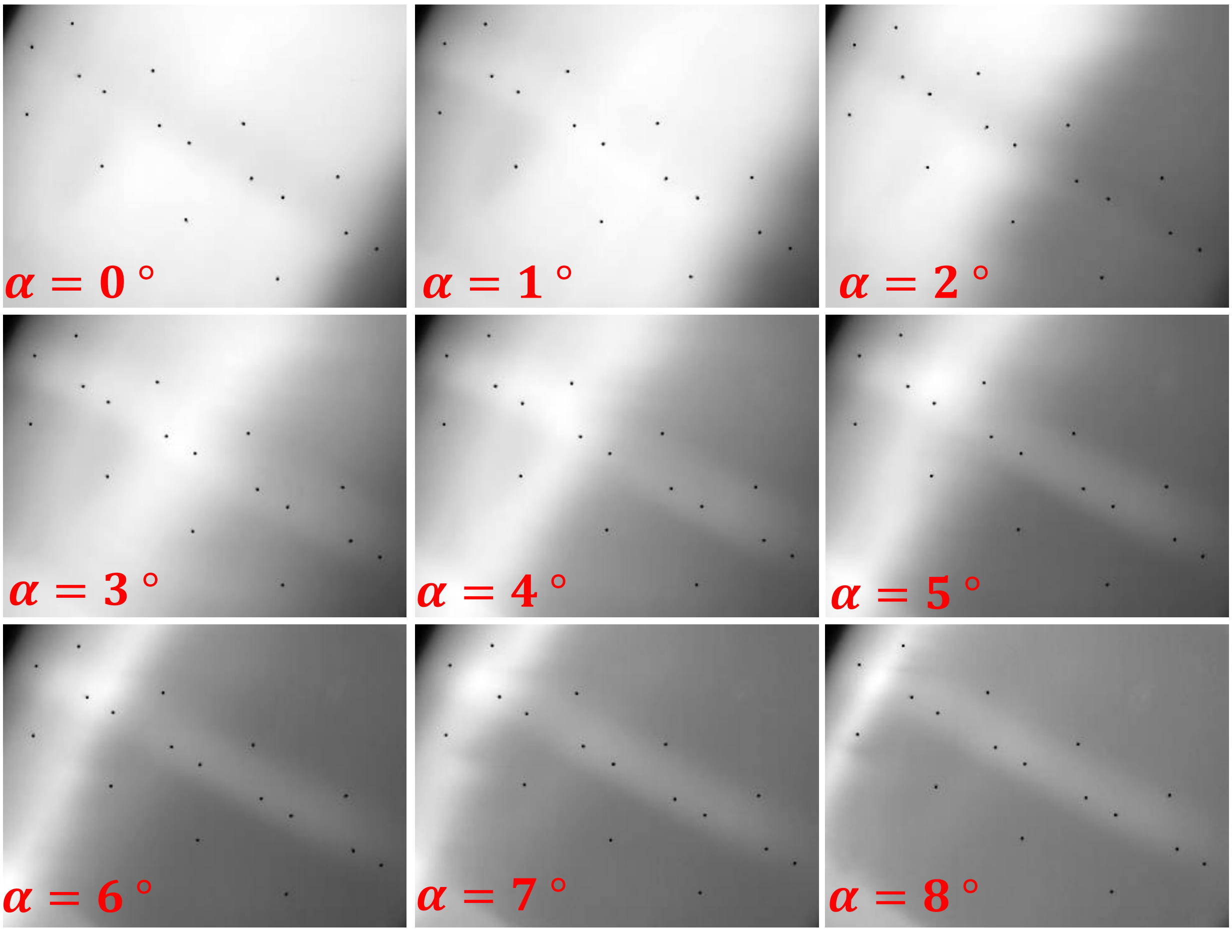

Figure VIII.3: Swept Wing Infrared Thermography for Re =720000

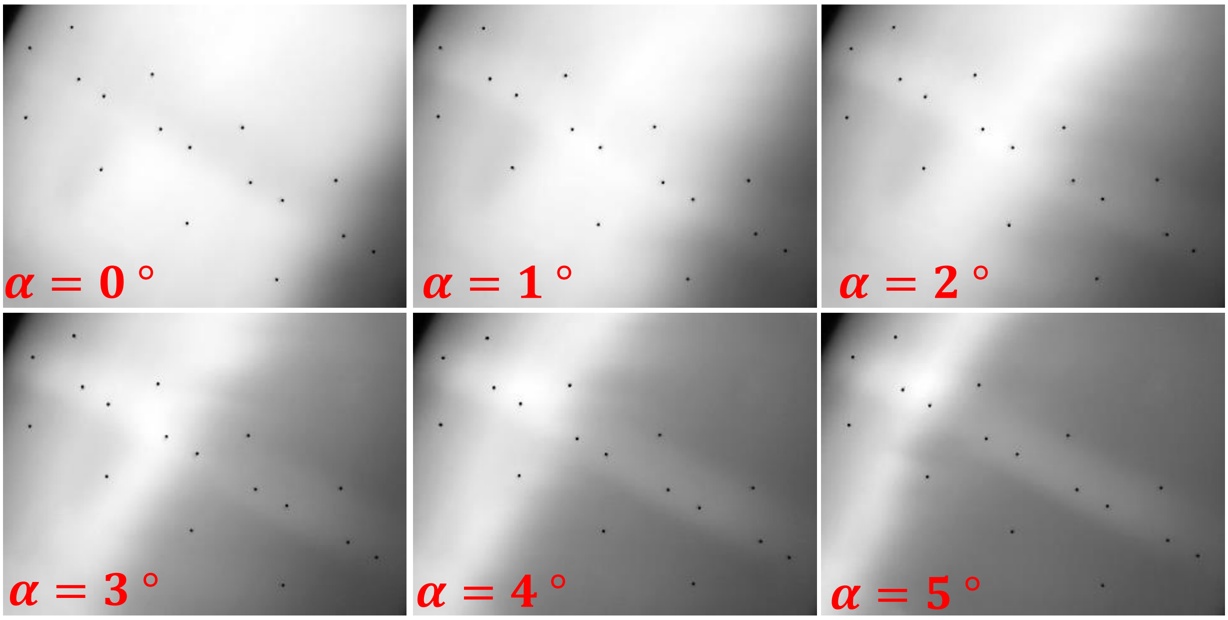

Figure VIII.4: Swept Wing Infrared Thermography for Re =765000

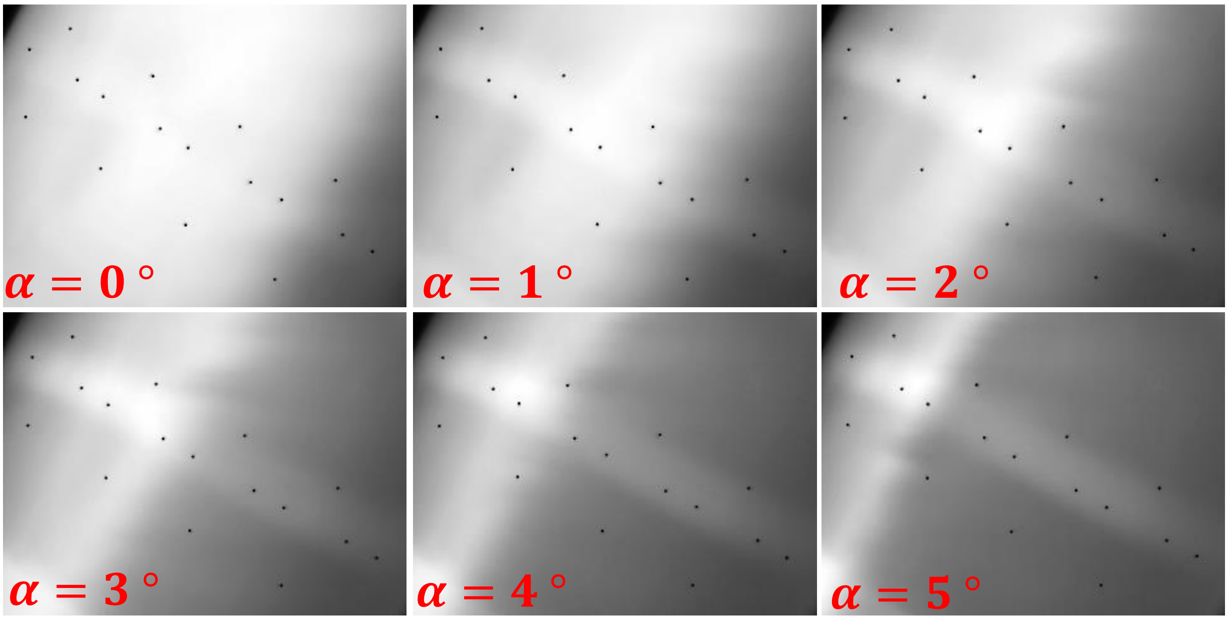

Figure VIII.5: Swept Wing Infrared Thermography for Re =915000

ANNEX I

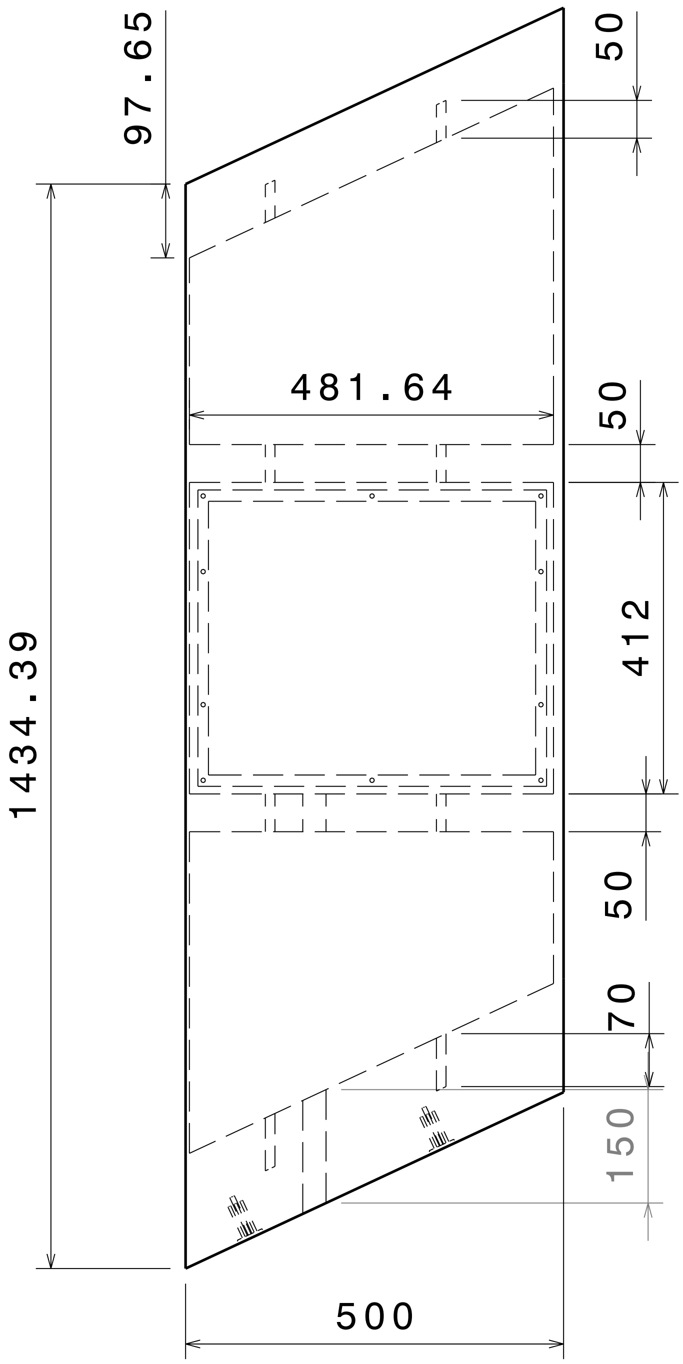

Front view
Scale: 1:10

DESIGNED BY:
Caio Botter
DATE:
10/01/2022
Dimmensions
mm

Swept Wing Model

SIZE
A4

Wing Assemble

SCALE	WEIGHT (kg)	DRAWING NUMBER	SHEET
1:10	XXX	1	1/3

This drawing is our property; it can't be reproduced or communicated without our written agreement.

I	_
H	_
G	_
F	_
E	_
D	_
C	_
B	_
A	_

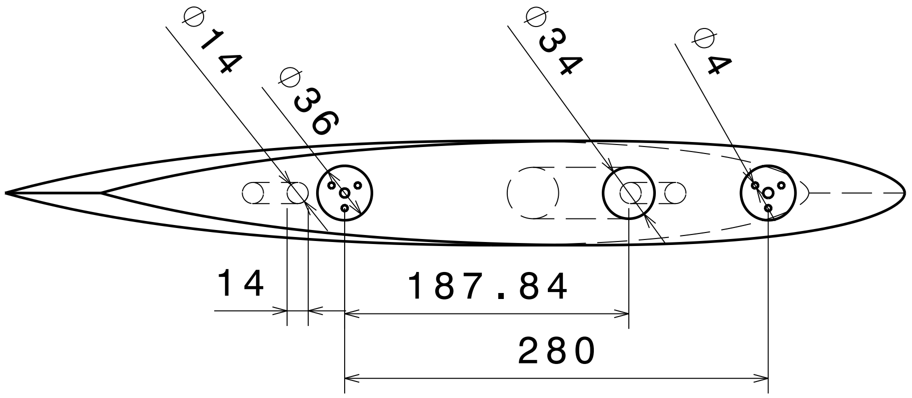

Front view
Scale: 1:5

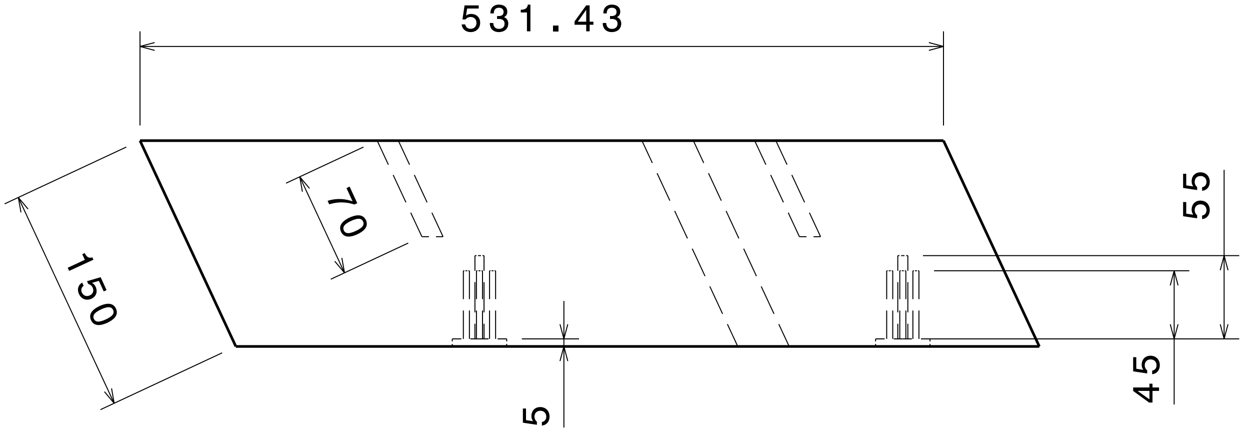

Top view
Scale: 1:5

DESIGNED BY:
Caio Botter
DATE:
10/01/2022
Dimmensions
mm

Swept Wing Model

Inferior Riblet

SIZE
A4

SCALE
1:10

WEIGHT (kg)
XXX

DRAWING NUMBER
1

SHEET
2/3

I	_
H	_
G	_
F	_
E	_
D	_
C	_
B	_
A	_

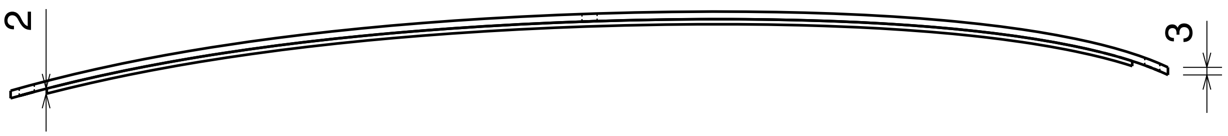

Bottom view
Scale: 1:3

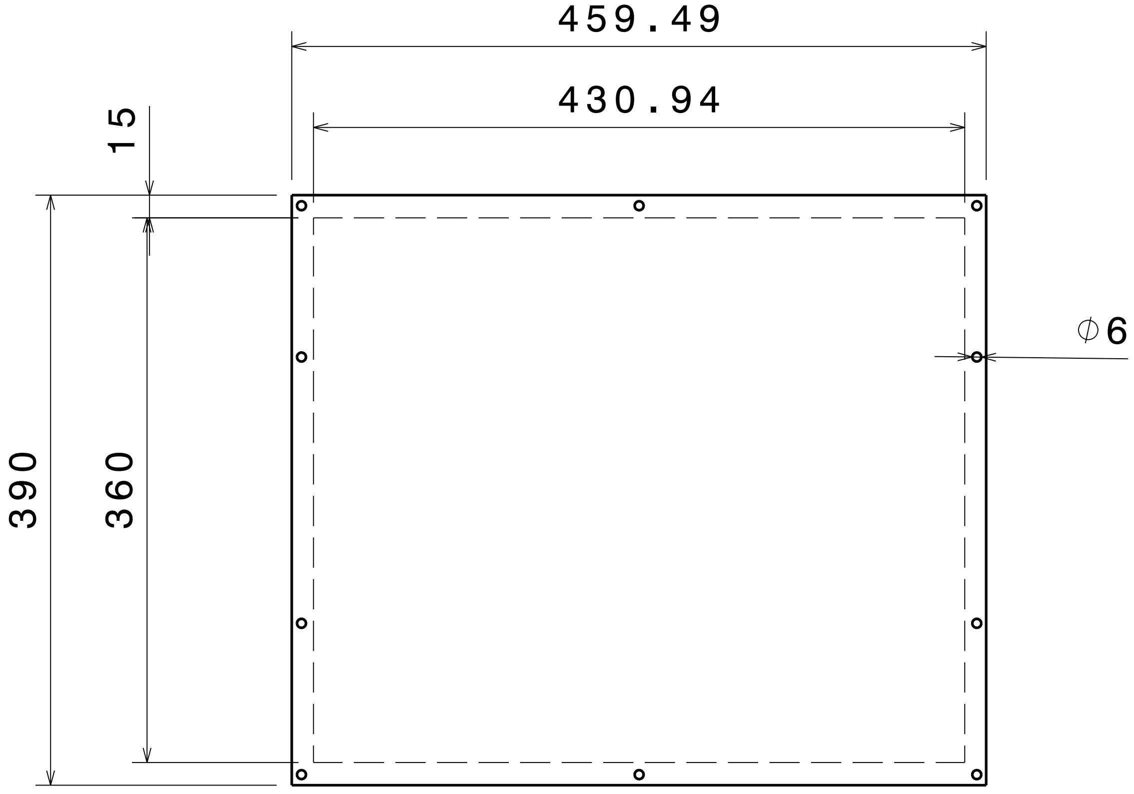

Front view
Scale: 1:5

DESIGNED BY: Caio Botter DATE: 10/01/2022	Swept Wing Model		I	_
Dimmensions mm			H	_
			G	_
			F	_
SIZE A4	Pressure Cavity Cover		E	_
			D	_
SCALE 1:10	WEIGHT (kg) XXX	DRAWING NUMBER 1	SHEET 3/3	C	_
			B	_
			A	_

ANNEX II

```
import matplotlib.pyplot as plt
import cv2 as cv
import numpy as np
import scipy.signal
import scipy
from sklearn.linear_model import LinearRegression
from sklearn.metrics import mean_squared_error, r2_score
import glob
import xlsxwriter


# Wing reference points

# Swept wing object points
objpoints = np.array([[0.00, 0.884476],
[0.00, 0.818952],
[0.09, 0.753428],
[0.00, 0.687904],
[0.00, 0.62238],
[0.09, 0.556856],
[0.00, 0.491332],
[0.00, 0.425808],
[0.09, 0.360284],
```

```
[0.00, 0.29476],

[0.00, 0.229236],

[0.09, 0.163712],

[0.00, 0.098188],

[-0.14, 0.163712],

[-0.14, 0.360284],

[-0.14, 0.556856],

[-0.14, 0.753428]])


with xlsxwriter.Workbook('C:/Users/User/Desktop/Asa UFU/IR/10_08_2022/915k/Imagens Processadas/Dados_Transicao_10_08_2022_Re=915k.xlsx') as workbook:

    worksheet = workbook.add_worksheet()


    excel_colum = 0


    folders = ['C:/Users/User/Desktop/Asa UFU/IR/10_08_2022/915k/*.png']


    files = []


    for foldersnames in folders:

        files.extend(glob.glob(foldersnames))


    for fname in files:

        # Image read in grayscale

        image = cv.imread(fname)

        img = cv.cvtColor(image, cv.COLOR_BGR2GRAY)
```

```
## Finding makers location in the image


# Initialize the mask with all white pixels (no mask)


# mask = [[0] * 320] * 240

# mask = np.asarray(mask)

# mask = mask.astype(np.uint8)

# mask[:, :] = 255


## Detect corners with mask (no mask)

corners = cv.goodFeaturesToTrack(img[:,:], 17, 0.05, 5) #, mask = mask)

corners = np.int0(corners)

corners = corners.reshape(17, 2)



## Sorting the corners

corners_tuple = []  # [tuple(corners[0])]

[corners_tuple.append(tuple(corners[i])) for i in range(len(corners))]

sorted_corners = sorted(corners_tuple, key=lambda x: x[1], reverse=True)


cornerpoints = np.array([]).reshape([0, 2])

for i in range(len(sorted_corners)):

    cornerpoints = np.vstack((cornerpoints, np.asarray(sorted_corners[i])))


for i in corners:

    x, y = i.ravel()

    cv.circle(img, (x, y), 3, 0, -1)
```

```
    ## Save image files

    # plt.imshow(img, cmap='gray'), plt.axis('off')#, plt.show()
    # # print(fname[49:78])
    # #PNG
    # fsave = 'C:/Users/User/Desktop/Asa UFU/IR/10_08_2022/915k/Imagens Processadas/Marcadores_Re=915k_' + \
    #       fname[53:81] + '.png'
    # plt.savefig(fsave)
    # #EPS
    # fsave = 'C:/Users/User/Desktop/Asa UFU/IR/10_08_2022/915k/Imagens Processadas/Marcadores_Re=915k_' + \
    #       fname[53:81] + '.eps'
    # plt.savefig(fsave)
    plt.close()

    ## Marker sorting
    cornerpoints = cornerpoints[:, [1, 0]]
    imgpoints = np.array([]).reshape([0, 2])
    imgpoints = np.vstack((imgpoints, cornerpoints[np.where(cornerpoints[:,1] == max(cornerpoints[:,1]))[0][0],:]))
    cornerpoints = np.delete(cornerpoints, np.where(cornerpoints[:,1] == max(cornerpoints[:,1]))[0][0], 0)

    while len(cornerpoints) > 0:
        dist = np.sqrt(np.sum(np.power(cornerpoints - imgpoints[-1] * np.ones((len(cornerpoints), 2)), \
                              np.array([2, 2]) * np.ones((len(cornerpoints), 2))), axis=1))
```

```
        index = np.where(dist == min(dist))
        imgpoints = np.vstack((imgpoints, cornerpoints[index[0]]))
        cornerpoints = np.delete(cornerpoints, index[0], 0)

    ## Linear regression from image and object points (for low distortion only)

    modelimgtoobj = LinearRegression().fit(imgpoints, objpoints) # Img pts to obj pts
    modelobjtoimg = LinearRegression().fit(objpoints, imgpoints)  # Obj pts to img pts

    img = cv.cvtColor(image, cv.COLOR_BGR2GRAY)

    # Image size
    n_row, n_col = img.shape

    ## Trasition points detection

    trans_pts = np.array([]).reshape([0, 2])

    for i in range(n_row):
        gx = np.gradient(img[i, :])
        gx_2 = np.gradient(scipy.signal.savgol_filter(img[i, :], 50, 3)) #3D
        gx_smooth = scipy.signal.savgol_filter(np.gradient(scipy.signal.savgol_filter(img[i, :], 50, 3)),
10,
                                    4)
        grad = gx_2[19:]
        gx_min = np.where(grad == np.min(grad))
```

```
        ## Detection check (keep commented)
        # if i == 100:
        #     f = plt.figure()
        #     f.add_subplot(1, 3, 1)
        #     plt.imshow(img, cmap='gray')
        #     f.add_subplot(1, 3, 2)
        #     plt.plot(np.linspace(1, n_col, n_col, dtype="int"), img[i, :], np.linspace(1, n_col, n_col, dtype="int"),
        #             scipy.signal.savgol_filter(img[i, :], 50, 3))
        #     f.add_subplot(1, 3, 3)
        #     plt.plot(np.linspace(1, n_col, n_col, dtype="int"), gx, np.linspace(1, n_col, n_col, dtype="int"), gx_2,
        #             np.linspace(1, n_col, n_col, dtype="int"), gx_smooth)
        #     plt.show(block=True)

        trans_pts = np.vstack((trans_pts, np.concatenate((np.array([i]), gx_min[0] + 19))))

    ## Image edges removal

    # Front
    # if len(trans_pts[np.where(trans_pts[:,1] <= 19),:][0]) > 1:
    #     trans_pts = np.delete(trans_pts, np.linspace(int(trans_pts[np.where(trans_pts[:,1] <= 19),:][0][0][0]),len(trans_pts[:,1])-1,
    #                                          len(trans_pts[:,1])-int(trans_pts[np.where(trans_pts[:,1] <= 19),:][0][0][0])).astype(int), 0)
    # Back
    # if len(trans_pts[np.where(trans_pts[:,1] >= 315),:][0]) > 1:
```

```
    #    trans_pts = np.delete(trans_pts, np.linspace(0,int(trans_pts[np.where(trans_pts[:,1] >= 315),:][0][-1][0]),
    #      int(trans_pts[np.where(trans_pts[:,1] >= 315),:][0][-1][0])).astype(int),0)

    ## Outiliers removal
    trans_pts_coord = modelimgtoobj.predict(trans_pts)
    trans_pts_nooutliers_coord = np.array([]).reshape([0, 2])
    for i in range(len(trans_pts)):
        if abs(trans_pts_coord[i, 1] - np.mean(trans_pts_coord[:, 1])) <= 0.5 * np.std(trans_pts_coord[:, 1]):
            trans_pts_nooutliers_coord = np.vstack((trans_pts_nooutliers_coord, trans_pts_coord[i]))
    # print(trans_pts_coord)
    # print(trans_pts_nooutliers_coord)
    trans_pts_nooutliers = modelobjtoimg.predict(trans_pts_nooutliers_coord)

    # Plot and save transition line images
    # trans_pts_nooutliers_coord = modelobjtoimg.predict(trans_pts_nooutliers_coord )
    plt.plot(trans_pts_nooutliers[:, 1], trans_pts_nooutliers[:, 0])
    # plt.plot(trans_pts[:, 1], trans_pts[:, 0])
    plt.imshow(image), plt.axis('off')#, plt.show()

    #PNG
    # fsave = 'C:/Users/User/Desktop/Asa UFU/IR/10_08_2022/915k/Imagens Processadas/TransLine_Re=915k_' + \
    #       fname[53:81] + '.png'
    # plt.savefig(fsave)
    # #EPS
    # fsave = 'C:/Users/User/Desktop/Asa UFU/IR/10_08_2022/915k/Imagens Processadas/TransLine_Re=915k_' + \
```

```
#       fname[53:81] + '.eps'

# plt.savefig(fsave)

plt.close()


## Save transition line data to Excel

dados_trans = trans_pts_nooutliers_coord.tolist()

worksheet.write_row(0, excel_colum, [fname])

for row_num, data in enumerate(dados_trans):

   worksheet.write_row(row_num+1, excel_colum, data)


excel_colum = excel_colum + 3
```

ANNEX III

FLIR A300

Safety: the infrared eye that never sleeps

The FLIR A300 camera offers an affordable and accurate temperature measurement solution for anyone who needs to solve problems that do not call for the highest speed or reaction and who uses a PC. Due to to its composite video output, it is also an excellent choice for thermal image automation applications, where you can utilize its unique properties such as looking through steam.

Key Features:

- MPEG-4 streaming
- PoE (Power over Ethernet)
- Built-in web server
- General purpose I/O
- 100 Mbps Ethernet (100 m cable, wireless, fiber, etc.)
- Synchronization through SNTP
- Composite video output
- Multi-camera utility software: FLIR IP Config and FLIR IR Monitor included
- Open and well-described TCP/IP protocol for control and set-up
- 16-bit 320 × 240 images @ 3 Hz, radiometric
- Lenses: 25° included, 15° and 45° optional

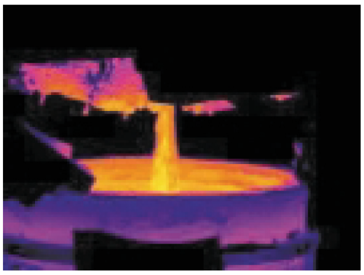

Process monitoring

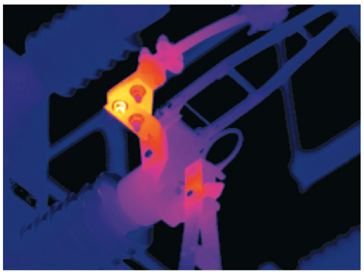

Sub-station monitoring

Typical applications:

- Fire prevention, critical vessel monitoring, and power utility asset management
- Volume-oriented industrial control (multi-camera installation is possible)

IR Automation for Oil & Gas industry

- Oil refineries and exploration, petrochemical plants:
- Natural gas processing, transport and storage
- Fire prevention in storage areas
- Refractory lining monitoring
- Flare detection
- Process quality control

IR Automation for Power Generation and Distribution

- Fire prevention on coal piles
- Fire prevention in wood storage areas
- Fire prevention in waste storage areas
- Sub-station monitoring
- Critical equipment monitoring

FLIR A300 Technical Specifications

Imaging and optical data

Field of view (FOV)	25° x 18.8°
Minimum focus distance	0.4m
Focal Length	18mm
Spatial resolution	1.36mrad
Lens identification	Automation
F-number	1.3
Thermal sensitivity/ NETD	<0.05°C @ + 30°C/ 50mK
Image frequency	30Hz
Focus	Automatic or manual (built in motor)
Zoom	1-8x continuous, digital, interpolating zooming on images

Detector data

Detector type	Focal Plane Array (FPA), uncooled microbolometer
Spectral range	7.5-13µm
IR resolution	320 x 240pixels
Detector pitch	25µm
Detector time constant	Typical 12ms

Measurement

Object temperature range	-20°C to + 120°C 0 to +350°C
Accuracy	±2°C or ±2% of reading

Set-up

Color palettes	Color palettes (BW, BW inv, Iron, Rain)
Set-up commands	Date/ time, Temperature°C

Storage of images

Image storage type	Built-in memory for image storage
File format	Standard JPEG, 16-bit measurement data included

Ethernet

Ethernet	Control and image
Ethernet, type	100Mbps
Ethernet, standard	IEEE 802.3
Ethernet, connector type	RJ-45
Ethernet, communication	TCP/IP socket-based FLIR proprietary
Ethernet, video streaming	MPEG-4, ISO.IEC 14496-1 MPEG-4 ASP@ L5
Ethernet, image streaming	16-bit 320 x 240 pixels @ 3 Hz
Ethernet, power	Power over Ethernet, PoE Ieee 802.3af class 0
Ethernet, protocols	TCP, UDP, SNTP, RTSP, RTP, HTTP, ICMP,
	IGMP, ftp, SMTP, SMB (CIFS), DHCP, MDNS (Bonjour), uPnP

Digital input/output

Digital input, purpose	Image tag (start/ stop/ general), Input ext. device (programmatically read)
Digital input	2 opto-isolated, 10-30 VDC
Digital ouput, purpose	Output to ext. device (programmatically set)
Digital ouput	2 opto-isolated, 10-30 VDC, max 100mA
Digital I/O, isolation voltage	500VRMS
Digital I/O, supply voltage	12/24 VDC, max 200 mA
Digital I/O, connector voltage	6-pole jackable screw terminal

Composite video

Video out	Composite video output, PAL and NTSC compatible
Video, standard	CVBS (ITU-R-BT.470 PAL/ SMPTE 170M NTSC)
Video, connector type	Standard BNC connector

Power system

External power operation	12/24 VDC, 24W absolute max
External power, connector type	2-pole jackable screw terminal
Voltage	Allowed range 10-30 VDC

Environmental data

Operating temperature range	-15°C to +50°C
Storage temperature range	-40°C to +70°C
Humidity (operating and storage)	IEC 60068-2-30/24 h 95% relative humidity +25°C to +40°C
EMC	- EN 61000-6-2:2001 (Immunity) - EN 61000-6-3:2001 (Emission) - FCC 47 CFR Part 15 Class B (Emission)
Encapsulation	IP 40 (IEC 60529)
Bump	25g (IEC 60068-2-29)
Vibration	2g (IEC 60068-2-6)

Physical data

Weight	0.7kg
Camera size (L x W x H)	170 x 70 x 70mm
Tripod mounting	UNC1/4"-20 (on three sides)
Base mounting	2 x M4 thread mounting holes (on three sides)
Housing materia	Aluminium

Scope of delivery

Packaging, contents	Hard transport case or cardboard box Infrared camera with lens Calibration certificate Ethernet™ cable Mains cable Power cable, pig-tailed Power supply Printed Getting Started Guide Printed Important Information Guide User documentation CD-ROM Utility CD-ROM Warranty extension card or Registration card

Supplies & Accessories

IR lens f = 30 mm, 15° incl. case
IR lens f = 10 mm, 45° incl. case
Close-up 4× (100 µm) incl. case
Close-up 2× (50 µm) incl. case
Lens 76 mm (6°) with case and mounting support for A/SC3XX
Lens 4 mm (90°) with case and mounting support for A/SC3XX
Close-up 1× (25 µm) incl. case and mounting support for A/SC3XX
High temp. option +1200°C/+2192°F for FLIR T/B2XX to T/B4XX and A/ ••• SC3XX Series
Power supply for A/SC3XX and A/SC6XX
Power cord EU
Power cord US
Power cord UK
Video cable, 3.0 m/9.8 ft.
Ethernet cable CAT-6, 2m/6.6 ft.
Power cable, pigtailed
Hard transport case for A/SC3XX and A/SC6XX series
Delivery Box for A/SC3XX
ThermoVision™ System Developers Kit Ver. 2.6
ITC Advanced General Thermography Course – attendance, 1 pers.
ITC Advanced General Thermography Course – group of 10 pers.
ITC Level 1 Thermography Course – attendance, 1 pers.
ITC Level 1 Thermography Course – group of 10 pers.
ITC Level 2 Thermography Course – attendance, 1 pers.
ITC Level 2 Thermography Course – group of 10 pers.

Accessories

Asia Pacific Headquarter
Hong Kong
FLIR Systems Co Ltd.
Room 1613 – 16, Tower 2
Grand Central Plaza
138 Shatin Rural Committee
Road, N.T, Hong Kong
Tel: +852 2792 8955
Fax: +852 2792 8952
Email: flir@flir.com.hk

China Head Office - Shanghai
FLIR Systems (Shanghai) Co., Ltd
Tel: +86 21 5169 7628
Fax: +86 21 5466 0289
e-mail: info@flir.cn

Japan Office - Tokyo
FLIR Systems Japan K.K.
Tel: +81 3 6277 5681
Fax: +81 3 6277 5682
e-mail: info@flir.jp

Korea Office - Seoul
FLIR Systems Korea Co., Ltd
Tel: +82 2 565 2714
Fax: +82 2 565 2718
e-mail: sales@flirkorea.com

Taiwan Representative Office
Tel: +886 2 27579662
Fax: +886 2 27576723
e-Mail: flir@flir.com.hk

India Representative Office
Tel: +91 11 4606 7100
Fax: +91 11 4606 7110
e-mail: flir@flir.com.hk

www.flir.com/thg

Model ZOC 33

Electronic Pressure Scanning Module

Scanivalve

Data Sheet No. G480

Features

- 0 - 50 psid pressure range
- Field replaceable pressure sensors
- 45kHz scan rates
- Duplex 128 pressure inputs with 64 pressure sensors
- On board sensor excitation

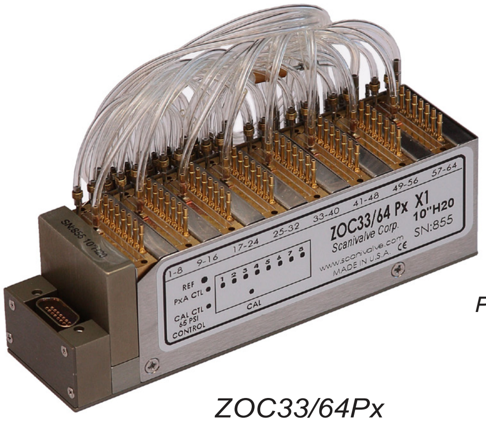

Patented

ZOC33/64Px
Pressure Scanner (shown)

General Description

The Model ZOC33 electronic pressure scanning module is extremely compact and accepts up to 64 pneumatic inputs and converts them to high level electronic signals. Each ZOC33 module incorporates 64 individual silicon pressure sensors, calibration valving, a high speed multiplexer (45kHz), and an instrumentation amplifier. An integral "duplexing" valve is available to allow the ZOC33's 64 sensors to service up to 128 input pressures.

The integral calibration valve has 4 modes of operation: operate, calibrate, purge, and leak test. Each group of 8 pressure sensors has its own calibration valving and multiplexer which allows the ZOC33 module to incorporate multiple pressure ranges and easy sensor replacement. This calibration valve allows the ZOC sensors to be automatically calibrated on-line.

The ZOC33's extremely compact design (approximately .1 cu. in. per channel) permits installation within the very confined spaces typically available in wind tunnel models.

Three versions are available:

ZOC33/64Px - 64 Px inputs each with its own dedicated sensors.

ZOC33/64PxX2 - 128 Px inputs duplexed* between 64 sensors.

ZOC33/64Px - Valveless (no calibration valve).

Applications

The ZOC33 electronic pressure scanning module is specifically designed for use in wind tunnel and flight tests where operational conditions are very space constrained and pressures do not exceed 50 psi. It is ideal for use inside small supersonic wind tunnel models.

It may be mounted in any position so the pressure sensors may be close coupled to the pressure sources to be measured. A removable header allows for easy installation and removal without breaking the pneumatic lines. When the ZOC33 is used for flight test, it must be installed in a thermostatically controlled heater jacket.

The ZOC33 module is designed to be used in conjunction with our Model ERAD4000 Remote A/D or our Model DSM4000 Digital Service Module. Each ZOC33 pressure scanner incorporates an embedded RTD to monitor the temperature of the pressure sensors. The ERAD4000 communicates via Ethernet. The DSM4000 communicates via Ethernet, RS-232, or ARINC 429.

*Duplexing shares 2Px inputs with one pressure sensor. This doubles the usefulness of a ZOC33 module without increasing the installation volume.

Px = Pressure Input

Specifications

Inputs (Px): 128 or 64 .042 inch (1.067mm) O.D. tubulations

Full Scale Ranges: ±10, ±20 inch H_2O, ±1, ±2.5, ±5, ±15, 50 psid (2.5, 5, 7, 17, 35,100, 350 kPa)

Accuracy:[1]

10 to 20 in.H_2O	±0.15% F.S.
1 psid	±0.12% F.S.
2.5 psid	±0.10% F.S.
5 to 50 psid	±0.08% F.S.

Sensor Addressing: 6 bit binary, CMOS level

Full Scale Output: Standard: ±2.5Vdc
Optional: ±5Vdc, ±10Vdc

Resolution: Infinite

Scan Rate: 45kHz

Operating Temperature: 0° to 60°C

Temperature Sensitivity:

Range	Zero	Span
10 inch H_2O	0.25% FS/°C	0.10% FS/°C
20 inch H_2O	0.20% FS/°C	0.08% FS/°C
1 to 50 psid	0.10% FS/°C	0.05% FS/°C

Connector Type: Cannon 15 pin MDM 15SL2P

Power Requirements: ± 15Vdc @ 110mA

Control Pressure Requirements: 65 psi instrument grade air

Overpressure Capability: (With no damage) 10 inch H_2O, 20 inch H_2O, 1 psid = 10 psi (70kPa)
2.5-50 psid = 400% or 75 psi (517kPa) (whichever is less)

Maximum Reference Pressure: 50 psig (345kPa)

Media Compatibility: Gases compatible with silicon, silicone, aluminum, and Buna-N

Weight:

ZOC33/64Px:	11 ozs. (312 gm)
ZOC33/64PxX2:	13 ozs. (369 gm)

Ordering Information

ZOC33 / 64Px - 1 psid ______

Model

Inputs
64Px, for 64 Inputs
64PxX2, for 128 inputs Duplexed

Pressure Ranges

Write "Valveless" here for this option only.

[1] Note: Accuracies are following a calibration with Scanivalve DSM or RAD data systems.

† 10 inch H_2O = 25.4 cm H_2O = .36127 psi

‡ 20 inch H_2O = 50.8 cm H_2O = .72254 psi

Dimensions Inches (mm)

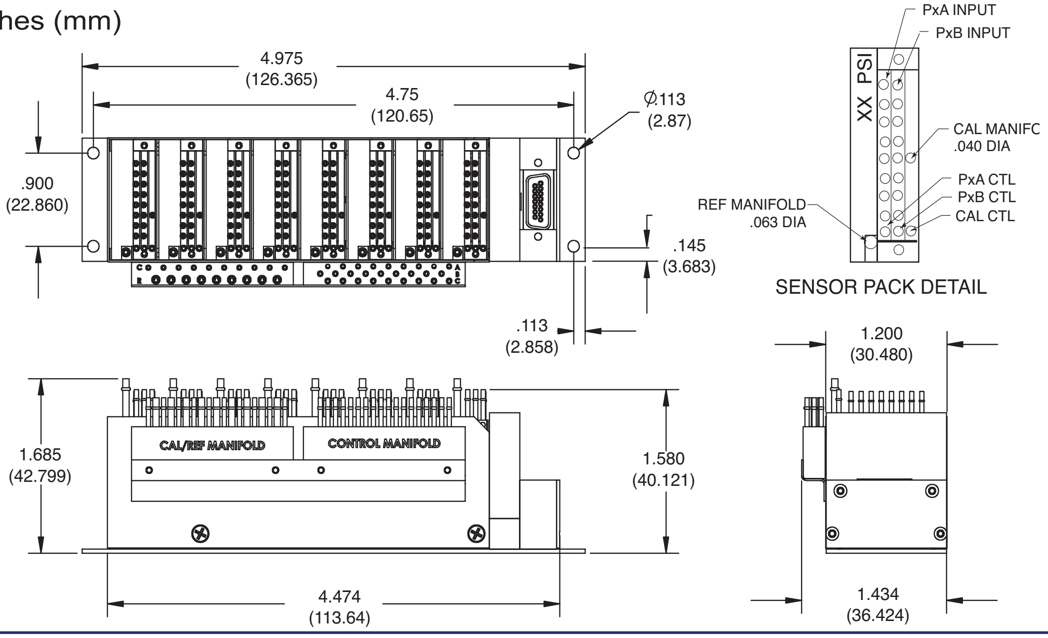

Scanivalve Headquarters
1722 N. Madson Street
Liberty Lake, WA 99019
Tel: 509-891-9970
800-935-5151
Fax: 509-891-9481
e-mail: scanco@scanivalve.com

Scanivalve
www.scanivalve.com